SAMARKAND STATE UNIVERSITY NAMED AFTER SHAROF RASHIDOV

On the right of the manuscript
UDC: 530.12:531.51

RAHMATOV BEKZOD MANSUR O‘G‘LI

FUNDAMENTAL FREQUENCIES AND THERMODYNAMICAL PROPERTIES OF BLACK HOLES IN THE PRESENCE OF EXTERNAL MATTER FIELDS

01.04.02 - Theoretical physics

DISSERTATION OF THE DOCTOR OF PHILOSOPHY (PhD) IN PHYSICS AND MATHEMATICS

Scientific supervisor: Academician Bobomurot Ahmedov

Tashkent-2026

CONTENTS

Introduction 7

1 Black holes surrounded by Chaplygin-like dark matter: space-time properties and quasiperiodic oscillations tests 16

1.1 Introduction 16

1.2 BHs surrounded by dark fluid with Chaplygin-like EoS 20

1.2.1 A BH solution with dark fluid equation of state 21

1.2.2 Event horizon and effective mass 22

1.2.3 The scalar invariants 25

1.3 Circular motion of test particles 27

1.3.1 Stable orbits and ISCO characteristics 28

1.3.2 Angular Momentum & energy at ISCO and energy efficiency 31

1.4 Fundamental frequencies 33

1.4.1 Keplerian frequency 33

1.4.2 Orbital data 34

1.4.3 The Radial and Vertical Oscillation Frequencies 36

1.5 Astrophysical Applications to Theoretically Calculated Quasi-Periodic Oscillations 37

1.5.1 QPO models and orbits 39

1.6 MCMC analyses 42

1.7 Conclusion 46

2 Black holes coupled to nonlinear electrodynamics and perfect fluid dark matter: Spacetime Stability and Thermodynamics 48

2.1 Introduction 48

2.2 Black holes in GR coupled to NED surrounded by PFDM 49

2.2.1 Black hole solutions with the dark fluid equation of state 50

2.3 Energy conditions 54

2.4 Thermodynamics of black holes surrounded by PFDM 56

2.5 Conclusion 62

3 Magnetically charged black holes surrounded by perfect fluid dark matter: radiation processes, particle dynamics, and quasiperi- odic oscillations 64

3.1 Introduction 64

3.2 Spacetime 68

3.2.1 Black hole solutions with the dark fluid equation of state 69

3.2.2 The scalar invariants. 72

3.3 Circular motion of test particles 75
3.3.1 Equations of motion 75
3.3.2 The circular orbits 77
3.3.3 Stable circular orbits 79
3.4 Radiation properties of the accretion disk of black hole 81
3.5 Fundamental frequencies 86
3.6 Astrophysical Applications to Theoretically Calculated Quasi-Periodic Oscillations 90
3.6.1 QPO models and orbits 91
3.7 MCMC priors for Black Holes Coupled to NED and Surrounded by PFDM 96
3.8 Conclusion 100
Main result of the dissertation 102
Bibliography 103

Abbreviations

EoS	Equation of States
MCMC	Markov Chain Monte Carlo
PFDM	Perfect Fluid Dark Matter
QPOs	Quasi Periodic Oscillations
EHT	event horizon telescope
ISCO	innermost stable circular orbit
BH	black hole
SgrA*	Sagittarius A*
AdS	Anti de-Sitter
GR	General Relativity
AGNs	active galactic nuclei
NED	Nonlinear electrodynamics
DM	Dark Matter
DE	Dark Energy

Physical constants & other definitions

Speed of Light	$c = 2.998 \times 10^{10}$ cm s^{-1}
Gravitational constant	$G = 6.672 \times 10^{-8}$ cm^3 g^{-1} s^{-2}
Mass of the Sun	$M_\odot = 1.989 \times 10^{33}$ g
Mass of Sgr A*	$M_* = 4.14 \times 10^6 M_\odot = 8.23 \times 10^{39}$ g
Schwarzschild radius of the Sun	$r_S = 2GM_\odot/c^2 = 2.95 \times 10^5$ cm
Schwarzschild radius of Sgr A*	$R_S = 2GM_*/c^2 = 1.22 \times 10^{12}$ cm

1 parsec $= 1\text{pc} = 3.26\text{ly} = 3.08 \times 10^{18}$ cm
$1\text{eV} = 1.6 \times 10^{-19}$ J $= 1.6 \times 10^{-12}$erg
1 Gauss $= 1\text{G} = 10^{-4}$ T

INTRODUCTION

Topicality and demand of the dissertation.

Black holes are among the most important objects for testing general relativity in the strong gravitational-field regime. Their spacetime geometry, horizon structure, thermodynamic behavior, and particle dynamics are directly connected with observable astrophysical processes occurring near compact objects. In particular, the motion of test particles, accretion-related phenomena, and quasi-periodic oscillations observed in X-ray emissions provide important tools for studying the physical properties of black holes and their surrounding environments.

Recent astrophysical observations have shown that the distribution of dark matter in galaxies can be more diverse than expected. Several systems with very low dark matter content or without a clearly detectable dark matter component, including NGC 1052-DF2, NGC 1052-DF4, FCC 224, and dark matter deficient spiral galaxies, indicate that dark matter effects may strongly depend on the astrophysical environment. Numerical simulations also suggest that such systems can appear due to environmental mechanisms such as tidal interactions and stripping. These results motivate the study of effective models describing possible dark environments around compact objects, especially black holes.

Within general relativity, perfect fluid dark matter and Chaplygin-like dark fluid provide useful effective descriptions for investigating how dark environments may influence black hole physics. Perfect fluid dark matter can phenomenologically describe dark matter effects near black holes, while Chaplygin-like dark fluid is important because it can represent a medium with properties interpolating between dark-matter-like and dark-energy-like behavior. Therefore, studying black holes surrounded by these fields is relevant for understanding how external dark environments modify strong-field gravitational properties.

The presence of perfect fluid dark matter and Chaplygin dark fluid can change the spacetime structure around black holes, affect the event horizon, and modify

thermodynamic quantities such as Hawking temperature, entropy, and heat capacity. These fields can also influence the Keplerian, radial, and vertical epicyclic frequencies of particles moving around black holes. Since these fundamental frequencies are closely related to quasi-periodic oscillations observed in microquasars and other compact astrophysical systems, their analysis is important for connecting theoretical black hole models with observational data.

The demand for this dissertation is determined by the need to study black holes in realistic astrophysical environments and to clarify how dark matter and dark fluid parameters affect observable strong-field signatures. In particular, the investigation of particle dynamics, thermodynamic properties, fundamental frequencies, and QPO signatures makes it possible to test black hole models within general relativity and compare theoretical predictions with astrophysical observations. Thus, the dissertation is topical because it addresses the influence of perfect fluid dark matter and Chaplygin dark fluid on black hole thermodynamics, orbital motion, and quasi-periodic oscillations, which are among the important problems of modern relativistic astrophysics and strong-field gravity.

This dissertation corresponds to the tasks set by the following state regulatory documents: Decree of the President of the Republic of Uzbekistan No. UP4947 "On the Strategy of Actions for the Further Development of the Republic of Uzbekistan" dated February 07, 2017, and Decree of the President of the Republic of Uzbekistan No. PP-2789 "On Measures for Further Improvement of Academy of Sciences, organization, management, and financing of research activities from 18.02.2017.

Compliance of the research with the main priority areas for the development of science and technology in the Republic. The research conducted for the dissertation was carried out in accordance with the priority areas of science and technology of the Republic of Uzbekistan.

Degree of study the problem. The works of Kerr, Reissner-Nordström, Hawking, Page, Born-Infeld, and Maldacena have made significant contributions to the study of

black holes under the conditions of nonlinear electrodynamics. The Kerr and Reissner-Nordström metrics provide classical solutions, while Hawking and Page explored quantum effects. Born-Infeld and Maldacena proposed alternative theoretical approaches. These studies help deepen our understanding of the electromagnetic properties of black holes and their role in the universe.

In our country, the works of Bobomurat Ahmedov, Ahmadjon Abdujabbarov, Bobir Toshmatov, Javlon Rayimbaev, Farrux Atamuratov, and Sanjar Shaymatov on black holes in NED models hold an important place in modern astrophysics and theoretical physics. Their research reveals new physical properties by studying the effects of nonlinear electromagnetic fields around black holes and connects these processes with astrophysical observations.

My dissertation focuses on the combined effects of nonlinear electrodynamics and perfect fluid dark matter on black hole geometry, gravitational and electromagnetic fields, thermodynamic properties, and particle dynamics. It also investigates how external matter fields affect fundamental frequencies and quasi-periodic oscillation signatures, with the aim of comparing theoretical predictions with astrophysical observations.

Connection of the dissertation topic with the scientific research of the higher educational/research institutions, where the dissertation was carried out. The dissertation was carried out at Samarkand State University named after Sharof Rashidov within the framework of the scientific research topic and scientific projects of the Institute of Fundamental and Applied Research:

FL-7923051796 "Modeling the dynamics of scalar fields and quantum emitters in spherically symmetric gravitational fields" (2024-2026).

The aim of the research of the dissertation: Aim of the work is to assess astrophysical processes around black holes by studying their particle dynamics, fundamental frequencies, thermodynamic properties, and QPO signatures in the presence of Chaplygin dark fluid and perfect fluid dark matter.

The tasks of the research:

- to study the spacetime properties of black holes surrounded by CDF;
- to analyze the dynamics of test particles and stable circular orbits around black holes in the presence of CDF;
- to calculate the fundamental frequencies and study QPO signatures of black holes surrounded by dark fluid matter;
- to obtain new black hole solutions in GR coupled to NED in the presence of PFDM;
- to study the thermodynamic properties and phase-transition behavior of black holes in NED and PFDM fields;
- to constrain black hole and surrounding-field parameters using QPO data and MCMC analysis.

The objects of the research are black holes influenced by PFDM and NED, including their geometric and thermodynamic properties, the orbital motion of test particles, accretion disk and radiation characteristics, as well as the determination of PFDM and NED parameters using MCMC simulations.

The subjects of the research is the influence of PFDM and NED models on black holes, test particles, accretion disks, and shadows, as well as the study of the geometric and thermodynamic properties of black holes within these models.

The methods of the research are Theoretical and analytical methods; methods of general relativity; numerical modeling; thermodynamic analysis; orbital dynamics analysis; statistical and MCMC methods.

The scientific novelty of the research is the follows:

- for the first time, two types new black hole solutions are obtained in GR coupled to NED in the presence of PFDM;
- for the first time, we have shown that the heat capacity of the black hole undergoes phase transitions due to the NED field and dark matter;

- for the first time, we constrain the parameters of black holes, NED, and dark fields, namely Chaplygin dark fluid and perfect fluid dark matter, using QPO data from microquasars and stellar-mass black holes through MCMC analysis.

Practical results of the research are as follows:

The parameters of black holes surrounded by Chaplygin-like dark fluid were constrained using MCMC simulations based on observed QPO data. For XTE J1550–564, GRO J1655–40, GRS 1915+105, Sgr A*, and M82 X-1, the parameters were obtained in the ranges $B = 5.311 \times 10^{-5}$–9.340×10^{-5}, $q = 0.651$–0.953, and $r/M = 3.057$–4.496.

For magnetically charged black holes surrounded by perfect fluid dark matter, the observed QPO data of XTE J1550–564, GRS 1915+105, GRO J1655–40, and M82 X-1 constrained the parameters within $q/M = 0.0241$–0.0692 and $\lambda/M = 0.0203$–0.0281. The corresponding QPO orbital radii were found in the range $r/M = 6.0961$–7.3697.

It has been shown that the heat capacity of black holes in the presence of NED and PFDM changes its sign at the phase-transition point. This result allows one to distinguish thermodynamically unstable and stable black hole configurations. Therefore, the obtained results can be practically used to estimate black hole mass, magnetic charge, dark-fluid parameters, and PFDM parameters from QPO observations.

Reliability of the research results

The reliability of the research results is ensured by the use of well-established methods of mathematical physics, computational mathematics, and relativistic astrophysics. All calculations are carried out within the framework of general relativity and black hole physics. The obtained results are based on analytical derivations and numerical computations of the spacetime geometry, horizon structure, thermodynamic quantities, particle motion, fundamental frequencies, and quasi-periodic oscillation signatures. The validity of the results is further supported by comparison with known limiting cases, previously published results, and available astrophysical observational

data. The conclusions of the dissertation are consistent with the basic principles of compact object astrophysics and strong-field gravity.

Scientific and practical significance of the research

The scientific significance of the research lies in clarifying how perfect fluid dark matter, Chaplygin dark fluid, and nonlinear electrodynamics affect the physical properties of black holes. In particular, the dissertation investigates their influence on black hole geometry, horizon structure, thermodynamic behavior, particle dynamics, and fundamental frequencies. These results contribute to a deeper understanding of black holes surrounded by external matter fields and provide theoretical insight into how such environments can modify strong gravitational-field processes.

The practical significance of the research is related to the application of the obtained results to astrophysical observations of compact objects. The analysis of Keplerian, radial, and vertical epicyclic frequencies makes it possible to study quasi-periodic oscillation models and compare theoretical predictions with observed QPO data from microquasars and supermassive black hole candidates. Therefore, the results of the dissertation can be used to estimate black hole and external matter field parameters more accurately and to interpret observational signatures arising from strong-field regions around black holes.

Applications of the research results

The results of the study titled fundamental frequencies and thermodynamical properties of black holes in the presence of external matter fields have been applied as follows:

- in the investigation of the fundamental frequencies and thermodynamical properties of black holes influenced by external matter fields, this approach has been utilized by several authors ("Li, Xiang-Qian and Kim, Yoonbai and Lee, Bum-Hoon and Yan, Hao-Peng and Yue, Xiao-Jun. Black holes immersed in modified Chaplygin-like dark fluid and cloud of strings: geodesics, shadows, and images. Chinese Physics C, 2025", "Javed, Faisal and Waseem, Arfa and Mustafa, G. and Fatima, Ghulam and

Alkarni, Shalan". Particle motion and thermal fluctuations of charged AdS black holes surrounded by external matter fields fluid with modified Chaplygin equation of state. Phys. Dark Univ. 47, 2025" and "Turimov, Bobur and Rahimov, Ozodbek and Davlataliev, Akbak and Tadjimuratov, Pulat and Norkobilov, Mukhiddin and Rahimova, Shakhzoda. Analysing geodesic motion in Bocharova-Bronnikov-Melnikov-Bekenstein spacetime. 2025. Phys.Dark Univ. 48 (2025) 101855", "Erdem Sucu, Izzet Sakall. "Astrophysical reality of black hole thermodynamics and dynamics: Transformative influence of Hernquist dark matter distributions", Physics of the Dark Universe, vol. 49, 2025, 102051.");

- scientific results obtained on the motion of particles and photons have been used by scientists from Fudan University (FU) in Shanghai (FU, China, May 23, 2025);

Approbation of the research results The dissertation results have been discussed in 4 international and 3 local conferences.

Publication of the research results were presented in 7 scientific articles published in scientific journals recommended by the Higher Attestation Commission under the Ministry of Higher Education, Science and Innovation of the Republic of Uzbekistan.

Volume and structure of the dissertation

Consists of an introduction, three chapters, a conclusion, and a list of references all in 115 pages.

List of published papers

Dissertation chapters have been constructed using the results of the following published papers:

- B. Rahmatov, M. Zahid, J. Rayimbaev, R. Rahim, and S. Murodov, "QPOs and circular orbits around black holes in Chaplygin-like cold dark matter," Chin. J. Phys. 92, 143-165 (2024), (IP - 4.6, Q1)
- B. Rahmatov, M. Zahid, S. U. Khan, J. Rayimbaev, I. Ibragimov, Z. Yuldoshev, A. Dauletov, and S. Muminov, "Black holes in general relativity coupled

with nonlinear electrodynamics surrounded by perfect fluid dark matter: Thermodynamics, particle motion and black hole shadow," Chinese Phys. C 49, no. 7, 1-21 (2025).(IP - 3.6, Q1)

- Bekzod Rahmatov, Sardor Murodov, Javlon Rayimbaev, Sokhibjan Muminov, Inomjon Ibragimov, Rashid Eshburiev, "QPO tests and charged particles around regular ABG black holes", Physics of the Dark Universe, 102102, 2025. (IP - 4.2, Q1)
- Bekzod Rahmatov, ”Testing black holes beyond Kerr: A critical review of imaging, thin-disk spectroscopy, and QPOs in modified gravity and dark-matter environments”, International Journal of Modern Physics D, https://doi.org/10.1142/S021827182630003X
- B.Rahmatov, B.Ahmedov, "Dynamics of Test Particles Around Black Holes in NED and PFDM", TURANIAN JOURNAL Volume 1, Number 2 (010206), 2025
- F. Umirzokov B. Rahmatov, P-V criticality and stability analysis of charged BTZ black holes. Scientific Bulletin of Samarkand State University. 2025, No. 1/1 (149).
- B. Rahmatov, D. Abduraimov, Topology of equatorial time-like circular orbits around quiescent black holes. Bulletin of Samarkand State University. 2024, No. 1/2 (143).

Chapter 1: Black holes surrounded by Chaplygin-like dark matter: spacetime properties and quasiperiodic oscillations tests

1.1 Introduction

In modern cosmology, the question of what constitutes matter in the Universe is still unclear. According to the latest Planck full-sky images of CMB anisotropies, the baryon matter is projected to contribute no more than 5% to the overall energy density [1]. On the other hand, dark energy and dark matter account for approximately 95% of the energy density in the universe. Considering the significant impact of the dark sector on the Universe, it is appropriate for us to acquire more knowledge about BHs in the presence of these peculiar forces. The linear EoS is a characteristic of quintessence, making it a viable candidate for dark energy. There has been significant interest in studying the properties of BHs that are static, spherical, and surrounded by quintessence matter [2-11].

The invisible dark sector of the universe, including dark energy and dark matter, is about 95%, and the sector is dominant over the universe. Therefore, studying BHs surrounded by such a mysterious field that is a candidate for the dark field is actual. Quintessence is an exciting candidate for dark energy. Several studies discuss static spherically symmetric BHs surrounded by quintessence matter and their properties [2-4]. Another possibility in the universal dark sector is that the unknown energy component is a unified dark fluid that mixes dark matter and dark energy. Among the proposed unified dark fluid models, the Chaplygin gas and its generalized models have been widely studied to explain the accelerating Universe [11]. Therefore, adopting the gas with (generalized and modified) Chaplygin EoS as a matter source to construct BH solutions is interesting.

The Chaplygin gas model is a unique kind of dark energy and matter that is characterized by its peculiar equation of state $p = -B/\rho$, where p is the pressure, ρ is the density, and B is a positive constant. The main advantage of this model is its ability to combine dark matter and dark energy into a single fluid description. In the early stages, this fluid behaves like dust; in the later stages, it behaves like a cosmological

constant [12]. This duality is advantageous for simultaneously tackling the problems of cosmic acceleration and structure development [13]. The presence of Chaplygin gas in BHs may impact their accretion and evaporation processes. This effect has the potential to cause noticeable variations in the pace at which the BH grows and in its temperature spectrum [14]. Additional research has investigated the influence of the model on variations in the cosmic microwave background, which has helped to establish limitations on its parameters [15]. Furthermore, the Chaplygin gas has been linked to a solution to the cosmic coincidence problem. It provides a more comprehensive framework for comprehending BH environments impacted by dark energy components [16]. Recent studies have expanded the notions to include higher-dimensional theories, such as brane-world scenarios, which increases the model's adaptability and importance [17]. These aspects make the Chaplygin gas model a pivotal topic in cosmology and astrophysics.

The BH's investigation includes many arrangements and characteristics, including the presence of accretion disks surrounding Reissner-Nordström BHs with nonlinear electrodynamics [18] and the effect of dark fluid on BHs. The study conducted in Ref. [19] examined the effects of tidal forces and shadow limitations on Schwarzschild-like BHs under Starobinsky-Bel-Robinson gravity. Additionally, Rehman et al. [20] evaluated the influence of magnetic charges and scalar hair on matter accretion. The analysis of thermal characteristics and Joule-Thomson expansion of BHs in metric-affine gravity has been conducted in Ref. [21]. Additionally, the study of light deflection by wormholes caused by dark matter has been carried out within the framework of modified symmetric teleparallel gravity [22]. Additional areas of emphasis encompass the structural characteristics of gravastars with electric charge, as discussed in the publication by Mustafa et al. [23]. Furthermore, the investigation explores original solutions for wormholes within the context of Ricci inverse gravity, as presented in Ref. [24]. Lastly, the examination delves into the analysis of gravastars with electric charge in the framework of symmetric teleparallel

gravity [25,26]. Studies have also investigated BHs in the context of Starobinsky-Bel-Robinson gravity [27] and the process of matter accretion in metric-affine gravity [28]. Furthermore, the phenomenon of Joule-Thomson expansion in AdS BHs has been explored in Ref. [29]. Furthermore, researchers have investigated the phenomenon of gravitational lensing caused by BHs in dark matter halos [30], the behavior of objects in circular orbits around BHs with nonlinear electrodynamics [31], and the study of tunneling in null aether BHs [32].

Based on astronomical observations, it has been hypothesized that the cosmos is undergoing acceleration [33]. To explain this acceleration, dark energy was introduced, which had a positive energy density and negative pressure. Quintessence, a dark energy, was considered a potential negative pressure source. The EoS is given by the expression $p = \omega\rho$, where ω represents the quintessence state parameter. It is important to note that the value of ω falls between the range $-1 < \omega < -1/3$ [34]. Another concept known as dark matter (DM) is attributed to the accounted mass in galaxies and large-scale distribution in the universe. The pressure of DM is negligible. Models incorporating dark energy and DM have been suggested to interpret the universe's dark components and understand its thermal history. One such unified dark-fluid model that has caught the attention of describing the expanding universe is the Chaplygin gas and its generalizations [35-37].

Several authors have derived efficient BH solutions utilizing alternative approaches to quintessence matter. The work referenced in [38] presents the BH solutions that exist when an Abelian gauge field is present. These solutions are characterized by a density that is determined by a power of the Maxwell Lagrangian. The solutions of Einstein-Born-Infeld equations in asymptotically flat space (referenced as [39, 40]) and AdS spaces (referenced as [41, 42]) have been extensively studied as solutions of the theory of general relativity coupled with non-linear electrodynamics. There has been speculation surrounding the mysterious energy component in the dark sector of the Universe, suggesting that it may be a dark fluid that

combines dark matter and dark energy. Extensive research has been conducted on the Chaplygin gas [43-46] and its extended models [13] as potential unified dark-fluid models to explain the accelerating Universe [12, 47-54]. Utilizing the (generalized) Chaplygin gas as a matter source in constructing BH solutions is fascinating. In the framework of Lovelock gravity, the researchers in Ref. [55] examined a situation where a BH with charge, static nature, and spherical symmetry is encompassed by dark fluid with Chaplygin-like EoS (CDF). They obtained the BH solution analytically and calculated the corresponding thermodynamic characteristics. Xiang-Qian Li has discovered a stationary solution to the Einstein gravitational equations for a BH exhibiting spherical symmetry [34].

Observing QPOs in the X-ray emissions of BHs and neutron stars has revolutionized astrophysics by revealing crucial information about the intense gravitational conditions in their surroundings. The existence of quasiperiodic variations in brightness indicates the presence of basic physical processes, such as oscillations of accretion discs or gravitational interactions. These procedures may be used as techniques to analyze the basic properties of spacetime [31,56-58]. Twin-peak QPOs have been seen in some systems, leading to discussions over their origins and possible associations with oscillatory modes within the accretion disc. These results highlight the need to develop sophisticated theoretical frameworks and acquire more accurate observational data. The first discovery of QPOs in spectrum analysis and X-ray binary flux [59-61] has been extensively studied in several research studies, along with theoretical investigations into the characteristics and features of QPO. The QPO model with the greatest potential is associated with the dynamics of particles and the related oscillations of their trajectories. Previous studies have thoroughly examined the phenomena of QPOs, which arise from the synchronized motion of charged particles in an accretion disc. [62-76].

Recent research has made tremendous progress in enhancing our comprehension of BH physics, particularly about QPOs and the dynamics of test particles. Rayimbaev

et al. (2024) studied the behavior of test particles and QPOs near Kiselev BHs, including a cloud of strings. This study provided vital insights into the distinctive surroundings of these BHs [77-79]. Additional research has concentrated on studying the movement of test particles near regular Kiselev BHs, enhancing theoretical frameworks related to these phenomena. A separate investigation analyzed QPOs around hairy BHs in the context of Horndeski gravity, providing fresh insights into the impact of these modified theories of gravity on BH oscillations [76]. The study emphasized the significance of magnetic fields in examining regular nonminimal magnetic BHs as potential sources of QPOs. This examination revealed how magnetic interactions affect the oscillatory behavior of these BHs [80-83]. The study of charged particles and QPOs near magnetized Schwarzschild BHs has deepened our comprehension of the interaction between magnetism and the dynamics of BHs [84]. Furthermore, research on QPOs originating from BHs influenced by noncommutative geometry has yielded valuable knowledge on the effects of noncommutative geometry on BH dynamics [85]. These contributions improve our understanding of the intricate dynamics that regulate BH environments and the observable impacts they may have in astrophysical situations [86-104]. In this work, we adopt the signature $(-,+,+,+)$ for the space-time and utilize the unit system where $G = c = 1$. However, in our expressions related to astrophysical applications, we explicitly include the speed of light. The Latin indices span from 1 to 3, while the Greek indices range from 0 to 3.

1.2 BHs surrounded by dark fluid with Chaplygin-like EoS

In the context of BH solutions, researchers often study the behavior of BHs in different theoretical frameworks or gravitational backgrounds. This could involve exploring various metrics that describe spacetime geometry around BHs, such as the Schwarzschild metric for non-rotating BHs or the Kerr metric for rotating BHs. BH solutions in the background of the Chandrasekhar-Dyson field could involve investigating how BHs interact with or are influenced by certain hypothetical fields or

conditions proposed within the Chandrasekhar-Dyson framework. This could lead to insights into the behavior of BHs in more complex or external matter fields scenarios.

1.2.1 A BH solution with dark fluid equation of state

In this section, we provide a brief introduction of the black hole solution that has been developed in Ref. [34]. For the BH solution, the spherically symmetric metric is taken as

$$ds^2 = -f(r)dt^2 + \frac{1}{f(r)}dr^2 + r^2(d\theta^2 + \sin^2\,\theta d\phi^2) \tag{1.1}$$

where $f(r)$ is the metric function depending on the radial coordinate r. Authors in Ref. [34] have considered the non-linear behavior of the EoS for Chaplygin dark (perfect) fluid $p = -B/\rho$, with radial and tangential pressures $p_r = -\rho$ and $2p_t = \rho - 3B/\rho$, where B is a constant being positive. Here, the density ρ and pressure are radial dependent. The stress energy and Einstein tensors for the fluid are used in the following form:

$$T_t^t = T_r^r = -\rho, \qquad T_\theta^\theta = T_\phi^\phi = \frac{1}{2}\left(\rho - \frac{3B}{\rho}\right) \tag{1.2}$$

and

$$G_t^t = G_r^r = \frac{rf' + f - 1}{r^2}, \qquad G_\theta^\theta = G_\phi^\phi = \frac{2f' + rf''}{2r} \tag{1.3}$$

respectively. Using Eqs. (1.2) and (1.3) one can get the system of equations

$$f + rf' - 1 = -\rho r^2, \qquad \frac{1}{r}(2f' + rf'') = \rho - \frac{3B}{\rho} \tag{1.4}$$

From the above equation, one can immediately get,

$$\rho^2 = B + \frac{q^2}{r^6} \tag{1.5}$$

where q is an integration constant, and a positive normalization factor represents the CDF's intensity. In the geometrized units, the unit of density $[\rho] = cm^{-2}, [B] = cm^{-4}$ and $[q] = cm$. The unit of the parameter of the Chaplygin equation of state B is $kg^2/(m^4s^2)$ in the SI system. Simple algebraic analysis shows that $\rho \simeq \sqrt{B}$ when $q \rightarrow$

0 or at large distances, while when $B \to 0$ or at small distances $(r^6 \ll q^2/B)\rho \simeq q/r^3$. The function derived from [34] is obtained by solving Eq. (1.4) as

$$f(r) = 1 - \frac{2M}{r} - \frac{r^2}{3}\sqrt{B + \frac{q^2}{r^6}} + \frac{q}{3r}\operatorname{arcsinh}\frac{q}{\sqrt{B}r^3} \tag{1.6}$$

where M is BH mass, the quantity q represents CDF 's intensity and takes positive values. The CDF's EoS parameter, a positive constant B, is calculated using the EoS $p = -B/\rho$. For a comoving observer with the fluid, ρ and p represent the energy density and isotropic pressure, respectively. The spacetime metric (1.6) tuns to the Schwarzschild case at $B = q = 0$.

1.2.2 Event horizon and effective mass

The radial profiles of the metric function $f(r)$ for different values of B and q parameters are shown in Fig. 1.1. At $q = 0$, we can observe two horizons: event horizon and cosmological horizons, while the non-vanishing q parameter causes the appearance of the inner (Cauchy) horizon. Also, there is an upper limit in the values of q where Cauchy and event horizons disappear, but not the cosmological one.

To study the effect of the EoS parameters on the geometry around the BH, we consider the event horizon, which can be analyzed using the equation $f(r) = 0$. The dependence of the event horizon radius from the parameter

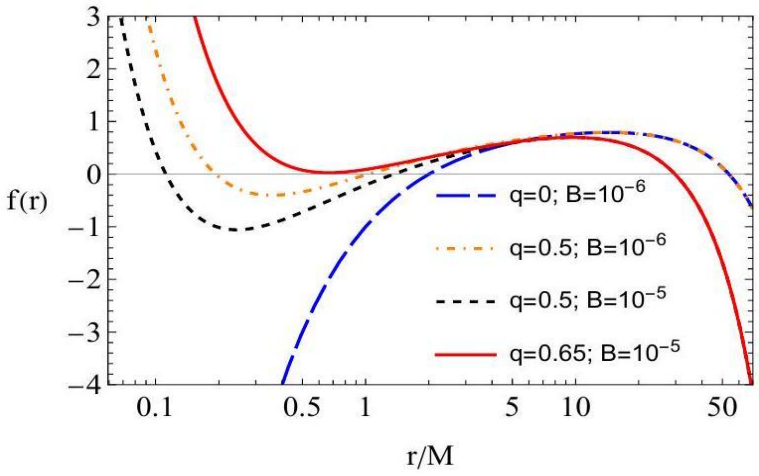


Figure 1.1: Radial dependence of lapse function $f(r)$ for varying values of q and B.

q for various values of B is shown in Fig. 1.2. Plotting the figure, we normalized all quantities to the BH mass and took $M = 1$. It is observed from the figure that the radius increases with the increase in the value of B. The event horizon shrinks as the parameter q increases, implying the parameter behaves with an antigravitating effect.

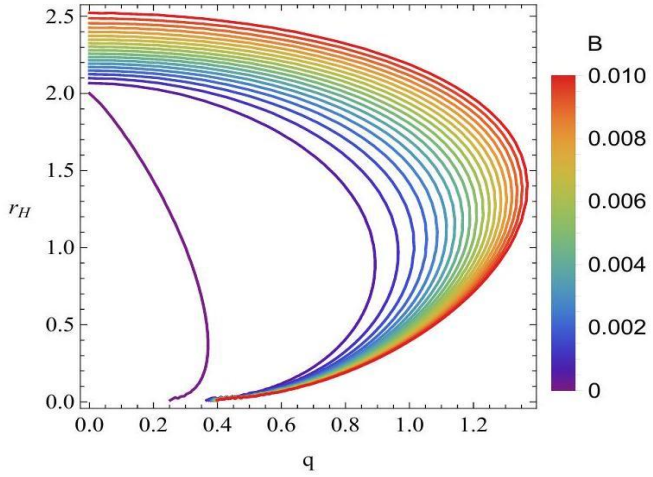


Figure 1.2: The event horizon radius as a function of q for different values of B.

There is an upper value for q where the event horizon and Cauchy horizons coincide. An increase in B causes an increase in the upper value and a decrease in the minimum value of the event horizon. In the $B = 0$ case, there is no inner horizon for the values of q that are less than about 0.25 . The mass of a stationary, asymptotically flat BH spacetime is linked to conserved quantities associated with the asymptotically timelike and spacelike Killing vector fields, $\eta^{\mu}_{(t)}$ and $\eta^{\mu}_{(\phi)}$. Ref. [56] outlines a general argument showing the equivalence of the conserved ADM mass and the Komar mass for stationary spacetimes with a timelike Killing vector. Using Komar's conserved quantities, we consider a spacelike hypersurface Σ_t, extending from the event horizon to spatial infinity, with a unit normal vector n_{μ}. The boundary S_t of Σ_t is defined by constant t and r surfaces with an outward normal vector σ_{μ}. The effective mass is then derived using the following equation:

$$M_{eff} = -\frac{1}{8\pi}\int_{S_t} \nabla^{\mu}\eta^{\nu}_{(t)} dS_{\mu\nu} \tag{1.7}$$

where $dS_{\mu\nu} = -2n_{[\mu}\sigma_{\nu]}\sqrt{h}d^2\theta$ is the surface element of S_t, h is the determinant of (2×2) metric on S_t, and

$$n_\mu = -\frac{\delta^t_\mu}{|g^{tt}|^{1/2}}, \sigma_\mu = -\frac{\delta^r_\mu}{|g^{rr}|^{1/2}} \tag{1.8}$$

are, respectively, timelike and spacelike unit outward normal vectors. Thus, mass integral Eq. (1.7) turned into an integral over closed 2 -surface at infinity:

$$M_{\text{eff}} = \frac{1}{4\pi}\int_0^{2\pi}\int_0^{\pi}\frac{\sqrt{g_{\theta\theta}g_{\phi\phi}}}{|g^{tt}g^{rr}|^{1/2}}\left(g^{tt}\Gamma^r_{tt} + g^{t\phi}\Gamma^r_{t\phi}\right)d\theta d\phi \tag{1.9}$$

Using the metric elements Eq. (1.1), we obtain the following expression for the effective mass of the BH :

$$M_{\text{eff}} = M - \frac{q}{6}\text{arcsinh}\frac{q}{\sqrt{B}r^3} + \frac{1}{3}\sqrt{Br^6 + q^2} \tag{1.10}$$

which is corrected due to the CDF field and goes over to the Kerr BH case that is $M_{\text{eff}} = M$, when $q = 0$. Simple algebraic analysis shows that $M_{\text{eff}} = M$ when $q \to 0$, while when $B \to 0$ or at large distances

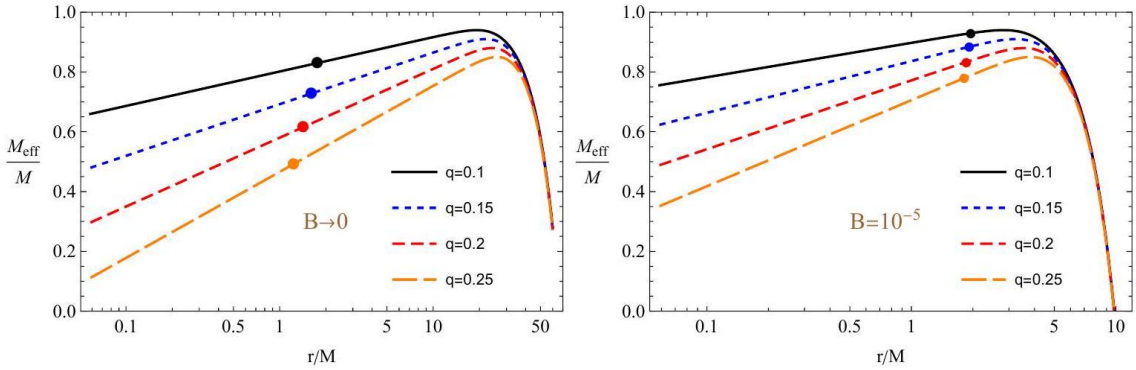


Figure 1.3: The behavior of effective mass vs. r for different values of the parameters. The black solid curves correspond to the Kerr-Newman BH, and the red dots in each curve denote the locations of the event horizon

In Fig. 1.3, we show the radial dependence of the effective mass of the spacetime geometry around the BH normalized to the BH for different values of q and B. One can see from the figure that At the limit $B \to 0$, as q increases, the peaks in the curves

decrease, and the distance where the peak occurs shifts slightly right. For larger distances, all the curves seem to converge. The dots in the curves imply the event horizons.

1.2.3 The scalar invariants.

To explore the properties of spacetime, we may start by studying the scalar invariants of geometry around a compact gravitating object. Here, we analyze the Ricci scalar, square of the Ricci tensor, and Kretschmann scalar of the spacetime metric (1.1) given with the lapse function given by Eq. (1.6). We calculate and analyze these quantities by observing their graphical behavior.

Ricci scalar

Ricci scalar, known as scalar curvature, defines as $R = g^{\mu\nu}R_{\mu\nu}$, where $R_{\mu\nu}$ is the Ricci tensor. The positive and the negative values of the Ricci scalar correspond to the sunken and convex form of the spacetime, respectively. After some algebraic calculations, the expression for the Ricci scalar takes the form

$$R = \frac{q^4 - 9Bq^2r^6 - 4B^2r^{12}}{r^3(q^2 + Br^6)^{\frac{3}{2}}}, \tag{1.11}$$

at $q \to 0, R = 4\sqrt{B}$ and at $B \to 0, R = q/r^3$.

Square of Ricci tensor

The second scalar invariant is the so-called square of the Ricci tensor, which is responsible for the square of the energy-momentum tensor of a field in spacetime. It is defined as $\mathcal{R} = R_{\mu\nu}R^{\mu\nu} \equiv \frac{1}{8\pi G}T_{\mu\nu}T^{\mu\nu}$ for the spacetime around BHs with the lapse functions given by Eq. (1.6) and takes the following form

$$\mathcal{R} = \frac{1}{2r^6(q^2 + Br^6)^4}\{q^6\left[5q^4 + 21Bq^2r^6 + B^2\left(65 + 2(Br^6 + q^2)\right)r^6\right] + B^3[7q^4\{11 + 4(Br^6 + q^2)r^{12}\} + 4Bq^2[9 + 2(Br^6 + q^2)r^{18}] + 8B^2r^{30}]\}$$

Therefore,

$$q \to 0 \Longrightarrow \mathcal{R} = 4B$$
$$B \to 0 \Longrightarrow \mathcal{R} = \frac{5q^2}{2r^6} \tag{1.13}$$

Kretschmann scalar

Now, we consider the Kretschmann scalar $\mathcal{K} = R_{\mu\nu\sigma\rho}R^{\mu\nu\sigma\rho}$, physically, the square root of the Kretschmann scalar can also be interpreted as an effective gravitational energy density $\sqrt{\mathcal{K}} \sim \rho_M$. The Kretschmann scalar for the spacetime metric (1.6) can be written as

$$\mathcal{K} = \frac{1}{3r^6(q^2+Br^6)^2}\left\{+\frac{36B^3q^2r^{18}+8B^4r^{24}}{3r^6(q^2+Br^6)} + 144M^2(q^2+Br^6)^2\right.$$
$$-24Mq^2\sqrt{Br^6+q^2}(7q^2+13Br^6) + \frac{63q^8+254Bq^6r^6+327B^2q^4r^{12}}{3r^6(q^2+Br^6)}$$
$$\left.+2q\operatorname{arcsinh}\frac{q}{\sqrt{B}r^3}\left[1+q^2\sqrt{Br^6+q^2}(7q^2+13Br^6)-12M(q^2+Br^6)^2\right]\right\}$$

From that, we have

$$q \to 0 \Longrightarrow \mathcal{K} = \frac{8B}{3} + \frac{48M^2}{r^6} \tag{1.14}$$
$$B \to 0 \Longrightarrow \mathcal{K} = \frac{21q^2+48M^2-56Mq}{r^6} \tag{1.15}$$

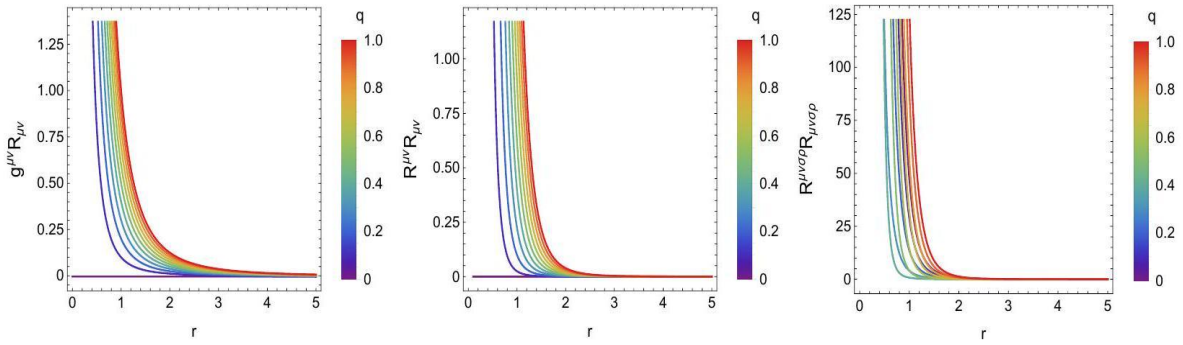


Figure 1.4: Radial profiles of scalar invariants, varying values of q. from the left to the right, we show the Ricci scalar, the square of the Ricci tensor, and the Kretschmann scalar, respectively.

Fig. 1.4 shows the radial dependence of scalar invariants: the Ricci scalar, the square of the Ricci tensor, and the Kretschmann scalar for the various values of q. All

the invariants rapidly decrease as r increases and approach an asymptotic value, becoming Ricci flat. An increase in the parameter q causes a slight increase in the scalar invariants.

1.3 Circular motion of test particles

Since test particle motion refers to the movement of particles with no net electric charge, electric fields do not influence these particles due to their lack of charge. However, they may still be subject to other forces, such as gravitational, magnetic, or particle interactions. Understanding the motion of neutral particles is crucial in various scientific fields, including nuclear physics, astrophysics, and materials science. Studying neutral particle dynamics with external fields interacting with their surroundings provides insights into the behavior of matter under different conditions and helps understand fundamental processes in the universe.

1.3.1 Stable orbits and ISCO characteristics

The standard Lagrangian density for the neutral particle with rest mass m moving around a BH can be written as

$$\mathcal{L}_{\mathrm{p}} = \frac{1}{2} g_{\mu\nu} \dot{x}^{\mu} \dot{x}^{\nu}. \tag{1.16}$$

Due to the existence of the timelike and spacelike Killing vectors, one may introduce the conserved specific energy $\mathcal{E}$ and specific angular momentum $\mathcal{L}$ of the particle in the following form

$$g_{tt}\dot{t} = -\mathcal{E}, g_{\phi\phi}\dot{\phi} = \mathcal{L} \tag{1.17}$$

One can govern the equations of motion for a test particle using the normalization condition,

$$g_{\mu\nu} u^{\mu} u^{\nu} = \epsilon, \tag{1.18}$$

where ϵ is 0 and -1 for massless and massive particles, respectively. For neutral test particles, the motion is governed by timelike geodesics of the spacetime, and the motion equations can be found using Eq. (1.18). Taking into consideration Eq. (1.17). One may easily obtain the following equations of radial and vertical motions,

$$\dot{r}^2 = \mathcal{E}^2 + g_{tt}\left(1 + \frac{K}{r^2}\right), \dot{\theta}^2 = \frac{1}{g_{\theta\theta}^2}\left(K - \frac{\mathcal{L}^2}{\sin^2\theta}\right), \tag{1.19}$$

where K is the Carter constant associated with the total angular momentum. Restricting the motion of the particle to the constant plane $\theta = \text{const}$ and $\dot{\theta} = 0$, the Carter constant takes the form $K = \mathcal{L}^2$, and the equation of the radial motion can be expressed as

$$\dot{r}^2 = \mathcal{E}^2 - V_{\text{eff}}, \tag{1.20}$$

where the effective potential of the motion of neutral particles is defined as

$$V_{\text{eff}}(r;\theta) = f(r)\left(1 + \frac{\mathcal{L}^2}{r^2 \sin^2\theta}\right). \tag{1.21}$$

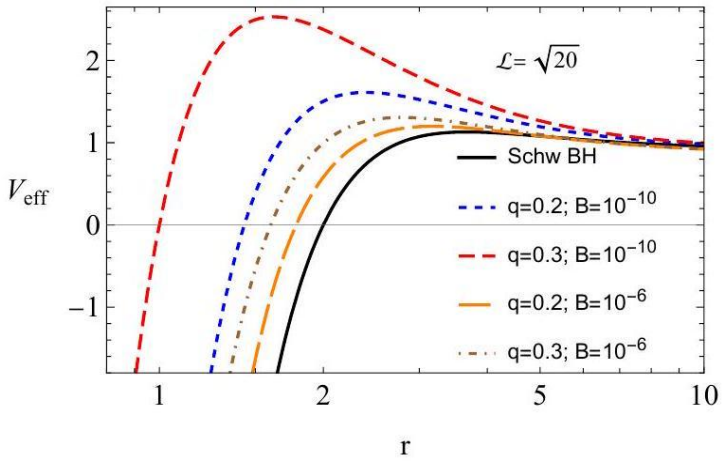


Figure 1.5: The radial dependence of the effective potential for the circular motion of test particles around the BH for different values of q and B parameters. The specific angular momentum is fixed as $\mathcal{L} = \sqrt{20}M$.

The radial profile of effective potential is shown in Fig. 1.5 for various values of CDF and EoS parameters, q and B, and a comparison is made with the Schwarzschild BH case. It is evident from the figure that the maximum of V_{eff} has increased due to q and B and the orbits corresponding to the maximum shifts towards the central BH, compared with the Schwarzschild case (black curve).
To study the circular motion of the particles, we use the following conditions:

$$\dot{r}^2 = 0, \text{ or } V_{\text{eff}} = \mathcal{E}^2, \text{ and } V'_{\text{eff}} = 0 \tag{1.22}$$

Using the solution of Eq. (1.22), we found the following expressions for the expressions of angular momentum and energy of particles corresponding to circular orbits:

$$\mathcal{L}^2 = \frac{r^2\left[2\sqrt{Br^6+q^2}-6M+q\,\mathrm{arcsinh}\frac{q}{\sqrt{B}r^3}\right]}{3\left(6M-2r-q\,\mathrm{arcsinh}\frac{q}{\sqrt{B}r^3}\right)} \tag{1.23}$$

$$\mathcal{E}^2 = \frac{2}{9r\left(2r-6M+q\,\mathrm{arcsinh}\frac{q}{\sqrt{B}r^3}\right)} \tag{1.24}$$

$$\times\left(3r-6M-\sqrt{q^2+Br^6}+q\,\mathrm{arcsinh}\frac{q}{\sqrt{B}r^3}\right) \tag{1.24}$$

$$\times\left(3r-12M+\sqrt{q^2+Br^6}+2q\,\mathrm{arcsinh}\frac{q}{\sqrt{B}r^3}\right) \tag{1.24}$$

Fig. 1.6 shows the radial profiles of the energy $\mathcal{E}$ (left panel) and the angular momentum $\mathcal{L}$ (middle panel) corresponding to circular orbits. In the right panel, we show the energy and angular-momentum dependencies. Figures in the top panel for the case of $B = 0$, and in the bottom one for the case of $B = 10^{-7}$. The minimum of both quantities increases with a decreasing intensity parameter of the CDF q. In the right panel, we show particles' energy dependence and angular momentum corresponding to circular orbits. The minimum in the curve implies that the values of $\mathcal{L}$ and $\mathcal{E}$ correspond to their ISCO value (right columns). An increase in the parameter q causes the ISCO energy and angular momentum to increase. It is observed that the ISCO energy and the ISCO angular momentum increase faster in the $B = 0$ case than in the case of $B = 10^{-7}$. The equation describes the stability condition for circular orbits in compact objects that gravitate in spacetime $\partial_{rr}V_{\text{eff}} \geq 0$. The innermost stable circular orbits satisfy the condition $\partial_{rr}V_{\text{eff}} = 0$. This condition is often applied together with the circularity condition in Eq. (1.22). The equation $\partial_{rr}V_{\text{eff}} = 0$ leads to the following equation

The radius of the ISCO of the test particles can be calculated numerically by solving Eq. (1.25). The dependence of ISCO radius from the parameters B and q are shown in Fig. 1.7. It is observed from the figure that an increase in q, r_{ISCO} decreases for a given value of B.

$$2Br^6(4r-15M)+3(12M^2+q^2-2Mr)\sqrt{q^2+Br^3}$$
$$-q^2(r+12M)+q\text{arcsinh}\frac{q}{\sqrt{B}r^3}[2q^2+5Br^6 \qquad (1.25)$$
$$+\sqrt{q^2+Br^3}\left(r-12M+q\text{arcsinh}\frac{q}{\sqrt{B}r^3}\right)]=0.$$

However, it increases with an increase of B for a given value of q, reaching its maximum at the upper value of B. The upper value in B also increases due to an increase in q. Moreover, it is also observed that there is an outermost stable circular orbit (OSCO) in the presence of the B parameter due to the effect of the cosmological horizon. An increase in the q parameter causes an increase in the OSCO radius.

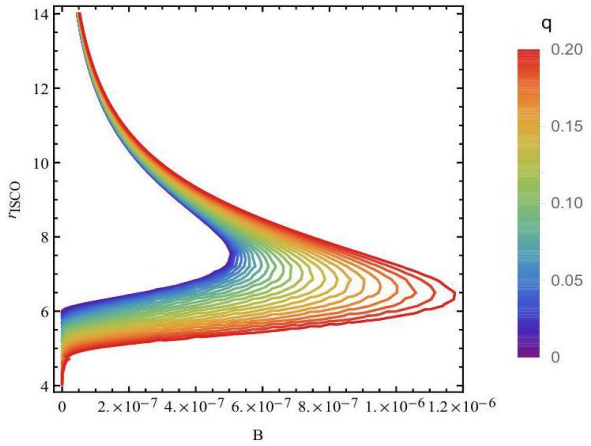


Figure 1.7: Dependece of r_{ISCO} on B for various values of q.

1.3.2 Angular Momentum & energy at ISCO and energy efficiency

This subsection discusses particles' angular momentum and energy at their ISCOs around the BH. The Keplerian accretion around an astrophysical BH is modeled as the geometrically thin disk governed by the properties of the spacetime circular geodesics. Generally, the energy efficiency of the accretion disk around a BH means the maximum energy that can be extracted as radiation from the infalling matter into the central BH . The efficiency of the accretion of the test particle can be calculated through the following expression:

$$\eta = 1-\mathcal{E}_{ISCO}, \qquad (1.26)$$

where $\mathcal{E}_{ISCO}$ is the particle's energy at the ISCO, characterized by the binding energy ratio.

In Fig. 1.8, we present the values of $\mathcal{L}_{ISCO}, \mathcal{E}_{ISCO}$ and the energy efficiency η for various values of parameters q and B. We can observe that there is a minimum and a maximum value in $\mathcal{L}_{ISCO}$ and $\mathcal{E}_{ISCO}$ at different values of the EoS parameter B. The minimum (maximum) energy and angular momentum values decrease (increase) with an increase in q. In addition, the critic value of B in which the profiles of $\mathcal{L}_{ISCO}$ and $\mathcal{E}_{ISCO}$ take the maximum decrease with increasing q. In contrast, energy efficiency takes a minimum at the critical EoS parameter.

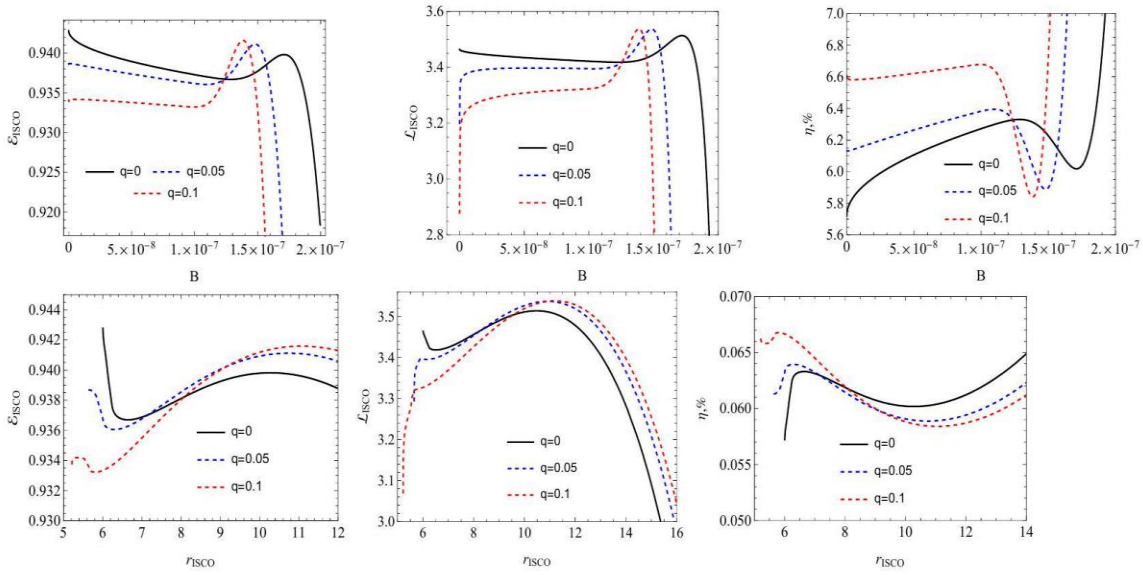


Figure 1.8: Dependecies of $\mathcal{E}_{ISCO}$&$\mathcal{L}_{ISCO}$ and energy efficiency from r_{ISCO} and B parameter for various values of q.

1.4 Fundamental frequencies

This section discusses the fundamental frequencies of test particles around our modified Schwarzschild BH of metric (1.1) are discussed.

The plan is to study the possible values of the upper and lower frequencies by the following models for twin peak HF QPOs described by the fundamental frequencies of test particles around compact gravitating objects $\left(\nu_{r,\theta,\phi} = c^3/(2\pi GM)\Omega_{r,\theta,\phi}\right)$. The

equatorial circular orbits of a test particle are characterized by three fundamental frequencies:

1. Orbital frequency (or Keplerian frequency) ν_ϕ, which is the inverse of the orbital period.

2. Radial epicyclic frequency ν_r, which is the frequency of radial oscillations around the mean orbit.

3. The vertical epicyclic frequency ν_θ is the frequency of vertical oscillations around the mean orbit.

These three frequencies depend only on the space-time metric and the orbit radius. Although they are defined as the characteristic frequencies for the orbital motion of a free particle, there is a direct relation between these frequencies and those of the oscillation modes of the fluid of an accretion flow.

1.4.1 Keplerian frequency

To study the Keplerian frequency of a test particle, one uses the geodesic equation,

$$\ddot{x}^\alpha + \Gamma^\alpha_{\mu\nu}\dot{x}^\mu\dot{x}^\nu = 0, \tag{1.27}$$

here, $\Gamma^\alpha_{\mu\nu}$ are the Christoffel symbols and $\dot{x} = \dot{t}(1,0,0,\Omega)$, the equation of motion, the test particles get the form

$$\partial_r g_{tt} + \Omega^2 \partial_r g_{\phi\phi} = 0, \tag{1.28}$$

and the solution of the above equation for the Keplerian frequency, Ω_K, can be expressed as

$$\Omega_K^2 = \frac{M}{r^3} - \frac{1}{3r^3}\sqrt{Br^6 + q^2} - \frac{q}{6r^3}\operatorname{arcsinh}\frac{q}{\sqrt{B}r^3}. \tag{1.29}$$

To estimate the value of the fundamental frequencies, the unit of Hz is associated with them as,

$$\nu = \frac{1}{2\pi}\frac{c^3}{GM}\Omega, [\text{ Hz}]. \tag{1.30}$$

Note that the values of the speed of light in vacuum and the gravitational constant are $c = 3 \cdot 10^8$ m/sec and $G = 6.67 \cdot 10^{-11}$ m^3/(kg^2 $\cdot$ sec), respectively.

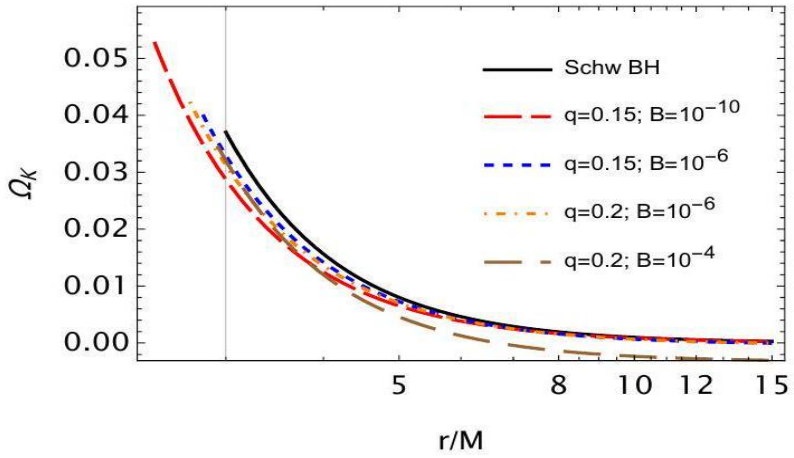


Figure 1.9: The figure shows the radial dependence Ω_r (for fixed B) and Ω_K.

The radial dependence of angular momentum of particles in Keplerian orbits is shown in Fig. 1.9 by varying the parameters q and B. One can observe that the Keplerian frequency increases in the presence of the parameter q compared to the Schwarzschil case. In contrast, the EoS parameter causes it to decrease. The effect of the intensity parameter of the dark fluid on the frequency is negligible at large distances.

1.4.2 Orbital data

Here, we aimed to test the dark fluid model with the Chaplygin EoS around the SgrA* using the hotspot observational data. One can immediately express the relations between the radius and period of the orbits of the particles $P = 1/\nu(r)$, where $\nu(r) = c^3\Omega(r)/(2\pi G M_{BH})$. The flares detected on May 27, July 22, and July 28, 2018, in near-infrared observations, with orbits close to (at the distance of about ~ 0.7AU) the supermassive BH (SMBH) Sgr A* at the center of the Milky Way galaxy (see Ref. [105]). Observations show that the flares' peak intensity is in the order of the flux of the S2 star, and the period is about $30 - 90$ minutes. The data from the hot-spot dynamics are useful to test the magnetic field and spacetime properties around Sgr A* [106, 107].

In Fig. 1.10, we present the dependence of orbital radius and period of the orbit for different values of the EoS and intensity parameters and obtained upper and lower

values for the intensity parameter q using orbital data from hotspot observations around supermassive BH SgrA*.

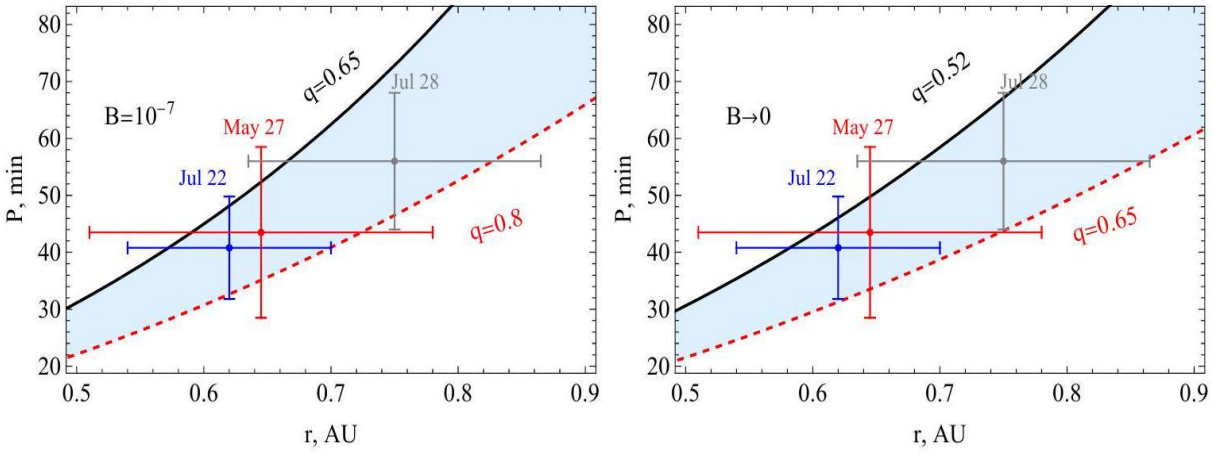


Figure 1.10: Dependence of the period on the orbital radius at different values of q

The mass of SgrA* is taken as $M_{SgrA*} = 4.14 \times 10^6 M_\odot$ and the distance from the solar system is 8 kpc while gravitational radius $R_g = GM_{\text{SgrA}*}/c^2 \simeq 6 \times 10^6$ km $\simeq 0.04077$AU. 1AU $\simeq 1.5 \times 10^8$ km and the angular size of SgrA* is about 5μ as [105]. It is observed that at $B \to 0$, the lower and upper values from $q \simeq 0.65 \div 0.8$, while at $B = 10^{-7}$, the values from 0.52 to 0.65 .

1.4.3 The Radial and Vertical Oscillation Frequencies

The test particles moving in the equatorial plane around BHs in stable orbits oscillate along radial and vertical axes because of the small displacement from their stable orbits as $r_0 + \delta r$ and $\pi/2 + \delta\theta$. The following harmonic oscillator equations can calculate the radial and vertical frequencies as [108-111]:

$$\frac{d^2\delta r}{dt^2} + \Omega_r^2 \delta r = 0, \frac{d^2\delta\theta}{dt^2} + \Omega_\theta^2 \delta\theta = 0 \tag{1.31}$$

where

$$\Omega_i^2 = -\frac{1}{2g_{ii}(u^t)^2}\partial_i^2 V_{\text{eff}}(r,\theta)\Big|_{\theta=\pi/2}, i = r, \theta \tag{1.32}$$

are the radial and vertical angular frequencies, respectively. Some algebra leads to

$$\Omega_r^2 = \Omega_K^2 \left\{ \frac{\left(4\sqrt{q^2 + Br^6} - 12M + 2q\text{ArcSinh}\left(\frac{q}{\sqrt{B}r^3}\right)\right)}{3r} \right.$$

$$+ \frac{\left(6M - 3r + \sqrt{q^2 + Br^6} - q\text{ArcSinh}\left(\frac{q}{\sqrt{B}r^3}\right)\right)}{6r\sqrt{q^2 + Br^6} - 18Mr + 3qr\text{ArcSinh}\left(\frac{q}{\sqrt{B}r^3}\right)}$$

$$\left. \times \left(6Mr^3 + \frac{q^2 - 8Br^6}{\sqrt{q^2 + Br^6}} - q\text{ArcSinh}\left(\frac{q}{\sqrt{B}r^3}\right)\right)\right\}$$

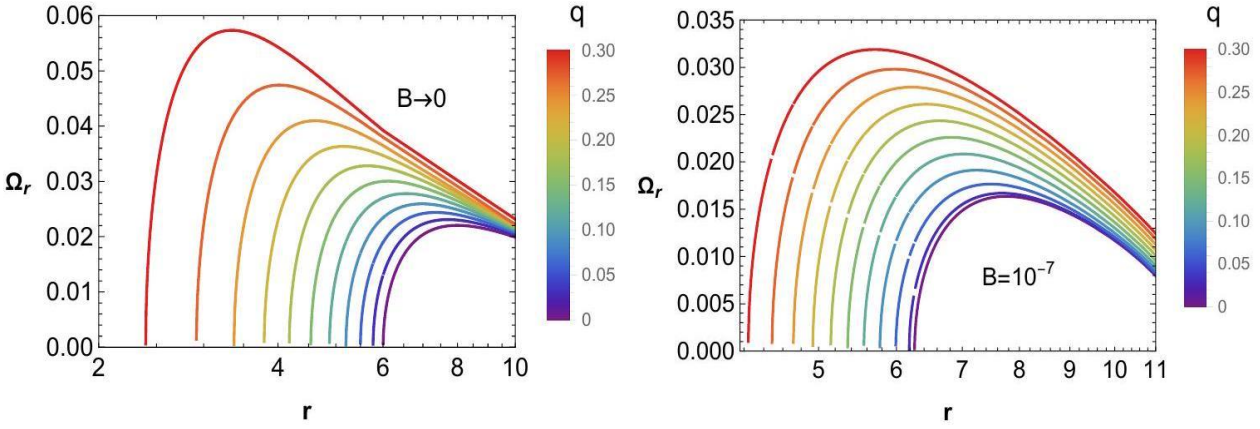


Figure 1.11: The figure shows the radial dependence Ω_r (for fixed B).

Fig. 1.11 represents the radial plots of Ω_r for a fixed value of B. The Ω_r graph shows that it increases with an increase in q, while the EoS parameter causes a decrease in it.

1.5 Astrophysical Applications to Theoretically Calculated Quasi-Periodic Oscillations

This section explores possible frequencies of twin-peak QPOs around Schwarzschild BHs surrounded by a dark fluid using various QPO models using a Chaplyginlike EoS. Special attention will be given to examining results on the frequency relationship with neutral particles orbiting Schwarzschild BH. In addition, we also focus on determining the relationship between the mass of the hairy BH and the parameter q using their observational frequency data from QPOs. We also consider

the BHs at the center of the microquasars GRS $1915+105$ and XTE 1550-564 surrounded by a dark fluid with Chaplygin-like EoS. Detectors on board X-ray missions can typically measure the time of arrival of every X-ray photon hitting the detector with an accuracy of micro and nanoseconds.

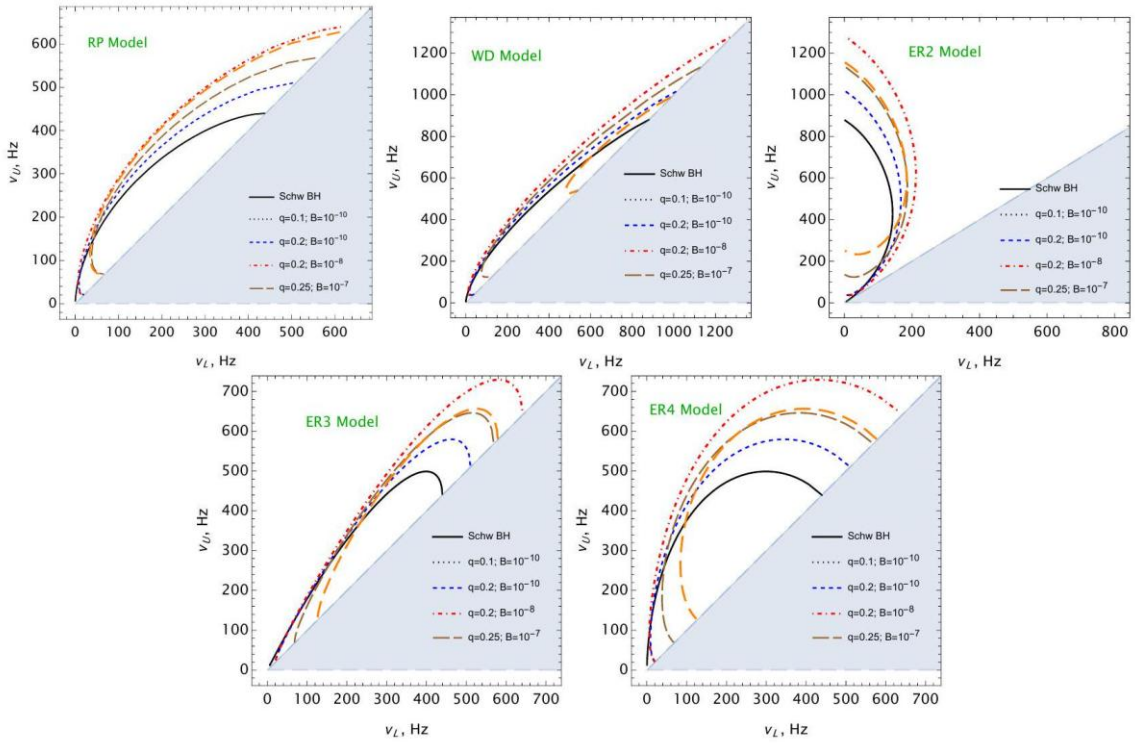


Figure 1.12: The relationship between the upper and lower frequencies around a Schwarzschild BH surrounded by CDF with Chaplygin-like EoS for the different parameter values q and B. Diagrams are shown in the RP, ER, and WD models from top left to bottom right.

QPOs are narrow features in the X-ray power density spectrum of a source found in the Fourier transformation of the photon count rate. In BH binaries, there are two classes of QPOs: low-frequency QPOs (LFQPOs) and high-frequency QPOs (HFQPOs). The low-frequency QPOs in the frequency range $0.1-30$Hzs on a short timescale (~ 1 min) or be relatively stable can be type-A, type-B, and type-C. For instance, type-A QPOs typically manifest when the source is in the high soft state, just after the intermediate state. The presence of type-B QPOs is used to define the soft intermediate state. Type C QPOs are mainly detected when the source is in the bright

end of the hard state or the hard intermediate state. Highfrequency QPOs have a frequency in the range of $40^{\vee}450$ Hz. In four systems, we have detection of pairs of HFQPOs (even if not always simultaneously) with the two frequencies that turn out to be in the ratio $3:2$. These two QPOs are usually called the upper and lower HFQPOs.

Source	ν_{U}[Hz]	$\Delta\nu_{\mathrm{U}}$[Hz]	ν_{L}[Hz]	$\Delta\nu_{\mathrm{L}}$[Hz]	Mass [$\mathrm{M}_{\odot}$]
XTE J1550-564	276	± 3	184	± 5	9.1 ± 0.61
GRS 1915+105	168	± 3	113	± 5	$12.4^{+2.0}_{-1.8}$
GRO J1655-40	451	± 5	298	± 4	5.4 ± 0.3
M82 X-1	5.07	± 0.06	3.32	± 0.06	415 ± 63

Table 1.1: BH binaries with a measurement of two high-frequency QPOs

Below, we analyze obtaining estimations of the EoS and BH parameters using the upper and lower frequencies of the microquasars given in Table: 1.1 in the QPO models we further discuss.

1.5.1 QPO models and orbits

In this subsection, we study the potential outcomes of lower and upper frequencies through the following models of twin peak QPOs, which can be described by the fundamental frequencies of test particles around compact gravitating objects:

- Stella and Vietri first presented the relativistic precession (RP) model for kHz twin peak QPOs related to the frequency range $0.2 - 1.25$kHz from neutron stars detected in LMXRBs. This model also applies to BHs in binary systems and accurately determines the mass and spin of central BH in microquasars by employing data from the power-density spectrum of the BH accretion disk. Corresponds upper and lower frequencies in the RP model are described by the frequencies of the radial, vertical, and orbital oscillations of test particles in the accretion disc near their ISCO $\nu_U = \nu_\phi$ and $\nu_L = \nu_\phi - \nu_r$;

- In the epicyclic resonance (ER) model, various resonance cases in the axisymmetric oscillations in a thin accretion disc around BHs are considered [62]. The

model establishes frequencies of the disc oscillations connected to the frequencies of orbital and epicyclic oscillations of the circular geodesics of the test particles. In this work, we study subcases of the ER model, namely ER2, ER3, and ER4, with the corresponding upper and lower frequencies in ER2-4 models $\nu_U = 2\nu_\theta - \nu_r$ and $\nu_L = \nu_r$, $\nu_U = \nu_\theta + \nu_r$ and $\nu_L = \nu_\theta, \nu_U = \nu_\theta + \nu_r$ and $\nu_L = \nu_\theta - \nu_r$, respectively;

- The warped disc (WD) model is based on non-axisymmetric oscillatory modes of a thin accretion disc around BHs and neutron stars. The upper and lower frequencies are $\nu_U = 2\nu_\phi - \nu_r, \nu_L = 2(\nu_\phi - \nu_r)$. Here, vertical oscillatory frequency has been initiated by supposing the vertical axial symmetric oscillations of the accretion disc, which lead the disc to be warped.

In Fig. 1.12, the diagrams $\nu_U - \nu_L$ are shown for the twin peak QPOs around the BH of the metric (1.1) in the RP, ER2, ER3, ER4, and WD models with the plots being compared to the QPOs around Schwarzschild's BH. Here, the mass of the central BH is $M = 5M_\odot$ as a test stellar mass BH . The lightblue shaded area in these diagrams represents the "graveyard" for twin-peak QPOs, where no twin-peaked QPOs are noticed. From the analyses, one can observe that there are no LF QPOs in the presence of q. An increase in the EoS parameter B causes an increase in the upper and lower frequencies near the kilohertz band. However, the frequencies decrease with the q parameter. This means that there are inverse relationships between the parameters B and q, resulting in the same upper and lower frequencies.

Here, we study the outer orbits of ISCO where a twin peak QPO occurs in the RP, ER2-4, and WD models using the set of equations $m\nu_L(M, r, q) = n\nu_U(M, r, q)$ where m and n are integers.

Fig. 1.13 presents the dependence of QPO orbits from the dark fluid intensity parameter. It is observed that the parameter q decreases the QPO radius and approaches the ISCO. According to the RP, ER3, and ER4 models, the orbit almost coincides with the ISCO.

Now, we analyze the distance between the ISCO and QPO orbit as ($\delta = r_{QPO} - r_{ISCO}$) for the QPOs observed in GRS $1915 + 105$ and XTE 1550564. Here, we assume the central BH is a BH surrounded by dark fluid with Chaplygin-like EoS. The frequencies of the QPO sources in the microquasars GRS $1915 + 105$ and XTE $1550 - 564$ are $\nu_U = 168 \pm 5$ Hz and $\nu_L = 113 \pm 3$ Hz, and $\nu_U = 184 \pm 5$ Hz and $\nu_L = 276 \pm 3$ Hz. The graphical representation is shown in Fig. 1.14.

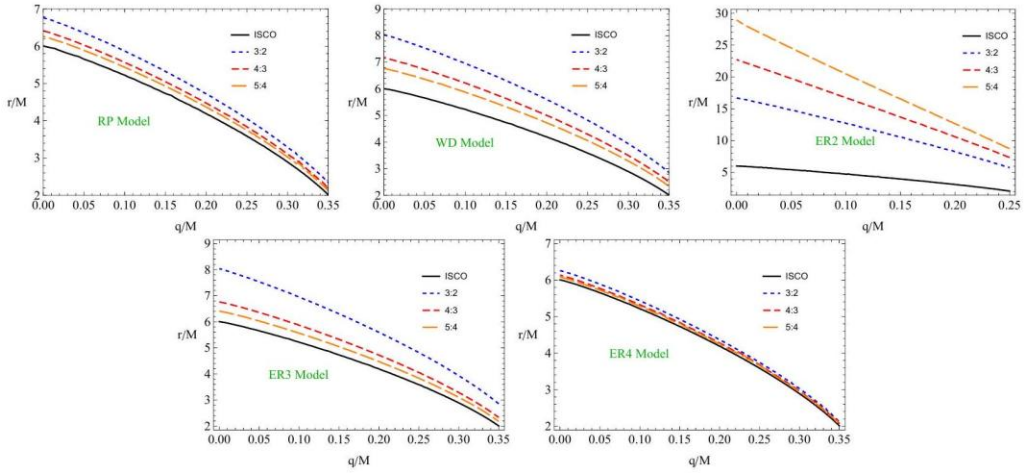


Figure 1.13: QPO radius as a function of q.

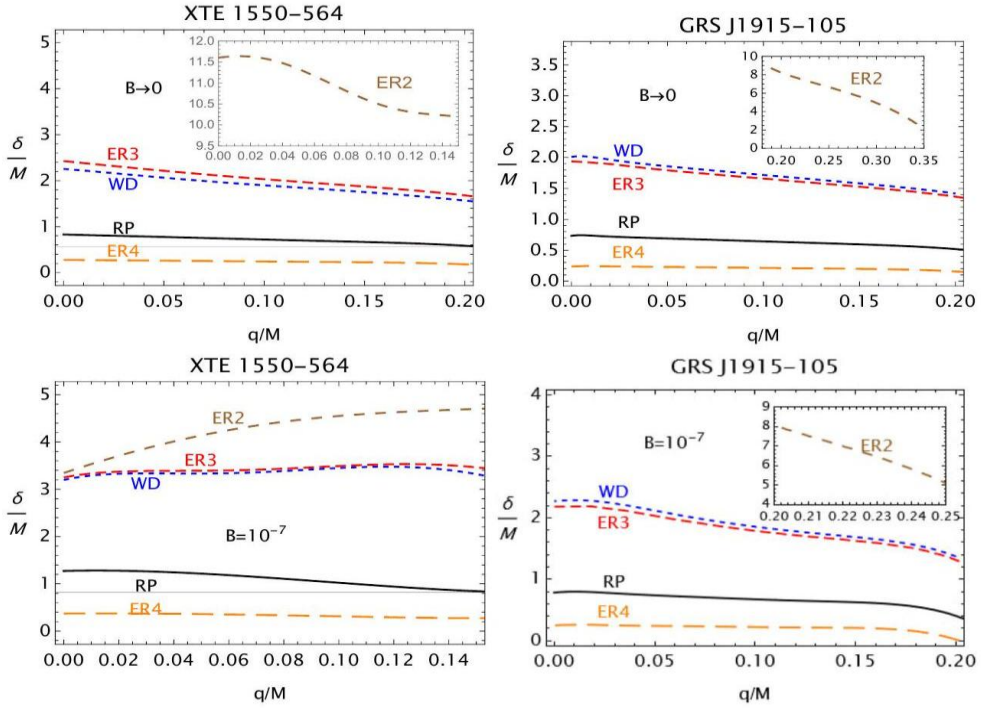


Figure 1.14: Distance between QPO orbits and ISCO as a function of the normalizing factor q, in RP, ER2-4, and WD models. The microquasars GRS

J1915+105 (right column) and XTE 1550-564 (left column), $B \to 0$ case is in the top row, in the bottom row, we fixed $B = 10^{-7}$.

1.6 MCMC analyses

In this section, we obtain constraints on the mass and metric parameters (1.1) of the black holes located at the center of (i) the microquasars GRS 1915-105, GRO J1655-40 and XTE 1550-564. We also used QPO data from (ii) M82 $\mathrm{X}-1$, an ultraluminous X-ray source in the galaxy M82. It is a candidate intermediate-mass black hole, with the exact mass estimate varying from around 100 to 1000 solar masses [112, 113]. In addition, we used (iii) mHz QPOs around supermassive black hole SgrA*. To obtain the constraints, we use the Python library emcee [114-116] and perform MCMC analysis in the RP model. The posterior distribution is [117],

$$\mathcal{P}(\theta \mid \mathcal{D}, \mathcal{M}) = \frac{P(\mathcal{D} \mid \theta, \mathcal{M})\pi(\theta \mid \mathcal{M})}{P(\mathcal{D} \mid \mathcal{M})} \tag{1.33}$$

where the functions: $\pi(\theta)$ is the prior function and $P(D \mid \theta, M)$ is the likelihood one. We consider priors has normal known as Gaussian distribution within suitable boundaries (see Table 1.2), i.e., $\pi(\theta_i) \sim \exp\left[-\frac{1}{2}\left(\frac{\theta_i - \theta_{0,i}}{\sigma_i}\right)^2\right]$, $\theta_{\text{low},i} < \theta_i < \theta_{\text{high},i}$. Here, the parameters are $\theta_i = \{M, B, q, r/M\}$ and σ_i are their deviations. We provide MCMC analysis using the orbital, vertical, and radial frequencies calculated in the previous section. The likelihood function λ has form,

$$\log \lambda = \log \lambda_{\mathrm{U}} + \log \lambda_{\mathrm{L}} \tag{1.34}$$

where $\log \lambda_{\mathrm{U}}$ denotes the likelihood of the upper and lower frequencies,

$$\log \lambda_{\mathrm{U}} = -\frac{1}{2}\sum_i \frac{\left(\nu^i_{\phi,\mathrm{obs}} - \nu^i_{\phi,\mathrm{th}}\right)^2}{\left(\sigma^i_{\phi,\mathrm{obs}}\right)^2} \tag{1.35}$$

where $\log \lambda_L$ is the probability (likelihood) of the lower frequency data.

$$\log \lambda_{\mathrm{L}} = -\frac{1}{2}\sum_i \frac{\left(\nu^i_{\mathrm{per,obs}} - \nu^i_{\mathrm{per,th}}\right)^2}{\left(\sigma^i_{\mathrm{per,obs}}\right)^2} \tag{1.36}$$

Here $\nu^i_{\phi,\mathrm{obs},}, \nu^i_{\mathrm{per,obs}}$ are direct observational results of the orbital/Keplerian frequencies (ν_{K}), periastron precession frequencies $\nu_{\mathrm{per}} = \nu_{\mathrm{K}} - \nu_{\mathrm{r}}$ for the source of our interest. On the other side, $\nu^i_{\phi,\,\mathrm{th}}, \nu^i_{\mathrm{per,th}}$ are the respective theoretical estimations.

Next, we perform the MCMC simulation to constrain the parameters ($M, B, q, r/M$) for black holes in CDF. We use Gaussian priors based on parameter values from existing literature on QPO data processing. We sampled approximately 7×10^4 points for each parameter from a Gaussian prior distribution. This allowed us to explore the physically possible parameter space within set boundaries and identify the best-fitting parameter values.

Parameter	**XTE J1550-564**		**GRO J1655-40**		**GRS 1915-105**		**SgrA^***		**M82 X-1**	
	μ	σ	μ	σ	μ	σ	μ	σ	μ	σ
$\boldsymbol{M/M_\odot}$	16.46	1.5	15.26	0.8	20.3	1.7	$1.7 \times 10^$	$0.2 \times 10^$	661.37	65
$\boldsymbol{B/10^{-5}}$	8.7	0.9	5	0.6	9.33	1.1	5	0.6	9.11	1.0
$\boldsymbol{q}$	0.83	0.085	0.65	0.07	0.85	0.08	0.96	0.01	0.85	0.07
$\boldsymbol{r}$	4.5	0.5	3	0.35	3.48	0.4	4.14	0.44	3.52	0.35

Table 1.2: The Gaussian prior of the dusty BH spacetime for the microquasars and Galactic center.

Parameters	XTE J1550-564	GRO J1655-40	GRS 1915 - 105	SgrA^*	M82 X-1
$M/M_\odot$	$16.458^{+1.498}_{-1.490}$	$15.259^{+0.799}_{-0.794}$	$20.300^{+1.694}_{-1.693}$	$(2.103^{+0.143}_{-0.131}) \times 10^6$	$555.3^{+20.365}_{-21.058}$
$B \times 10^{-5}$	$8.698^{+0.901}_{-0.895}$	$5.311^{+0.594}_{-0.595}$	$9.340^{+1.100}_{-1.100}$	$5.453^{+0.576}_{-0.577}$	$8.925^{+0.997}_{-1.005}$
q	$0.829^{+0.084}_{-0.084}$	$0.651^{+0.070}_{-0.070}$	$0.851^{+0.080}_{-0.080}$	$0.953^{+0.010}_{-0.010}$	$0.847^{+0.068}_{-0.069}$
r	$4.496^{+0.497}_{-0.498}$	$3.057^{+0.347}_{-0.346}$	$3.488^{+0.400}_{-0.400}$	$4.223^{+0.436}_{-0.431}$	$3.413^{+0.336}_{-0.332}$

Table 1.3: Best-fit values of M, B, q and r parameters for XTE $J1550-564$, GRO J1655-40, GRS $1915-105$, SgrA^*&M82$X-1$.

In Figs. 1.15, we show the results of the MCMC analysis of the Chaplygin CDM model parameters by using the QPO data from five different black holes (three stellar-

mass black hole candidates, one intermediate-mass and supermassive black holes). We use the emcee package to obtain the posterior distribution with the possible choice of the prior given in Table 1.2. In the analysis, the contour plots highlight the confidence levels ($1\sigma(68\%)$,2σ (95%) and 3σ (99%) of the posterior probability distributions for the entire set of parameters. The shaded regions on the contour plots reflect these confidence levels.

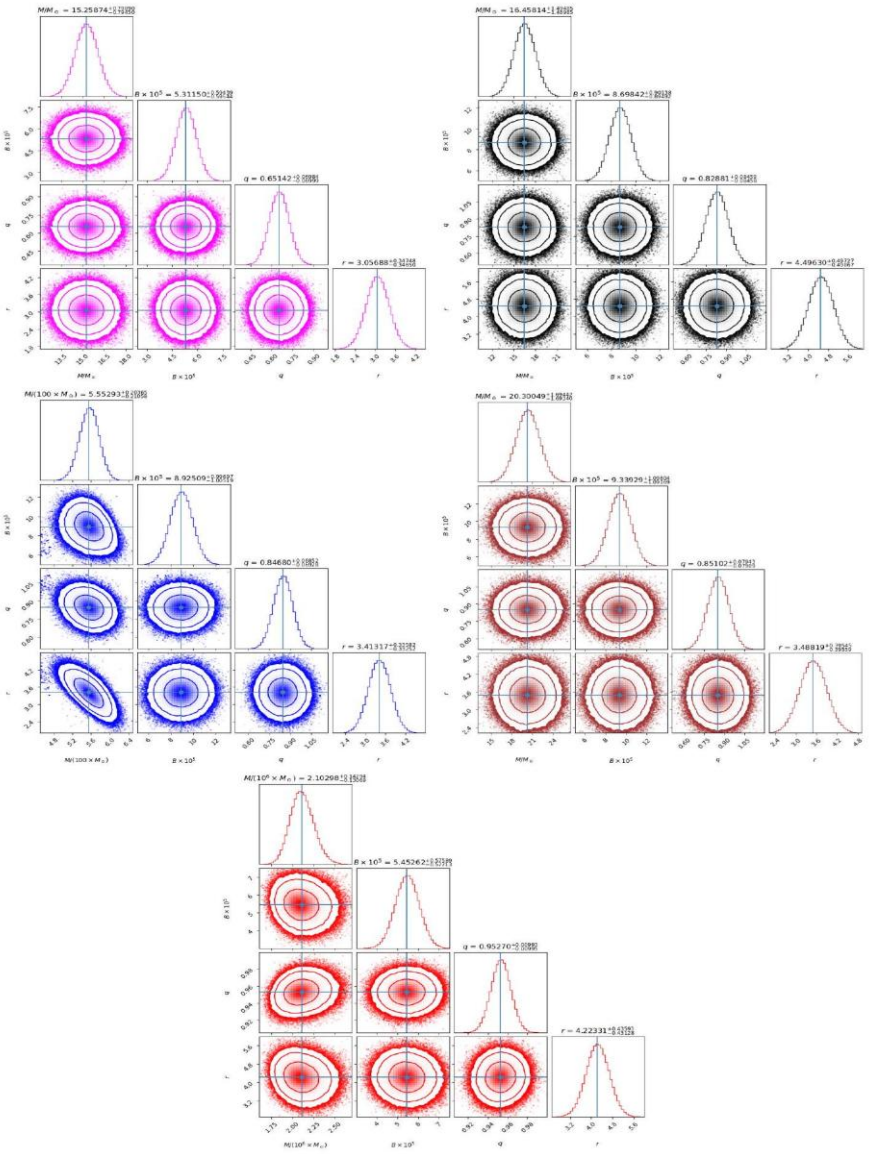


Figure 1.15: Constraints on the Chapligyn EoS model of CDM parameters, the black hole mass, and the radius of the QPO orbit from a four-dimensional MCMC analysis using the QPO data for the stellar-mass black hole GRO J1655-40, XTE J1550-564, M82 X-1, GRS 1915-105, Sgr A* in the RP model.

1.7 Conclusion

One can probe dark fluids with different EoS and parameters to understand the nature of the universe's dark energy. This work investigates a Schwarzschild BH surrounded by a dark fluid with a Chaplygin-like EoS. We first explore how the dark fluid parameters affect the BH's horizon properties. The decrease in the EOS parameter causes the horizon to shrink. In contrast, the fluid's "density" causes it to increase. Also, there is a critical value in the EoS parameter q, which increases as the density increases.

Next, we studied the effective mass of spacetime and analyzed it under dark fluid parameters in the absence and presence of the parameter B. It is shown that the mass decreases in the stronger inner horizon. At $B = 0$, the mass change is more extensive than in the dark fluid case. We also calculate the scalar invariants of the BH spacetime, which demonstrate an increase in spacetime curvature as the dark fluid parameter rises. Next, we investigated the circular motion of the test particle around the BH . As part of our standard particle motion investigations, we analyzed the effective potential of the particles for circular motion, specific energy, and angular values that correspond to circular orbits with zero and non-vanishing values of the dark fluid intensity.

The energy and angular momentum of the particles in the circular orbits are measured in two cases: at $B \to 0$ and $B = 10^{-7}$, and it is shown that the minimum of the energy and angular momentum is increased due to an increase in the EoS parameter. We also study the innermost stable circular orbits (ISCO). Due to the presence of the dark fluid, we observe an outermost stable circular orbit (OSCO). This demonstrates that at a critical value of the dark fluid intensity parameter, ISCO and OSCO have the same radius. The dark fluid intensity parameter shows a maximum. It is obtained that an increase in q, r_{ISCO} decreases for a given value of B. However, it increases with an increase of B for a given value of q, reaching its maximum at the upper value of B. The upper value in B also increases due to an increase in q. Moreover, there are OSCOs in the presence of the B parameter because of the effect of the cosmological horizon. An increase in the q parameter causes an increase in the OSCO radius.

We calculate the frequency of Keplerian orbits and the particles' radial and vertical oscillations along stable circular orbits. We also used orbital data from hotspots near Sgr A* to obtain upper and lower values for the EoS parameter. The orbital radius and period were shown for various values of the EoS and intensity parameters. We also got upper and lower values for the intensity parameter q by looking at orbital data from hotspot observations around the supermassive BHBHSgrA*. It is observed that at $B \to 0$, the lower and upper values of $q \simeq 0.65 \div 0.8$, while at $B = 10^{-7}$, the values range from 0.52 to 0.65 . The graph Ω_r increases with an increase in q, while the EoS parameter causes a decrease. We also looked at data from QPOs to find the relationships between GRS J1915-105 and XTE 1550-564's mass and EoS parameters in the RP, WD, and ER2-4 models. A test stellar-mass BH with the mass $M = 5M_{\odot}$ compares the twin peak QPOs around the BH with the metric 1.1 and plots. According to the analyses, there are no LF QPOs in the presence of q. An increase in the EoS parameter B causes a rise in the upper and lower frequencies near the kilohertz band. However, with the q parameter, the frequencies decrease. This means there are inverse relations between the parameters B and q, providing the same upper and lower frequencies. Analyses of the QPO orbits have shown that the parameter q increases the QPO radius decrease and comes close to the ISCO. According to the RP, ER3, and ER4 models, the orbit almost coincides with the ISCO. Finally, we have performed a detailed MCMC analysis of the Chaplygin CDM model parameters using the observational data from the twin-peak QPOs observed in the stellarmass black hole candidates in microquasars GRO J1655-40, XTE-J 1550564 & GRS 1915-105, the intermediate-mass black hole in M82-X1, and the supermassive black hole SgA* in the Milky Way galaxy in Figs. 1.15. More information on the best-fit values of these three parameters is given in Tab. 1.3.

Chapter 2: Black holes coupled to nonlinear electrodynamics and perfect fluid dark matter: Spacetime Stability and Thermodynamics

2.1 Introduction

Black holes are among the most challenging and still debated aspects of Einstein's theory of relativity. Regular or non-singular black holes have been predicted using certain energy-momentum tensors, resulting in secondary consequences. Recent research suggests that violating the strong energy condition is a crucial characteristic of regular black holes. The hunt for regular black holes began with Sakharov and Gliner [118,119], who hypothesized that using an environment with a de Sitter metric rather than a vacuum may prevent the occurrence of singularities. Gurevich and Starobinsky [120,121] postulated a complex interaction between gravitational and electromagnetic fields.

Nonlinear electrodynamics (NED) can generate fields that may be coupled to potential gravitational sources, especially in the neighborhood of gigantic entities like black holes. Under these circumstances, the gravitational field functions as a generator of electromagnetic fields, intensifying them and affecting the curvature of spacetime [122]. The motion of charged particles in their vicinity may be explained using a NED. Therefore, it is essential to study a black hole in General Relativity (GR) connected to NED [123].

According to recent cosmological investigations, the mainstream model of cosmology claims that dark energy (DE) accounts for almost 68.3% of our cosmos, while dark matter (DM) accounts for 26.8%. The baryon matter makes up the remaining 4.9% [124]. We infer the presence of DM in the visible cosmos from indirect evidence. As we go farther from the galactic center, its prevalence increases. These assumptions are concluded from the analysis of galaxy rotation [125].

Consequently, there is a need to examine black hole solutions encompassed by DE or DM, a topic that has recently received significant interest from researchers. Kiselve, for the first time, investigated the Schwarzschild black hole surrounded by

quintessential energy, and this study was later expanded to include the Kerr-like black hole in [126]. The perfect fluid dark matter (PFDM) model is a phenomenological framework containing a non-zero DM component represented by a logarithmic term $\alpha \ln\left(r/r_q\right)$. Rehaman et al. [127] constructed a PFDM model and examined the energy density, pressure, and equation of the DM. Li and Yang [128] provide an alternative black hole solution consisting of the term $\left(r_q/r\right)\ln\left(r/r_q\right)$. They do this by emphasizing that the DM halo, represented by a phantom scalar field, is composed of heavy particles with weak interactions with the equation of state. Since the phantom scalar field plays no role in the cosmos, thus this paradigm classifies background matter dispersion as DM. The contents of DE, such as a quintessence field or a cosmological constant, significantly impact the geometry of spacetime, particularly in the context of black holes. Therefore, in light of their approach, various astrophysical black hole characteristics have been explored in different DE and DM scenarios [129-138].

Black holes are famous for their strong gravitational attractions and thermodynamics. Bardeen et al. introduce the four laws of black hole thermodynamics. In physics, thermodynamics is helpful due to its inherent features. This lets us study a system's macroscopic physics without knowing its details. Hawking showed that black holes produce semiclassical thermal radiation like pure black bodies [139]. Schwarzschild black holes have a negative heat capacity and are unstable due to thermal fluctuations since their Hawking temperatures are inversely proportional to mass. These characteristics attracted many researchers to explore black hole thermodynamics for better understanding [140-144].

2.2 Black holes in GR coupled to NED surrounded by PFDM

In the context of black hole solutions, researchers often study black hole behavior in different theoretical frameworks or gravitational backgrounds. This could involve exploring various metrics that describe spacetime geometry around black holes, such as the Schwarzschild metric for non-rotating black holes or the Kerr metric for rotating black holes.

2.2.1 Black hole solutions with the dark fluid equation of state

The present section briefly introduces a black hole solution in GR coupled with the NED field and PFDMin a spherically symmetric spacetime with the ansatz

$$ds^2 = -e^{\nu(r)}dt^2 + e^{\Lambda(r)}dr^2 + r^2(d\theta^2 + \sin^2\,\theta d\phi^2) \tag{2.1}$$

Nonsingular (regular) extensions of black hole spacetimes have been widely considered in GR coupled to NED [145-152]. But, here, we focus on a new black hole solution in GR coupled with NED in the presence of an external matter fields field called the PFDM field using the following corresponding action:

$$\mathcal{S} = \frac{1}{16\pi}\int\ d^4x\sqrt{|g|}(\mathrm{R} - \mathcal{L}_{\mathrm{NED}} + \mathcal{L}_{\mathrm{PFDM}}) \tag{2.2}$$

where, R is the Ricci scalar, g is determinant of the metric tensor $g_{\mu\nu}$, NED field Lagrangian is given in Ref. [153]

$$\mathcal{L}_{\mathrm{NED}} = \frac{4\mu}{\alpha}\frac{(\alpha\,\mathrm{F})^{(\nu+3)/4}}{[1+(\alpha\mathrm{F})^{\nu/4}]^{1+\mu/\nu}} \tag{2.3}$$

with the coupling parameter α and the Faraday tensor of the electromagnetic field $\mathrm{F} = \mathrm{F}_{ab}\,\mathrm{F}^{ab}$. Since there is no matter Lagrangian, the energy-momentum tensor in Schwarzschild coordinates is due solely to $\mathcal{L}_{\mathrm{NED}}$ as

$$G_{\mu\nu} = R_{\mu\nu} - \frac{1}{2}Rg_{\mu\nu} = T_{\mu\nu}^{(\mathrm{NED})} + T_{\mu\nu}^{(\mathrm{PFDM})} \tag{2.4}$$

where the perfect fluid energy-momentum tensor is

$$T_{\mu\nu}^{(\mathrm{PF})} = (\rho + p)u_\mu u_\nu + pg_{\mu\nu}, \tag{2.5}$$

which, in the case of PFDM, has only the standard orthogonal basis

$$T_{\mu\nu}^{(\mathrm{PFDM})} = \mathrm{diag}\big(-\epsilon, p_r, p_\theta, p_\phi\big) \tag{2.6}$$

with

$$-\epsilon = p_r = \frac{\lambda}{8\pi r^3}, p_\theta = p_\phi = -\frac{\lambda}{16\pi r^3} \tag{2.7}$$

The energy-momentum tensor for the NED reads as,

$$4\pi T_{\mu\nu}^{(\mathrm{NED})} = -2\frac{\partial\mathcal{L}_{\mathrm{NED}}}{\partial F}F_\mu^\beta F_{\nu\beta} + \mathcal{L}_{\mathrm{NED}}g_{\mu\nu} \tag{2.8}$$

The non-zero diagonal components of the tensor for the NED field are

$$T_0^0 = T_1^1 = -\frac{2\mu M q^\nu r^{\mu-3}}{(q^\nu + r^\nu)^{\frac{\mu+\nu}{\nu}}} \tag{2.9}$$

$$T_2^2 = T_3^3 = \frac{\mu M q^\nu r^{\mu-3}}{(q^\nu + r^\nu)^{\frac{\mu}{\nu}+2}}[(\nu+1)r^\nu - (\mu-1)q^\nu] \tag{2.10}$$

To solve this field equation, first, we find the component G_{tt} of the Einstein tensor using the following ansatz

$$e^{\nu(r)} = e^{-\Lambda(r)} = f(r) \tag{2.11}$$

and we get

$$G_0^0 = G_1^1 = -\frac{1}{r}\frac{df(r)}{dr} - \frac{f(r)}{r^2} + \frac{1}{r^2} \tag{2.12}$$

$$G_2^2 = G_3^3 = -\frac{1}{2}\frac{d^2 f(r)}{dr^2} - \frac{1}{r}\frac{df(r)}{dr} \tag{2.13}$$

For a static and spherically symmetric spacetime with line element Eq. (2.1) and NED source given by a magnetic charge q in which $F_{\mu\nu} = \left(\delta_\mu^\theta \delta_\nu^\phi - \delta_\nu^\theta \delta_\mu^\phi\right) q \sin\theta$. One can have the following differential equation for the metric function $f(r)$, using Eq.(2.4) and taking into account Eqs. (2.6), (2.9) and (2.12):

$$\frac{1}{r}\frac{df(r)}{dr} + \frac{f(r)}{r^2} + \frac{1}{r^2} = \frac{2\mu M q^\nu r^{\mu-3}}{(q^\nu + r^\nu)^{\frac{\mu+\nu}{\nu}}} - \frac{\lambda}{8\pi r^3} \tag{2.14}$$

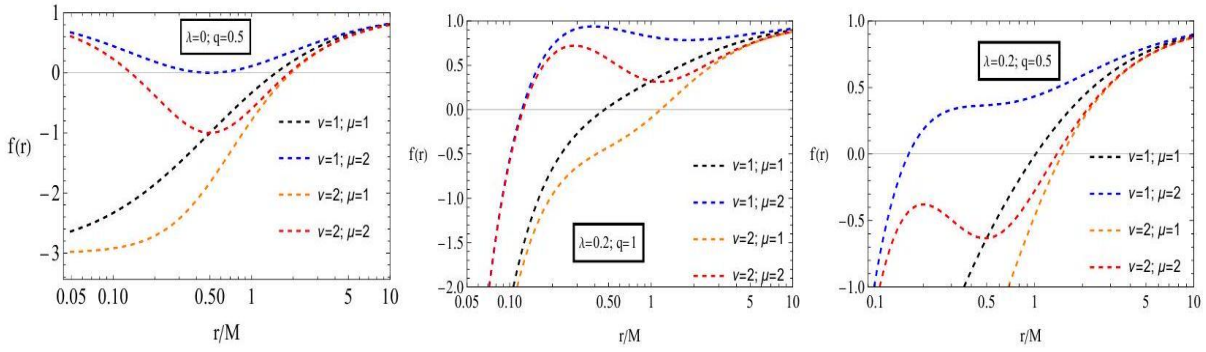


Figure 2.1: Radial dependence of the metric function $f(r)$ for various values of q and λ and fixed values of μ and ν.

Fig. 2.1 shows how the metric function $f(r)$ around the black hole changes under different parameter influences. Increasing the NED parameters reduces spacetime curvature, making the black hole more stable. A higher charge strengthens the electromagnetic field, expanding the event horizon. PFDM causes spacetime to extend and diminishes dynamic effects outside the black hole. These graphs highlight the interplay of these factors, providing insights into the structure of spacetime surrounding the black hole.

The solution of Eq.(2.14) takes the form,

$$f(r) = \frac{-2Mr^{\mu}(q^{\nu} + r^{\nu})^{-\frac{\mu}{\nu}} + \lambda \ln\, r + r}{r} + \frac{c_1}{r} \tag{2.15}$$

After simplifying Eq. (2.15) we can get the following form,

$$f(r) = 1 - \frac{2M}{r}\left(1 + \frac{q^{\nu}}{r^{\nu}}\right)^{-\frac{\mu}{\nu}} + \frac{\lambda \ln\, r}{r} + \frac{c_1}{r}. \tag{2.16}$$

Noting that a quantity in the logarithmic term should be dimensionless. Therefore, we chose the constant as $c_1 = -\lambda \ln\, |\lambda|$, and we get the following form for the metric function:

$$f(r) = 1 - \frac{2M}{r}\left(1 + \frac{q^{\nu}}{r^{\nu}}\right)^{-\frac{\mu}{\nu}} + \frac{\lambda}{r} \ln\, \frac{r}{|\lambda|}. \tag{2.17}$$

Now, we analyze the horizon properties of the obtained black hole solution graphically.

The given set of graphs in Fig.2.2 represents the radius of the event horizon r_H versus different parameters (λ and q) for various combinations of the parameters ν and μ. The upper row shows r_H versus λ, and the bottom row shows r_H versus q. Each column corresponds to different values of ν and μ. The color panel on the right side of each graph shows the value of the

third parameter, λ and q. The radius of the event horizon has a minimum value of a certain value of λ. The curves show all graphs. This minimum value varies according to the values of ν and μ. As the value increases, the initial value of the event horizon radius, r_H, increases on the graphs. It shows that increasing ν causes the black hole to

grow larger. An increase in the value of μ also increases the value of r_H, but this effect is weaker than the impact of ν. The U-shaped curves show the radius of the minimum event horizon as λ changes. This minimum value is reached at a certain value of λ, which varies for different parameters ν and μ.

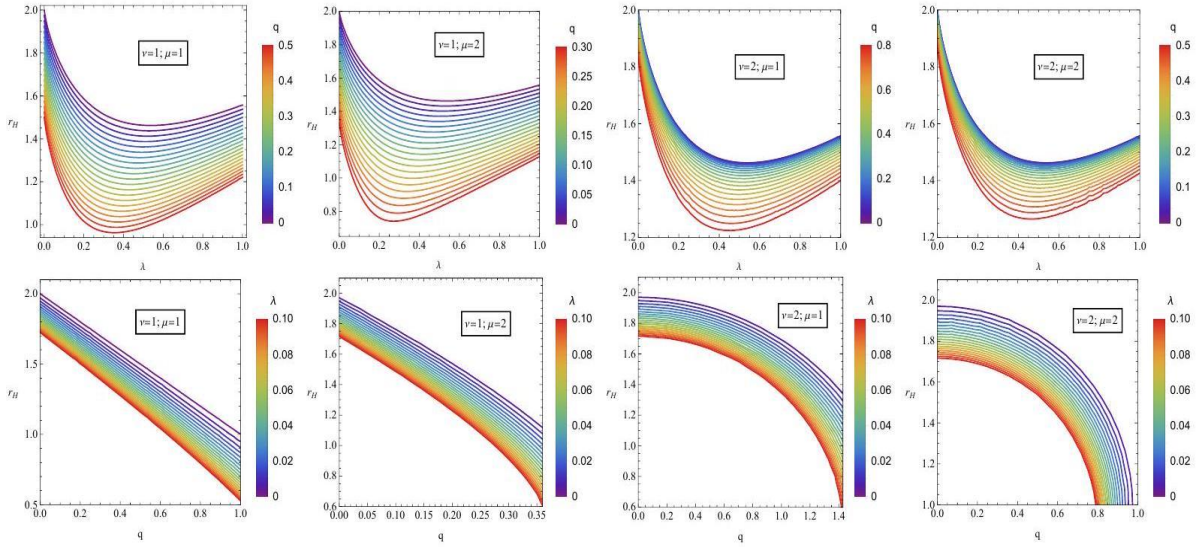


Figure 2.2: The Event horizon radius for q and λ.

The graphs show that an increase in λ first decreases and then increases the radius of the event horizon. All graphs show that with increasing q, the radius of the event horizon r_H generally decreases. This means that an increase in magnetic charge shrinks the radius of the black hole's event horizon.

2.3 Energy conditions

Energy conditions are handy tools for discussing cosmological geometry and black hole spacetimes [154-156] in both general relativity [157] and modified gravity [158]. In the models of NED and PFDM, it is essential to consider energy conditions to understand how gravity, electromagnetic fields, and dark matter behave. Energy conditions are fundamental constraints that ensure matter and energy's physical consistency and stability in theoretical physics and cosmology.

These conditions impose restrictions on the stress-energy tensor, providing a framework to analyze gravitational phenomena without requiring detailed knowledge of the underlying matter dynamics. In the context of NED and PFDM, energy

conditions are essential for understanding the interplay between gravity, electromagnetic fields, and dark matter [159]. The four primary energy conditions, WEC, NEC, DEC, and SEC, are particularly significant to study spacetime properties. They ensure non-negative energy densities, causal energy flow, and physically realistic gravitational effects. Additionally, these conditions enable the derivation of significant results, such as singularity theorems, black hole topology theorems, and constraints on cosmic expansion [160]. In NED, energy conditions regulate the behavior of nonlinear electromagnetic fields, preventing unphysical scenarios such as negative energy regions or superluminal propagation. In PFDM, they constrain the properties of dark matter, ensuring its compatibility with observational data and its role in shaping cosmic structures. Together, these frameworks provide a robust foundation for exploring the intricate dynamics of spacetime and the universe's evolution [161]. The standard energy conditions include NEC, WEC, SEC, and DEC, given as

$$\text{NEC:} \quad \rho + p_i \geq 0 (i = r, \theta, \phi)$$
$$\text{WEC:} \quad \rho \geq 0 \& \rho + p_i \geq 0 (i = r, \theta, \phi)$$
$$\text{SEC:} \quad \rho + \sum_i p_i \geq 0 \& \rho + p_i \geq 0 (i = r, \theta, \phi)$$
$$\text{DEC:} \rho \geq 0 \& |p_i| \leq \rho (i = r, \theta, \phi) \quad (2.18)$$

Relevant quantities are deduced as

$$\rho = -\frac{2\mu M q^{\nu} r^{\mu}}{r^3 (q^{\nu} + r^{\nu})^{\frac{\mu+\nu}{\nu}}} + \frac{\lambda}{8\pi r^3}$$
$$\rho + p_r = 0$$
$$\rho + p_{\theta,\phi} = -\frac{((\mu+1)q^{\nu} - r^{\nu}(\nu-1))\mu M q^{\nu} r^{\mu}}{r^3 (q^{\nu} + r^{\nu})^{\frac{\mu}{\nu}+2}} + \frac{3\lambda}{16\pi r^3}$$
$$\rho + p_r + p_{\theta} + p_{\phi} = \frac{2((\nu+1)r^{\nu} - (\mu-1)q^{\nu})\mu M q^{\nu} r^{\mu}}{r^3 (q^{\nu} + r^{\nu})^{\frac{\nu}{\nu}+2}} + \frac{\lambda}{8\pi r^3}$$
$$\rho - |p_{\theta,\phi}| = \frac{((\mu-3)q^{\nu} - (\nu+3)r^{\nu})\mu M q^{\nu} r^{\mu}}{r^3 (q^{\nu} + r^{\nu})^{\frac{\mu}{\nu}+2}} + \frac{\lambda}{8\pi r^3}$$

To examine the energy conditions of NED and PFDM in our case, we plot the unspecified quantities in Eq. (2.19) concerning the radial coordinate r in Fig. 2.3.

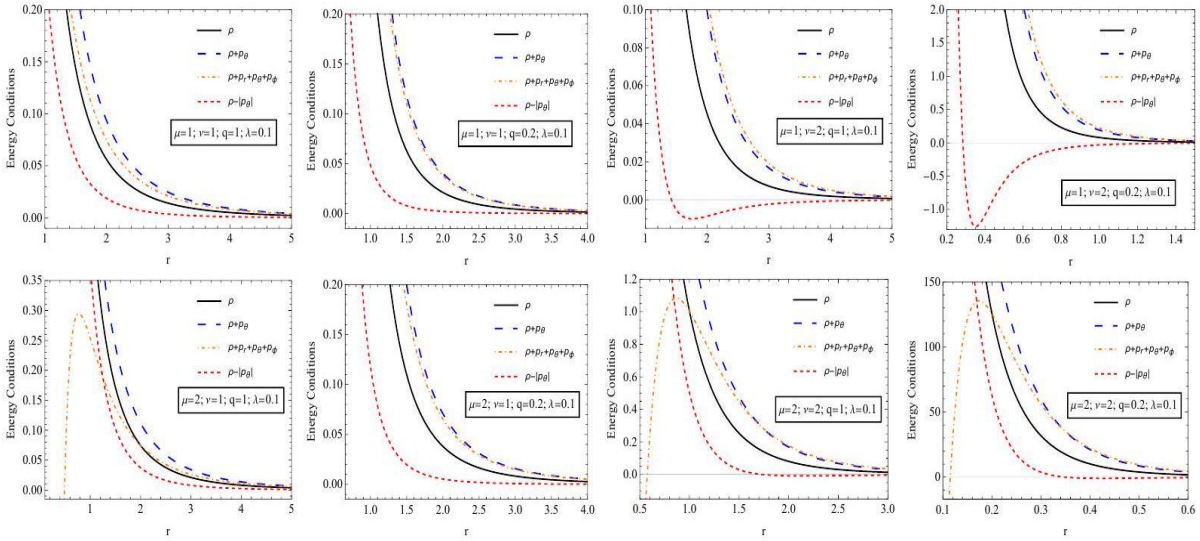


Figure 2.3: The variation of $\rho, \rho + p_\theta, \rho + p_r + p_\theta + \rho_\phi$ and $\rho - |p_\theta|$ versus r for NED and PFDM taking $\mathrm{q} = 1, \mathrm{q} = 0.2$ and $\lambda = 0.1$.

Fig. 2.3 shows the different energy states and the dependence of the different energy states on r for different sets of parameters. The graphs depict the distribution of energy density and pressure under the influence of various parameters. As the radius increases, all energy conditions decrease while they attain higher values at smaller distances. An increase in charge reduces energy density, and in some cases, it may become negative, indicating a stronger spacetime curvature due to the electromagnetic field. PFDM expands spacetime and slows down energy distribution changes, but some energy conditions may be violated at high values. The increase in NED parameters affects the internal structure of the black hole, stabilizing energy density and pressure at larger distances. These results are crucial for understanding the distribution of matter, electromagnetic fields, and dark matter around the black hole, revealing the possible existence of external matter fields or unstable structures in certain cases.

2.4 Thermodynamics of black holes surrounded by PFDM

Solving the equation $f(r_h) = 0$, one can obtain the event horizon radius r_h, with which the mass of the black hole can be expressed as

$$M = \frac{1}{2}\left(1 + \frac{q^\nu}{r_h^\nu}\right)^{\frac{\mu}{\nu}}\left(r_h + \lambda \ln \frac{r_h}{|\lambda|}\right) \tag{2.20}$$

The Hawking temperature T_h is related to the surface gravity by:

$$T_h = \frac{f'(r)}{4\pi}\bigg|_{r=r_h} = \frac{1}{4\pi}\left[\frac{2M}{r_h^2}\left(1+\frac{q^\nu}{r_h^\nu}\right)^{-\frac{\mu}{\nu}} + \frac{2M\mu q^\nu}{r_h^{2+\nu}} \times \left(1+\frac{q^\nu}{r_h^\nu}\right)^{-\frac{\mu}{\nu}-1} - \frac{\lambda}{r_h^2}\left(1+\ln\frac{r_h}{|\lambda|}\right)\right] \quad (2.21)$$

In Fig. 2.4, we plot the temperature of the black hole with NED charge surrounded by PFDM. We can see that the black hole temperature increases and reaches a maximum before having a phase of decrease. Furthermore, this figure shows us that this maximum increases for higher values of the dark matter parameter λ. Let us notice that the case " $\lambda = 0$ " corresponds to the temperature of a black hole without dark matter. We write the first law of black hole thermodynamics from the black hole studied here and then find the entropy before computing the corrected entropy. The first law is expressed as

$$dM = T_h dS_0 + \Phi_h dq + \beta_h d\lambda \quad (2.22)$$

where S_0 represents the entropy at the equilibrium without considering thermal fluctuation or the uncorrected entropy.

It should be emphasized that the entropy variation in Eq. (2.22) is not independent of the horizon variation. For fixed magnetic charge q and fixed dark matter parameter λ, the first law reduces to $dM = T_h\, dS_0$. Since the mass parameter is expressed as a function of the horizon radius, $M = M(r_h, q, \lambda)$, the entropy variation can be written as $dS_0 = (1/T_h)(\partial M/\partial r_h)_{q,\lambda}\, dr_h$. Therefore, when the mass changes, the corresponding change of the event horizon is automatically taken into account through dr_h. If the event horizon decreases along a given thermodynamic branch, the entropy variation follows from the sign of dS_0/dr_h. Thus, the entropy change is not neglected; it is encoded in the horizon dependence of M, T_h, and S_0.

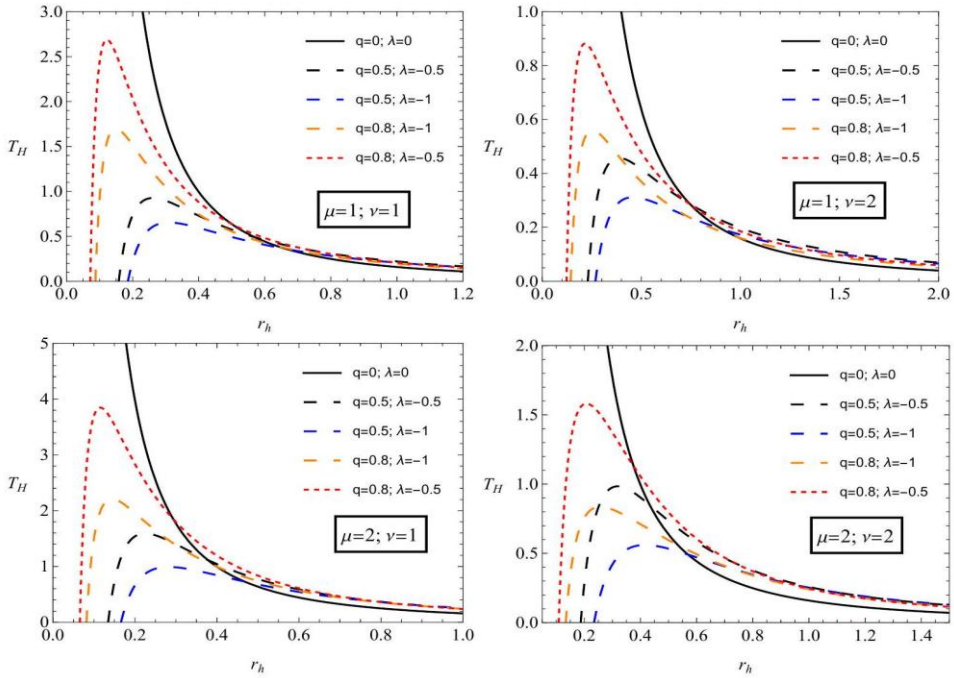


Figure 2.4: The black hole temperature T_h as a function of the event horizon radius r_h, showing the effects of the dark matter parameter λ and the black hole charge q on thermal evolution

Let us notice that S_0, the magnetic charge q, and the dark matter parameter α form a complete set of extensible variables. T_h is the Hawking temperature at the horizon and Φ_h is the potential. β_h is the conjugating quantity of the dark matter parameter λ. In deriving Eq. (2.23), we consider the canonical thermodynamic path in which the parameters q and λ are kept fixed. Therefore, the work terms $\Phi_h dq$ and $\beta_h d\lambda$ vanish, and only the horizon variation contributes to the entropy change. Now, in the first expression of (2.22), we can find the formula of the uncorrected entropy S_0, given by

$$S_0 = \int \frac{1}{T_h} dM = \int \frac{1}{T_h} \frac{\partial M}{\partial r_h} dr_h \qquad (2.23)$$

To compute this, we have to find $\frac{\partial M}{\partial r_h}$ from Eq.(2.23). The obtained expression is as follows

$$\frac{\partial M}{\partial r_h} = \frac{1}{2}\left(1+\frac{q^\nu}{r_h^\nu}\right)^{\frac{\mu}{\nu}}\left(1+\frac{\lambda}{r_h}\right) - \frac{\mu q^\nu}{2r_h^{\nu+1}}\left(1+\frac{q^\nu}{r_h^\nu}\right)^{\frac{\mu}{\nu}-1}\left(r_h+\lambda \ln\frac{r_h}{|\lambda|}\right)2 \qquad (2.24)$$

Introducing Eq.(2.24) and (2.21) into Eq. (2.23), we get the black hole entropy at the equilibrium expressed as

$$\begin{aligned} S_0 = {} & \frac{2\pi\left(1+\frac{q^\nu}{r_h^\nu}\right)^{\frac{\mu}{\nu}}}{(q^\nu+r_h^\nu)\left(q^\nu\lambda\left(-1+\mu\ln\frac{r_h}{|\lambda|}\right)+q^\nu(1+\mu)r_h-\lambda r_h^\nu+r_h^{1+\nu}\right)^2} \\ & \times [r_h^{3\nu}(r_h^2-2\lambda r_h-\lambda^2)+q^{3\nu}(\lambda^2(\mu-1)-2\lambda(1+\mu^2)r_h) \\ & -6\lambda r_h+(3+\mu(-1+2\nu))r_h^2)+q^{2\nu}\lambda^2\mu^2\ln\frac{r_h}{|\lambda|}(q^\nu(\mu-1)-r_h^\nu) \\ & +2q^\nu\lambda\mu\ln\frac{r_h}{|\lambda|}(q^{2\nu}(\lambda-\lambda\mu+(1-\mu+\mu^2)r_h)+r_h^{2\nu}(\lambda+(1+\nu)r_h) \\ & +q^\nu r_h^\nu(-\lambda(\mu-2)+(2-\mu+\nu)r_h))] \end{aligned} \qquad (2.25)$$

Here, we can see that this result is the same as obtained in the presence of quintessence dark energy found in Ref. [162, 163]. As a result, we can say that perfect fluid dark matter does not affect the evolution of the entropy of a non-linear black hole.

Now, we will compute the corrected entropy at the equilibrium S , for which the general formula is expressed as

$$S = S_0 - \beta \ln(S_0 T_h) \qquad (2.26)$$

Here, β is the corrected parameter with only two values. If $\beta = 0$, Eq.(2.26) describes the uncorrected entropy, and for $\beta = 1/2$, Eq.(2.26) represents the corrected entropy due to thermal fluctuation.

The logarithmic correction in Eq. (2.26) should be understood as a perturbative thermal-fluctuation correction valid away from the exact extremal limit. In the extremal limit $T_h \to 0$, the term $\ln(S_0 T_h)$ becomes singular, and therefore Eq. (2.26) should not be used to describe the exact zero-temperature state. For this reason, the present analysis does not claim a direct verification of the strong form of Nernst's theorem. Rather, the corrected entropy is considered for non-extremal black holes with $T_h > 0$, where thermal fluctuations are well defined.

From the plot Fig. 2.5, one can compare the corrected and equilibrium entropy for a given black hole. In the absence of the correction parameter β, the equilibrium entropy of the system is a linearly increasing function, as shown in the bottom. For the correction parameter $\beta = 1/2$, the corrected entropy of the system always has a positive value, which is important for the system. The corrected entropy is a decreasing function below the critical horizon radius, but above this point is always an increasing function. Therefore, for a larger black hole, the corrected entropy of the system is not significant as expected. However, for a smaller black hole system, the correction term significantly affects the system's entropy due to small thermal fluctuations.

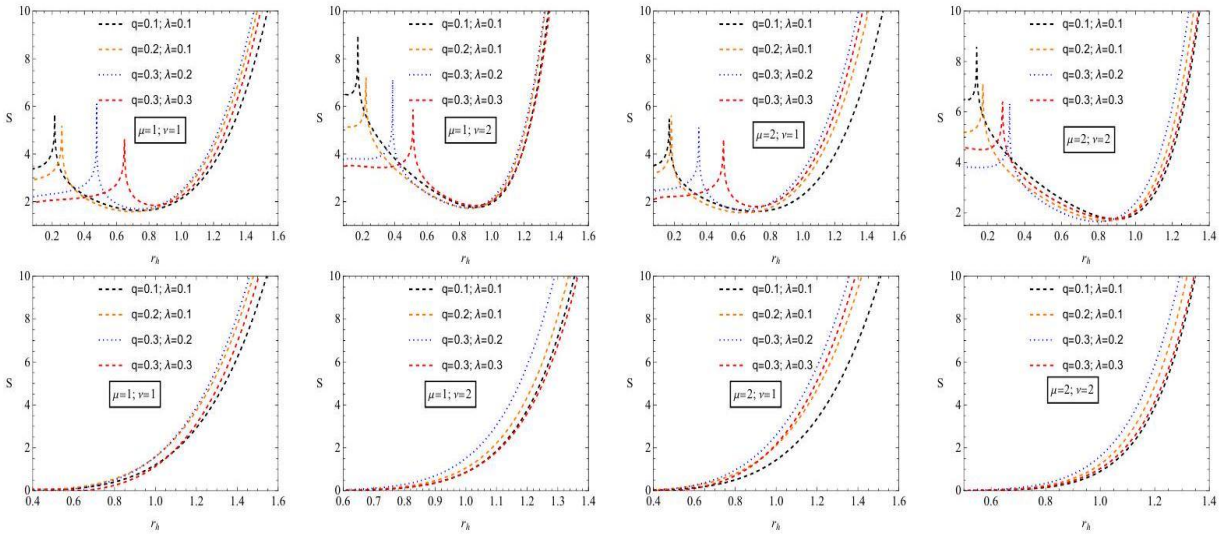


Figure 2.5: Variation of entropy (S) with black hole horizon radius ($r+$) for different values of q and λ. Here $\beta = 0$ (no correction) is the bottom panel and $\beta = 1/2$ (with correction) is the top panel.

Since both S and T_h are functions of the horizon radius, the heat capacity should be evaluated as $C = T_h(\partial S/\partial T_h)q,\lambda = T_h\,[(\partial S/\partial r_h)q,\lambda\,/\,(\partial T_h/\partial r_h)q,\lambda]$. For the corrected entropy $S = S_0 - \beta\,\ln(S_0T_h)$, one obtains $\partial S/\partial r_h = \partial S_0/\partial r_h - \beta[(1/S_0)(\partial S_0/\partial r_h) + (1/T_h)(\partial T_h/\partial r_h)]$. Therefore, the heat capacity takes the form $C = T_h\,\{\partial S_0/\partial r_h - \beta[(1/S_0)(\partial S_0/\partial r_h) + (1/T_h)(\partial T_h/\partial r_h)]\}\,/\,(\partial T_h/\partial r_h)$. For $\beta = 0$, this expression reduces to the uncorrected heat capacity.

The specific heat C at constant volume is given by:

$$C = T_h\left(\frac{\partial S}{\partial T_h}\right) \tag{2.27}$$

We need the relationship between the entropy S and the Hawking temperature T_h, which involves the implicit dependence on r_h.

We need:

$$\frac{dS_0}{dr_h} = 2\pi r_h \tag{2.28}$$

Then, we have

$$\left.\frac{dT_h}{dr}\right|_{r=r_h} = \frac{1}{4\pi}\left[\frac{d}{dr_h}\left(\frac{2M}{r_h^2}\left(1+\frac{q^\nu}{r_h^\nu}\right)^{-\frac{\mu}{\nu}}\right)\right.$$
$$\left. + \frac{d}{dr_h}\left(\frac{2M\mu q^\nu}{r_h^{2+\nu}}\left(1+\frac{q^\nu}{r_h^\nu}\right)^{-\frac{\mu}{\nu}-1}\right) - \frac{d}{dr_h}\left(\frac{\lambda}{r_h^2}\left(1+\ln\frac{r_h}{|\lambda|}\right)\right)\right] \tag{2.29}$$

Finally, the specific heat is:

$$C = T_h\frac{dS}{dr_h}\left(\frac{dr_h}{dT_h}\right) \tag{2.30}$$

After computing it, we get the following expression

$$C = \frac{A}{B}$$
$$A = -2\pi r_h^2(q^\nu + r_h^\nu)\left(q^\nu\lambda\left(\mu\ln\frac{r_h}{|\lambda|} - 1\right) + q^\nu(1+\mu)r_h - \lambda r_h^\nu + r_h^{1+\nu}\right)$$
$$B = r_h^{2\nu}(r_h - 2\lambda) + q^{2\nu}(r_h - 2\lambda + (r_h+\lambda)\mu) + q^\nu r_h^\nu$$
$$\times(\lambda(\mu-4) + r_h(2+\mu+\mu\nu)) + q^\nu\lambda\mu(2q^\nu + r_h^\nu(2+\nu))\ln\frac{r_h}{|\lambda|} \tag{2.31}$$

A black hole undergoes a second-order phase transition in phase transitions that lead the black hole to move from the stable phase ($C > 0$) to the unstable phase ($C < 0$).

Figure 2.6 presents the variation of the black hole heat capacity C as a function of the horizon radius, demonstrating the thermodynamic stability of the black hole solution under different values of the charge and the PFDM parameter. One can observe

from the plots the presence of discontinuities in the heat capacity, which indicate second-order phase transitions. These transitions separate different thermodynamic phases: The heat capacity is negative for small black holes (r_h below the discontinuity point), implying that they are thermally unstable. This corresponds to an evaporating phase, in which the black hole loses mass via Hawking radiation. The heat capacity for large black holes (r_h above the transition point)

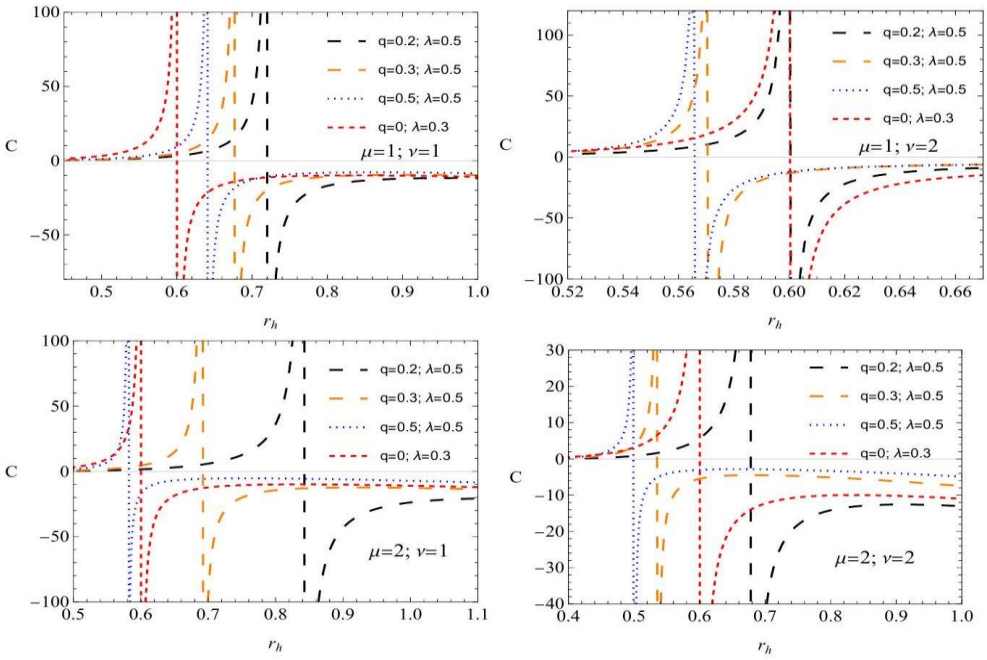


Figure 2.6: Change of the heat capacity C of the non-linear black hole in the background of perfect fluid dark matter becomes positive, signaling a stable equilibrium phase where the black hole can maintain thermal stability.

Increasing the black hole charge shifts the phase transition point, suggesting that stronger NED effects influence the black hole's thermodynamic structure. The increase in charge leads to a more extended stable phase, reducing the likelihood of black hole evaporation. Increasing the PFDM parameter significantly alters the stability properties. A higher value of it shifts the phase transition to a larger event horizon, implying that the presence of PFDM supports stability for larger black holes. This suggests that black holes embedded in PFDM environments are more resistant to evaporation than those in vacuum or standard dark matter models. From an

astrophysical perspective, these findings suggest that black holes in environments with significant PFDM influence may have longer lifetimes as the transition to a stable thermodynamic phase occurs at a larger horizon radius. Moreover, PFDM modifies the black hole's thermal response, potentially affecting accretion disk dynamics, black hole mergers, and observational signatures related to thermal fluctuations.

A well-defined second-order phase transition strengthens the argument that such black holes exhibit non-trivial stability properties, distinguishing them from classical Schwarzschild or Reissner-Nordström black holes. Future observational tests, such as those involving black hole shadow measurements or X-ray spectra from accretion disks, could constrain the parameters q and λ based on their effects on stability and evaporation rates.

2.5 Conclusion

This study investigated the properties of black holes in GR coupled to NED in the presence of PFDM. The main results obtained across different sections are summarized below: A singular black hole solution was derived, incorporating the effects of NED and PFDM. The energy conditions, including the WEC, NEC, SEC, and DEC, are examined. It was observed that as the radius increases, all energy conditions decrease. Higher charge values reduce energy density and sometimes lead to negative energy densities, indicating the influence of strong spacetime curvature. The PFDM parameter increase slows energy distribution changes, whereas NED parameters stabilize energy density at more considerable distances.

The thermodynamic properties, including temperature, entropy, and specific heat, are analyzed. The specific heat capacity transitioned from positive to negative values, suggesting stability and phase transition behavior in particular parameter ranges. PFDM and NED modified the black hole's Hawking temperature, indicating changes in its thermodynamic equilibrium.

The results demonstrate that nonlinear electrodynamics and perfect fluid dark matter significantly affect the physical properties of black holes within general

relativity. In particular, the dependence of the energy conditions on the charge and PFDM parameters has been analyzed. Noticeable deviations from the standard vacuum black-hole behavior arise due to the coupling of the gravitational field with nonlinear electrodynamics and external matter fields. The variations of the Hawking temperature, entropy, and specific heat reveal the existence of thermodynamically stable and unstable regions.

The study provides a useful framework for understanding black holes in general relativity coupled to nonlinear electrodynamics and phenomenological dark matter fields. The findings suggest that black holes surrounded by PFDM may exhibit modified thermodynamic and observational properties compared with their vacuum counterparts. Future black hole imaging and gravitational-wave observations may help test these effects. Further research is needed to explore the role of rotation, higher-order corrections, and more realistic matter distributions in these models. The results can also be extended to analyze accretion disk properties and their implications for high-energy astrophysics.

In conclusion, this work contributes to the understanding of black holes in general relativity coupled to nonlinear electrodynamics and external matter fields, and offers possible pathways for observational tests using astrophysical and cosmological data.

Chapter 3: Magnetically charged black holes surrounded by perfect fluid dark matter: radiation processes, particle dynamics, and quasiperiodic oscillations

3.1 Introduction

Black holes (BHs) represent one of the most intriguing and debated aspects of Einstein's theory of relativity. Regular or nonsingular black holes have been theorized using specific energy-momentum tensors, leading to secondary implications. Recent studies indicate that violating the strong energy condition is a key feature of regular black holes. The quest for regular black holes began with Sakharov and Gliner [118,119], who proposed that replacing a vacuum with a de Sitter metric environment could prevent the formation of singularities. Furthermore, Gurevich and Starobinsky [120,121] suggested a complex interplay between gravitational and electromagnetic fields in this context.

Recent cosmological investigations have led to a deeper understanding of the composition of our universe. According to the mainstream model of cosmology, dark energy (DE) constitutes approximately 68.3% of the total energy density of the cosmos, while dark matter (DM) accounts for about 26.8%. The remaining 4.9% comprises baryonic matter, including all visible matter such as stars, planets, and galaxies [124]. The existence of dark matter is inferred indirectly through its gravitational effects on visible matter, radiation, and the universe's large-scale structure. One of the key pieces of evidence for dark matter comes from the analysis of galaxy rotation curves. Observations show that the rotational velocities of galaxies do not decrease with distance from the galactic center as expected based on the distribution of visible matter alone. Instead, these velocities remain constant or even increase at larger radii, suggesting the presence of a significant amount of unseen mass-dark matter-that dominates in the outer regions of galaxies [125,164]. Furthermore, cosmic microwave background (CMB) radiation studies provide additional support for the dark matter hypothesis. The Planck satellite's measurements of CMB anisotropies indicate that dark

matter plays a crucial role in the formation and evolution of cosmic structures [124]. These findings align with simulations of large-scale structure formation, where dark matter is a scaffolding for baryonic matter to clump together and form galaxies. In addition to galaxy rotation curves and CMB data, other observational techniques, such as gravitational lensing and the dynamics of galaxy clusters, also point to the prevalence of dark matter. For instance, weak gravitational lensing surveys reveal distortions in the shapes of distant galaxies caused by the intervening mass of dark matter halos [125]. Similarly, observations of the Bullet Cluster-a system of two colliding galaxy clusters-provide direct empirical evidence for the separation of dark matter from baryonic matter, further confirming its existence [165]. Despite decades of research, the exact nature of dark matter remains one of the biggest mysteries in modern astrophysics. Various theoretical candidates, including Weakly Interacting Massive Particles (WIMPs), axions, and sterile neutrinos, have been proposed, but none have been conclusively detected yet. Experimental efforts, such as those using underground detectors and particle accelerators, continue to search for potential signals of dark matter interactions [166].

NED plays a crucial role in the interaction between electromagnetic fields and strong gravitational sources, particularly near BHs [167]. In such extreme environments, gravity enhances electromagnetic phenomena, influencing the motion of charged particles and sustaining fields through NED models [123, 168, 169]. Additionally, NED provides alternative frameworks that mitigate singularities in GR, addressing key issues like the information paradox and quantum gravity [170,171]. Beyond black holes, NED has been applied to cosmology, offering insights into inflation, dark energy, and dark matter dynamics [172,173]. It also helps explain ultra-strong magnetic fields observed in neutron stars and magnetars [174-176]. Moreover, incorporating NED into gravitational theories has led to solutions like regular black holes without singularities and studies on wormholes and external matter fields spacetime structures [177,178].

In studies on NED and PFDM, the effects of NED and PFDM models have been thoroughly investigated [179-181]. Additionally, orbital motions and epicyclic oscillations around Bardeen black holes have been analyzed under the influence of PFDM . NED models introduce corrections to classical electromagnetic theory, which can significantly alter the behavior of black holes and other compact objects. These changes affect the stability, shadow properties, and accretion processes around such objects, thereby influencing the distribution and dynamics of dark matter in their vicinity. PFDM is used as a phenomenological model to describe dark matter halos surrounding black holes or galaxies. By embedding black holes within PFDM, researchers can study how dark matter affects spacetime curvature, orbital dynamics, and observable phenomena such as gravitational lensing. PFDM is also important for understanding the interactions between dark matter and baryonic matter.

Understanding the dynamics of charged and neutral test particles near black holes (BHs) is fundamental to relativistic astrophysics. Such investigations provide valuable insights into the extreme gravitational fields that characterize BHs. The motion of particles around compact objects serves as a testing ground for gravity theories. In particular, specific X-ray sources are thought to arise from accretion disks surrounding astrophysical BHs. Measurements of the inner edge radii of these disks can help constrain parameters in alternative and modified theories of gravity [182-191]. The capture of massive and massless particles by parameterized BHs has been extensively analyzed in [192-194]. Additionally, orbital and epicyclic frequencies in axially symmetric and stationary spacetimes have been explored in [195-197]. This motivates further exploration of particle motion around BHs, particularly within the framework of nonlinear electrodynamics combined with general relativistic solutions.

The detection of QPOs in the X-ray emissions from black holes and neutron stars has significantly advanced astrophysics by providing insights into the extreme gravitational environments surrounding these compact objects. The presence of quasiperiodic variations in brightness points to fundamental physical mechanisms, such

as oscillations within accretion discs or gravitational interactions, which can serve as tools for probing the properties of spacetime [31,56-58]. Twin-peak QPOs observed in certain systems have sparked debates about their origins and potential links to oscillatory modes within accretion discs. These findings underscore the importance of developing advanced theoretical models and obtaining more precise observational data. The initial discovery of QPOs through spectral analysis and X-ray binary flux measurements [59-61] has been the subject of extensive research. Numerous studies have explored the observational characteristics of QPOs and their theoretical underpinnings. Among the various proposed models, the most promising explanation ties QPOs to the dynamics of particles and the oscillations of their trajectories within the accretion disc. Previous investigations have focused on the synchronized motion of charged particles in the disc, shedding light on the mechanisms behind these phenomena [62-70,74,76,198]. This body of work highlights the complexity and significance of QPOs in understanding the physics of compact objects and their surrounding environments.

Recent advancements in BH physics have significantly improved our understanding of QPOs and the dynamics of test particles. In a 2024 study, Rayimbaev et al. explored the behavior of test particles and QPOs near Kiselev black holes, incorporating the effects of a cloud of strings. This work provided critical insights into the unique environments surrounding these black holes [77-79]. Further research has focused on the motion of test particles around regular Kiselev black holes, refining theoretical models related to these phenomena. Another investigation examined QPOs near hairy black holes within the framework of Horndeski gravity, offering new perspectives on how modified theories of gravity influence black hole oscillations [76]. This study highlighted the role of magnetic fields in analyzing regular nonminimal magnetic black holes as potential sources of QPOs, revealing how magnetic interactions affect their oscillatory behavior [80-83]. Additionally, research on charged particles and QPOs near magnetized Schwarzschild black holes has deepened our understanding

of how magnetism interacts with black hole dynamics [84]. Moreover, studies on QPOs from black holes influenced by noncommutative geometry have provided valuable insights into the impact of such geometries on black hole behavior [85]. These contributions collectively enhance our grasp of the complex dynamics governing black hole environments and their observable effects in astrophysical contexts [89-102].

The study of accretion disks around black holes is a cornerstone of modern astrophysics, providing critical insights into the behavior of matter and energy in extreme gravitational environments. Accretion disks are formed when matter, such as gas or dust, spirals inward toward a black hole, releasing vast amounts of energy primarily through electromagnetic radiation. This radiation spans a wide range of wavelengths, from radio waves to X-rays and γ rays, making accretion disks observable across the electromagnetic spectrum. This work uses the Novikov- Thorne model to explore the radiation properties of accretion disks around black holes. According to the Novikov-Thorne model, the accretion disk should be optically thick and geometrically thin in the vicinity of black holes. We study the flux of electromagnetic radiation, the temperature of the accretion disk, and differential luminosity.

3.2 Spacetime

Black holes in GR coupled to NED surrounded by PFDM exhibit unique spacetime properties. NED modifies the electromagnetic field, leading to regular black hole solutions without singularities. PFDM alters spacetime geometry, affecting the event horizon, thermodynamics, and stability. The motion of test particles near such black holes shows deviations in orbital dynamics due to the combined influence of NED and PFDM. These factors modify the disk structure, energy emission, and accretion rates in accretion disks.

3.2.1 Black hole solutions with the dark fluid equation of state

This section provides a concise overview of a black hole solution in GR that incorporates both NED and PFDM. The metric is constrained using a specific ansatz to derive a spherically symmetric black hole solution.

$$ds^2 = -f(r)dt^2 + \frac{1}{f(r)}dr^2 + r^2(d\theta^2 + \sin^2\,\theta d\phi^2) \tag{3.1}$$

Nonsingular extensions of black hole spacetimes have been widely considered in GR coupled to NED [145-152, 199, 200]. Here, we focus on GR coupled with NED in the presence of an external matter fields field called the PFDM field, with the action [201, 202]

$$\mathcal{L}_{\text{NED}} = Fe^{-\frac{q}{2M}(2q^2F)^{\frac{1}{4}}} \tag{3.2}$$

where q and $F = F_{\mu\nu}F^{\mu\nu}/4$ refer to the magnetic charge and the invariant of the non-linear electromagnetic field with $F_{\mu\nu} = \partial_\mu A_\nu - \partial_\nu A_\mu$. To obtain the BH solution, one can use $F = q^2/(2r^4)$ and the corresponding Lagrangian of a NED field in the following form [202]

$$\mathcal{L}_{\text{NED}} = \frac{q^2}{2r^4}e^{-\frac{q^2}{2Mr}}, \tag{3.3}$$

Since there is no matter Lagrangian, the energy-momentum tensor in Schwarzschild coordinates is due solely to $\mathcal{L}_{\text{NED}}$ as

$$G_{\mu\nu} = R_{\mu\nu} - \frac{1}{2}Rg_{\mu\nu} = T_{\mu\nu}^{(\text{NED})} + T_{\mu\nu}^{(\text{PFDM})} \tag{3.4}$$

The perfect fluid energy-momentum tensor is:

$$T_{\mu\nu}^{(\text{PFDM})} = (\rho + p)u_\mu u_\nu + pg_{\mu\nu}, \tag{3.5}$$

it has only the standard orthogonal basis [203, 204]

$$T_\mu^{\nu(\text{PFDM})} = \text{diag}\big(-\epsilon, p_r, p_\theta, p_\phi\big) \tag{3.6}$$

with

$$-\epsilon = p_r = \frac{\lambda}{r^3}, p_\theta = p_\phi = -\frac{\lambda}{2r^3} \tag{3.7}$$

The parameter λ is the energy density and pressure associated with PFDM. The energy-momentum tensor for the NED reads as,

$$T_{\mu\nu} = 2\left[\frac{\partial \mathcal{L}_{\text{NED}}}{\partial F} F_{\mu}{}^{\alpha} F_{\nu\alpha} - g_{\mu\nu}\mathcal{L}_{\text{NED}}\right] \tag{3.8}$$

The non-zero diagonal components of the tensor for the NED field are

$$T_0^0 = T_1^1 = -\frac{q^2}{r^4} e^{-\frac{q^2}{2Mr}} \tag{3.9}$$

To solve this Eq.(3.4), first we will find the component G_{tt} of the Einstein tensor as Now, we derive the field equation for the following ansatz,

$$G_0^0 = G_1^1 = -\frac{1}{r}\frac{df(r)}{dr} - \frac{f(r)}{r^2} + \frac{1}{r^2} \tag{3.10}$$

$$G_2^2 = G_3^3 = -\frac{1}{2}\frac{d^2 f(r)}{dr^2} - \frac{1}{r}\frac{df(r)}{dr} \tag{3.11}$$

For a static and spherically symmetric spacetime with line element Eq. (3.1) and NED source given by a magnetic charge q in which $F_{\mu\nu} = \left(\delta_\mu^\theta \delta_\nu^\phi - \delta_\nu^\theta \delta_\mu^\phi\right) q \sin\,\theta$.

The metric function $f(r)$ satisfies the following differential equation, which is derived from Eq. (3.4) while incorporating Eqs. (3.6), (3.9), and (3.10):

$$\frac{1}{r}\frac{df(r)}{dr} + \frac{f(r)}{r^2} - \frac{1}{r^2} = \frac{q^2}{r^4} e^{-\frac{q^2}{2Mr}} + \frac{\lambda}{r^3} \tag{3.12}$$

If we solve Eqs. (3.12)

$$f(r) = \frac{-2Me^{-\frac{q^2}{2Mr}} + \lambda \ln\, r + r}{r} + \frac{c_1}{r} \tag{3.13}$$

Considering that the argument of the logarithmic term must be dimensionless, we set the constant as $c_1 = -\lambda \ln\, |\lambda|$. This leads to the following expression for the metric function:

$$f(r) = 1 - \frac{2Me^{-\frac{q^2}{2Mr}}}{r} + \frac{\lambda}{r} \ln\, \frac{r}{|\lambda|} \tag{3.14}$$

Next, we examine the horizon properties of the derived black hole solution using graphical analysis.

The parameter λ has little effect on the change in the event's horizon, while high values of the parameter q lead to an internal horizon (Cauchy). Moreover, in the lower limit of values of q, the Cauchy horizon disappears.

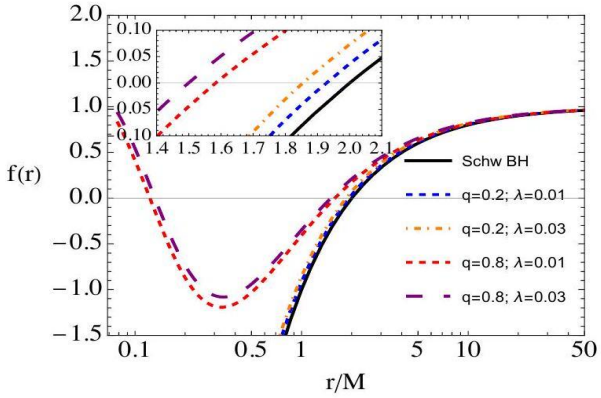


Figure 3.1: Radial dependence of lapse function $f(r)$ for varying values of q and λ.

The radial profiles of the metric function $f(r)$ for different values of the parameters λ and q are shown in Fig. 3.1.

To study the effect of the EoS parameters on the geometry around the BH , we consider the event horizon, which can be studied using the solution of the equation $f(r) = 0$.

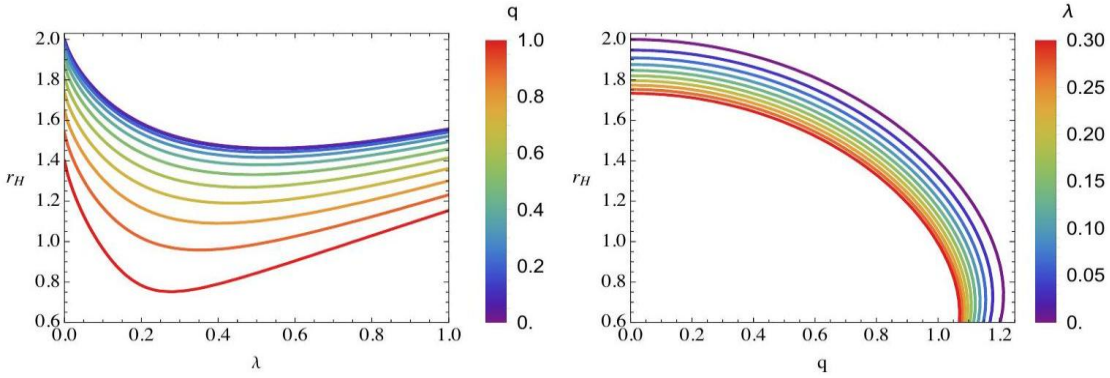


Figure 3.2: The Event horizon radius for q and λ.

The dependence of the radius of the event horizon on the parameter q for different values of λ is shown in Fig. 3.2. All quantities were normalized to the black hole mass in plotting the figure, with $M = 1$ assumed for simplicity. As can be seen from the figure, the radius increases with increasing values of λ. Conversely, as the

parameter q increases, the event horizon decreases, indicating that this parameter has an antigravitational effect.

3.2.2 The scalar invariants.

To explore the properties of spacetime, we may start by studying the scalar invariants of geometry around a compact gravitating object. Here, we analyze the Ricci scalar, square of the Ricci tensor, and Kretschmann scalar of the spacetime metric (3.1) given with the lapse function given by Eq. (3.14). We calculate and analyze these quantities by observing their graphical behavior.

Ricci scalar

The Ricci scalar, also referred to as scalar curvature, is defined as $R = g^{\mu\nu}R_{\mu\nu}$, where $R_{\mu\nu}$ represents the Ricci tensor. The sign of the Ricci scalar indicates the curvature nature of spacetime: a positive value corresponds to a sunken or converging curvature. In contrast, a negative value represents a convex or diverging curvature. Through algebraic manipulations, the Ricci scalar can be expressed in the following form:

$$R = \frac{q^4}{2Mr^5} e^{-\frac{q^2}{2Mr}} - \frac{\lambda}{r^3}, \tag{3.15}$$

at $q \to 0, R = -\frac{\lambda}{r^3}$.

Square of Ricci tensor

The second scalar invariant, the Ricci tensor's square, characterizes the squared contribution of the energy-momentum tensor in spacetime. It is mathematically expressed as $\mathcal{R} = R_{\mu\nu}R^{\mu\nu} \equiv \frac{1}{8\pi G} T_{\mu\nu}T^{\mu\nu}$, where $R_{\mu\nu}$ represents the Ricci tensor and $T_{\mu\nu}$ denotes the energy-momentum tensor. For the spacetime surrounding black holes with lapse functions given by Eq. (3.14), this scalar invariant simplifies to the following form:

$$\mathcal{R}=\frac{1}{8r^{10}}\left[\frac{q^4}{M^2}(32M^2r^2-8Mq^2r+q^4)e^{-\frac{q^2}{Mr}}\right.$$
$$\left.+\frac{4\lambda}{M}q^2r^2(q^2-12Mr)e^{-\frac{q^2}{2Mr}}+20\lambda^2r^4\right] \quad (3.16)$$

Therefore,

$$q=0 \implies \mathcal{R}=\frac{5\lambda^2}{2r^6} \quad (3.17)$$

$$\lambda=0 \implies \mathcal{R}=\frac{q^4e^{-\frac{q^2}{Mr}}}{8r^{10}}\left(32r^2-8q^2\frac{r}{M}+\frac{q^4}{M^2}\right) \quad (3.17)$$

Kretschmann scalar

Now, we consider the Kretschmann scalar, defined as $\mathcal{K}=R_{\mu\nu\sigma\rho}R^{\mu\nu\sigma\rho}$. Physically, the square root of the Kretschmann scalar can be interpreted as an effective gravitational energy density, expressed as $\sqrt{\mathcal{K}}\sim\rho_M$. For the given spacetime metric in Eq. (3.14), the Kretschmann scalar takes the following form:

$$\mathcal{K}=\frac{e^{-\frac{q^2}{Mr}}}{4M^2r^{10}}[q^8-16Mq^6r+96M^2q^4r^2-192M^3q^2r^3$$
$$+192M^4r^4-4\lambda Mr^2e^{\frac{q^2}{2Mr}}(32Mq^2r-40M^2r^2-3q^4$$
$$+2\ln\frac{r}{|\lambda|}(24M^2r^2-12Mq^2r+q^4)\Big)$$
$$+4\lambda^2M^2r^4e^{\frac{q^2}{Mr}}\left(12\ln^2\frac{r}{|\lambda|}-20\ln\frac{r}{|\lambda|}+13\right)\Big]. \quad (3.18)$$

From that, we have

$$q\to 0,\lambda\to 0 \Longrightarrow \mathcal{K}=\frac{48M^2}{r^6} \quad (3.19)$$

Fig. 3.3 demonstrates the radial behavior of scalar invariants, including the Ricci scalar, the square of the Ricci tensor, and the Kretschmann scalar, for different values of the magnetic charge q. These invariants decrease rapidly as r grows and converge to an asymptotic value, indicating a Ricci flat condition. A higher magnetic charge q value leads to a slight rise in the scalar invariants.

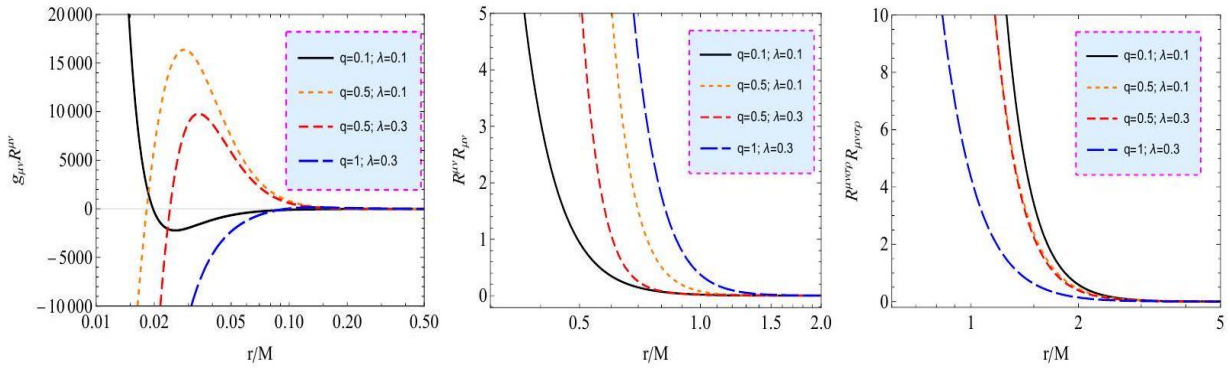


Figure 3.3: Radial profiles of scalar invariants, varying values of q and λ. From left to right, we show the Ricci scalar, the square of the Ricci tensor, and the Kretschmann scalar, respectively.

3.3 Circular motion of test particles

Test particle motion describes the movement of particles that do not carry a net electric charge, making them unaffected by electric fields. However, other forces, such as gravitational, magnetic, or particle interactions, can still influence these particles. Analyzing the motion of neutral particles is essential in several scientific disciplines, including nuclear physics, astrophysics, and materials science. Investigating how these particles behave in external fields and interact with their surroundings offers valuable insights into the properties of matter under various conditions, helping scientists better understand fundamental processes in the universe.

3.3.1 Equations of motion

The Hamilton-Jacobi equation for a neutral test particle of mass m is

$$g^{\mu\nu}\frac{\partial S}{\partial x^{\mu}}\frac{\partial S}{\partial x^{\nu}} + m^2 = 0 \tag{3.20}$$

We adopt the separable ansatz for the action,

$$S = -Et + L\phi + S_r(r) + S_\theta(\theta) \tag{3.21}$$

where E and L are the conserved energy and angular momentum, respectively.

Substituting this ansatz into the Hamilton-Jacobi equation, we obtain

$$-\frac{E^2}{g_{tt}} + \frac{1}{g_{rr}}\left(\frac{dS_r}{dr}\right)^2 + \frac{1}{g_{\theta\theta}}\left(\frac{dS_\theta}{d\theta}\right)^2 + \frac{L^2}{g_{\phi\phi}} + m^2 = 0 \tag{3.22}$$

Since the metric is separable, we introduce a separation constant K (the Carter constant) so that the radial and angular parts separate:

$$\frac{1}{g_{rr}}\left(\frac{dS_r}{dr}\right)^2 - \frac{E^2}{g_{tt}} + m^2 = K \tag{3.23}$$

and

$$\frac{1}{g_{\theta\theta}}\left(\frac{dS_\theta}{d\theta}\right)^2 + \frac{L^2}{g_{\phi\phi}} = -K \tag{3.24}$$

The generalized momenta are given by

$$p_t = \frac{\partial S}{\partial t} = -E \tag{3.25}$$

$$p_\phi = \frac{\partial S}{\partial \phi} = L \tag{3.26}$$

$$p_r = \frac{dS_r}{dr} \tag{3.27}$$

$$p_\theta = \frac{dS_\theta}{d\theta} \tag{3.28}$$

The four velocities can be derived using the relation

$$\dot{x}^\mu = \frac{1}{m} g^{\mu\nu} p_\nu \tag{3.29}$$

Finally, geodesic motion for neutral test particles can be found using Eq. (3.25)(3.28), and immediately, we have the following equations for radial and vertical motions,

$$\dot{t} = -\frac{\mathcal{E}}{g_{tt}} \tag{3.30}$$

$$\dot{r}^2 = \mathcal{E}^2 + g_{tt}\left(1 + \frac{K}{r^2}\right) \tag{3.31}$$

$$\dot{\theta}^2 = \frac{1}{g_{\theta\theta}^2}\left(K - \frac{\mathcal{L}^2}{\sin^2\theta}\right) \tag{3.32}$$

$$\dot{\phi} = \frac{\mathcal{L}}{g_{\phi\phi}} \tag{3.33}$$

where $\mathcal{L} = L/m$ and $\mathcal{E} = E/m$. Note that the Carter constant K is associated with θ -motion, and its square root has units of angular momentum and corresponds to the total angular momentum of a test particle.

Restricting the motion of the particle to the constant plane ($\theta = \text{const}$ and $\dot{\theta} = 0$), the Carter constant takes the form $K = \mathcal{L}^2$, and the equation of the radial motion can be expressed as

$$\dot{r}^2 = \mathcal{E}^2 - V_{\text{eff}} \tag{3.34}$$

where the effective potential of the motion of neutral particles is defined as

$$V_{\text{eff}}(r;\theta) = f(r)\left(1 + \frac{\mathcal{L}^2}{r^2 \sin^2\theta}\right) \tag{3.35}$$

The radial profile of the effective potential for different magnetic charge and PFDM parameters values, q and λ, is shown in Fig. 3.4, and a comparison is made with the Schwarzschild BH case. It can be seen from the figure that the maximum value of V_{eff} has increased compared to the Schwarzschild case (black curve, at $\lambda = q = 0$ case) due to the orbits corresponding to the maximum shifts of q and λ and towards the central BH , making it harder for particles to remain in stable orbits. This can influence black hole accretion dynamics and observational signatures.

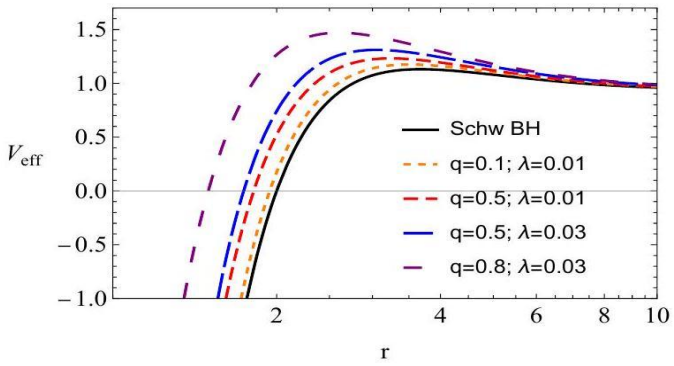


Figure 3.4: The radial dependence of the effective potential for the circular motion of test particles around the BH for different values of q and λ parameters. The specific angular momentum is fixed as $\mathcal{L} = \sqrt{20}M, M = 1$.

3.3.2 The circular orbits

To study the circular motion of the particles, we use the following conditions:

$$\dot{r}^2 = 0, \text{ or } V_{\text{eff}} = \mathcal{E}^2, \text{ and } V'_{\text{eff}} = 0. \tag{3.36}$$

Using the solution of Eq. (3.36), we found the following expressions for the expressions of angular momentum and energy of particles corresponding to circular orbits:

$$\mathcal{L}^2 = \frac{r^2\left(\lambda r e^{\frac{q^2}{2Mr}}\left(1-\ln\frac{r}{|\lambda|}\right)+2Mr-q^2\right)}{re^{\frac{q^2}{2Mr}}\left(3\lambda\ln\frac{r}{|\lambda|}-\lambda+2r\right)-6Mr+q^2},$$

$$\mathcal{E}^2 = \frac{2\left(r+\lambda\ln\frac{r}{|\lambda|}-2Me^{-\frac{q^2}{2Mr}}\right)^2}{r\left(2r-\lambda\left(1-3\ln\frac{r}{|\lambda|}\right)\right)+e^{-\frac{q^2}{2Mr}}(q^2-6Mr)}. \qquad (3.37)$$

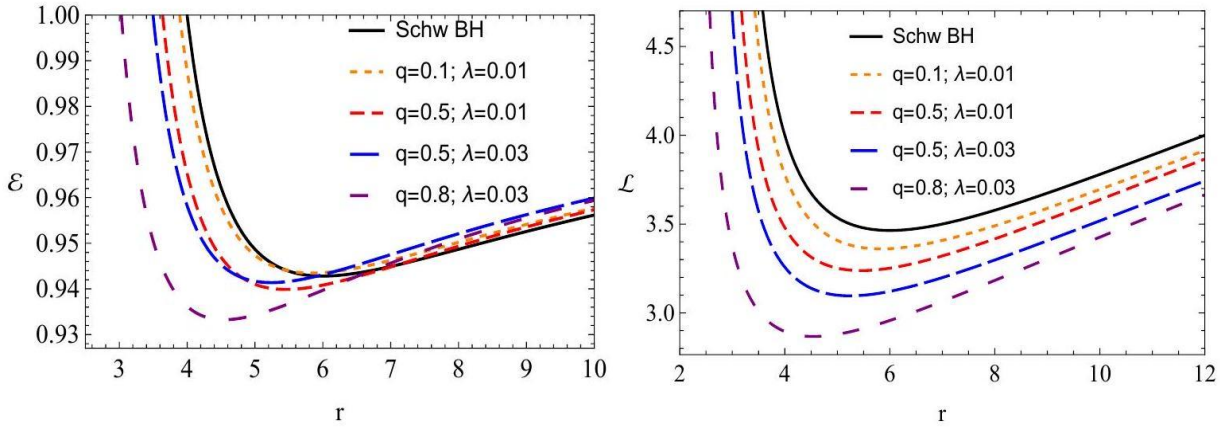


Figure 3.5: The profiles of $\mathcal{E}$ vary with q and λ (top panel). The bottom panel shows the plot of $\mathcal{L}$ for λ and q

Fig. 3.5 shows the radial profiles of specific energy $\mathcal{E}$ and angular momentum $\mathcal{L}$ corresponding to circular orbits. The top panel shows that increasing the magnetic charge q lowers the required energy for stable orbits, shifting the innermost stable circular orbit (ISCO) inward and allowing particles to be more tightly bound. This suggests that a magnetic charge enhances energy extraction efficiency from accretion disks. The bottom panel reveals that a higher q also decreases the angular momentum needed for circular motion, further supporting the idea that magnetically charged black holes influence disk dynamics significantly. In contrast, the PFDM parameter λ has a weaker effect, mainly noticeable at more considerable distances, where it slightly

increases both $\mathcal{E}$ and $\mathcal{L}$, indicating a reduction in gravitational attraction. These findings suggest that while magnetic charge moderates inner accretion disk properties, PFDM influences the outer disk structure. The results have important implications for observational astrophysics, particularly in studying quasi-periodic oscillations (QPOs) and X-ray emissions from accreting black holes, where deviations from standard Schwarzschild behavior may provide signatures of new physics.

3.3.3 Stable circular orbits

Understanding the stability of circular orbits around black holes is fundamental to astrophysical processes such as accretion disk radiation and QPOs in X-ray binaries. In GR, stable orbits exist only above the innermost stable circular orbit (ISCO), beyond which perturbations cause test particles to spiral into the black hole. However, additional fields, such as NED and PFDM, can modify the gravitational potential of the central black hole, altering the ISCO radius and the stability conditions of circular motion. These modifications have direct observational consequences as they affect the efficiency of energy extraction from the disk and influence the emitted radiation spectrum. In this section, we investigate the stability conditions of circular orbits around a magnetically charged black hole in the presence of PFDM, analyzing how the parameters q (magnetic charge) and λ (PFDM parameter) influence the ISCO structure and orbital dynamics.

$$\begin{aligned} &2\lambda(24M^2r^2 - 6Mq^2r - q^4)\ln\frac{r}{|\lambda|} \\ &-\lambda Mr^2 e^{\frac{q^2}{2Mr}}\left(4\ln\frac{r}{|\lambda|}\left(3\lambda\ln\frac{r}{|\lambda|} - 4\lambda + r\right) + 8\lambda\right) \\ &+4Me^{-\frac{q^2}{2Mr}}(6Mq^2r - 12M^2r^2 + q^4) \\ &+2r(4M^2r(r-4\lambda) + 2Mq^2(4\lambda + r) - q^4) = 0 \end{aligned} \tag{3.38}$$

The equation describes the stability condition for circular orbits in compact objects that gravitate in spacetime $\partial_{rr}V_{\text{eff}} \geq 0$. The innermost stable circular orbits satisfy the condition $\partial_{rr}V_{\text{eff}} = 0$. This condition is often applied with the circularity condition in Eq. (3.36). The equation $\partial_{rr}V_{\text{eff}} = 0$ leads to the

following equation, the radius of the ISCO of the test particles can be calculated numerically by solving Eq. (3.38). The dependence of the ISCO radius on the parameters λ and q is shown in Fig. 3.6. The ISCO defines the smallest radius at which test particles can maintain stable circular motion before plunging into the black hole. This parameter is critical in black hole astrophysics as it determines the inner edge of the accretion disk, influences emitted radiation, and plays a key role in quasi-periodic oscillations (QPOs) observed in X-ray binaries. The top panel shows r_{ISCO} vs. q for different values of λ. As q increases, r_{ISCO} decreases, meaning that a stronger magnetic charge allows stable orbits closer to the black hole. For small values of λ, the ISCO radius remains nearly constant for low q but decreases significantly at higher q. For larger λ, the ISCO radius is consistently larger, showing that PFDM counteracts the inward pull caused by magnetic charge. r_{ISCO} vs. λ for different values of q is shown. Increasing λ initially reduces the ISCO radius, but at higher values of the PFDM parameter, the ISCO radius increases again. The minimum r_{ISCO} occurs at intermediate λ, suggesting that PFDM initially enhances stability but weakens gravitational attraction at higher values. For higher magnetic charge q, the ISCO radius remains lower than the Schwarzschild case, reinforcing that q dominates over λ in determining inner disk structure.

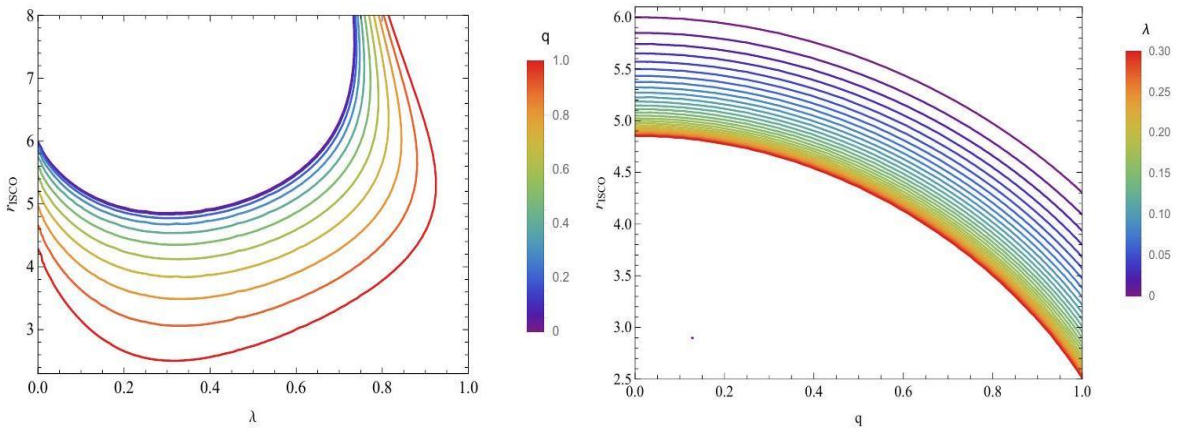


Figure 3.6: Dependence of r_{ISCO} on λ and q for different values of q and λ.

A higher q reduces the ISCO radius, meaning that charged black holes allow test particles to orbit closer before becoming unstable. This has implications for compact X-ray binaries, where tighter accretion disks could lead to stronger gravitational redshifts and higher accretion efficiency.

The behavior of ISCO radius with λ suggests that PFDM can initially strengthen gravity but weaken it at large widths, influencing the structure of dark matter halos around black holes. Since the ISCO location determines accretion efficiency and QPO frequencies, modifications by q and λ could provide observational signatures of non-Schwarzschild black holes in future X-ray and gravitational wave observations.

3.4 Radiation properties of the accretion disk of black hole

In this section, we study the radiative properties of the accretion disk of the magnetically charged BH in PFDM. We consider the Novikov-Thorne model for the accretion disk around the astrophysical compact objects. According to this model, the accretion disk should be optically thick and geometrically thin near the magnetically charged BH in PFDM . We explore the important quantities of the accretion disk using this model. The first is the flux of the electromagnetic radiation produced by the accretion disk of the magnetically charged BH in PFDM . Here, we note that the accretion disk is composed of gas and dust moving in the stable orbits of a black hole or neutron star. Gas and dust can lose energy and angular momentum due to the influence of the surrounding geometry as they begin to orbit the compact object. Consequently, the gas and dust orbits shift toward the inner edge of the accretion disk, eventually causing them to descend toward the compact object. This process leads to accretion disk radiation, where gas and dust heat up and release energy as radiation. We expect that the parameters of the magnetically charged BH can affect the radiation of the accretion disk. It is worth noting that the radiation from the accretion disk is considered a powerful tool for investigating key aspects of the disk and may have significant implications for observational studies.

$$\mathcal{F}(r) = -\frac{\dot{M}_0}{4\pi\sqrt{g}}\frac{\Omega_{,r}}{(\mathcal{E}-\Omega\mathcal{L})^2}\int_{r_{ISCO}}^{r}(\mathcal{E}-\Omega\mathcal{L})\mathcal{L}_{,r}dr \tag{3.39}$$

where g refers to the determinant of the three-dimensional subspace $g = \sqrt{-g_{tt}g_{rr}g_{\phi\phi}}$ with (t, r, ϕ) coordinates. The flux $\mathcal{F}(r)$ is defined as a function of the $\dot{M}_0$, which refers to the accretion rate of the mass of the disk and is unknown. However, we can set $\dot{M}_0 = 1$ for simplicity. One can derive the flux of the electromagnetic radiation using Eq. 3.37. Note that Ω is the orbital angular velocity of the test particles, and we considered this in detail in the next section.

In the numerical evaluation of the Novikov–Thorne flux, temperature, and differential luminosity, all quantities are first calculated in geometrized units, where $G = c = 1$. The radial coordinate is measured in units of the gravitational radius $r_g = GM_{\rm BH}/c^2$. Therefore, to express the results in physical cgs units, one has to specify the black-hole mass $M_{\rm BH}$ and the mass accretion rate $\dot{M}_0$.

In the present analysis, $\dot{M}_0$ is treated as a fixed normalization parameter. Hence, the plotted profiles of $F(r)$, $T(r)$, and $dL_\infty/d\ln r$ should be understood with respect to the adopted values of $M_{\rm BH}$ and $\dot{M}_0$. The absolute numerical values in units of erg cm^{-2} s^{-1}, K, and erg s^{-1} depend on this physical normalization, whereas the relative dependence on the magnetic charge q and the PFDM parameter λ is not affected by the choice of normalization.

The flux scale is controlled by both $M_{\rm BH}$ and $\dot{M}_0$: increasing $\dot{M}_0$ increases the flux normalization, while increasing $M_{\rm BH}$ decreases the flux scale. The disk temperature is obtained from the Stefan–Boltzmann relation, $T(r) \propto F(r)^{1/4}$, and therefore it depends on the same normalization. The differential luminosity is obtained from the local disk flux integrated over the emitting disk surface, with the corresponding relativistic energy factor included. For this reason, the luminosity should be expressed in erg s^{-1}, not simply in erg.

It should also be clarified that the determinant factor $\sqrt{-g}$ in Eq. (3.39) denotes the metric determinant contribution entering the Novikov–Thorne thin-disk flux formula on the equatorial disk surface. It is evaluated from the (t, r, ϕ) sector of the spacetime metric at $\theta = \pi/2$, rather than being introduced as an independent physical assumption. This determinant factor fixes the geometrical normalization of the disk surface element and removes the ambiguity in the definition of the flux normalization.

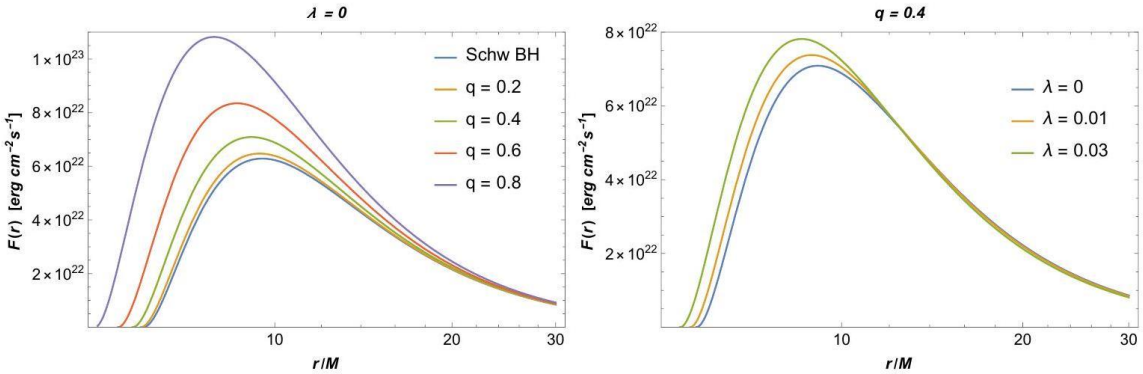


Figure 3.7: The radial profile of the flux of electromagnetic radiation for different values of the magnetic charge q (left panel) and λ parameter (right panel). The flux is shown using the adopted physical normalization of M_{BH} and $\dot{M}_0$. Therefore, the absolute scale depends on these choices, while the relative dependence on q and λ remains unchanged.

It is complicated to derive the analytical expression for the flux of electromagnetic radiation, thus we explore it numerically in Fig. 3.7. One can see from the left panel of this figure that the flux values increase with increasing magnetic charge q for $\lambda = 0$. The right panel of this figure represents the radial dependence of the flux of electromagnetic radiation for different values of the λ parameter. It can be seen from this panel that there is an increase under the influence of the λ parameter. We then turn to another important quantity of electromagnetic radiation: the disk's temperature. One can write the flux of the black body radiation as $\mathcal{F}(r) = \sigma T^4$, where σ is Stefan-Boltzmann's constant.

One can plot the radial dependence of the disk temperature and energy for different values of the magnetic charge q and λ parameter in Fig. 3.8. One can see from this figure that the values of the temperature and energy increase with the increasing magnetic charge q and λ parameter.

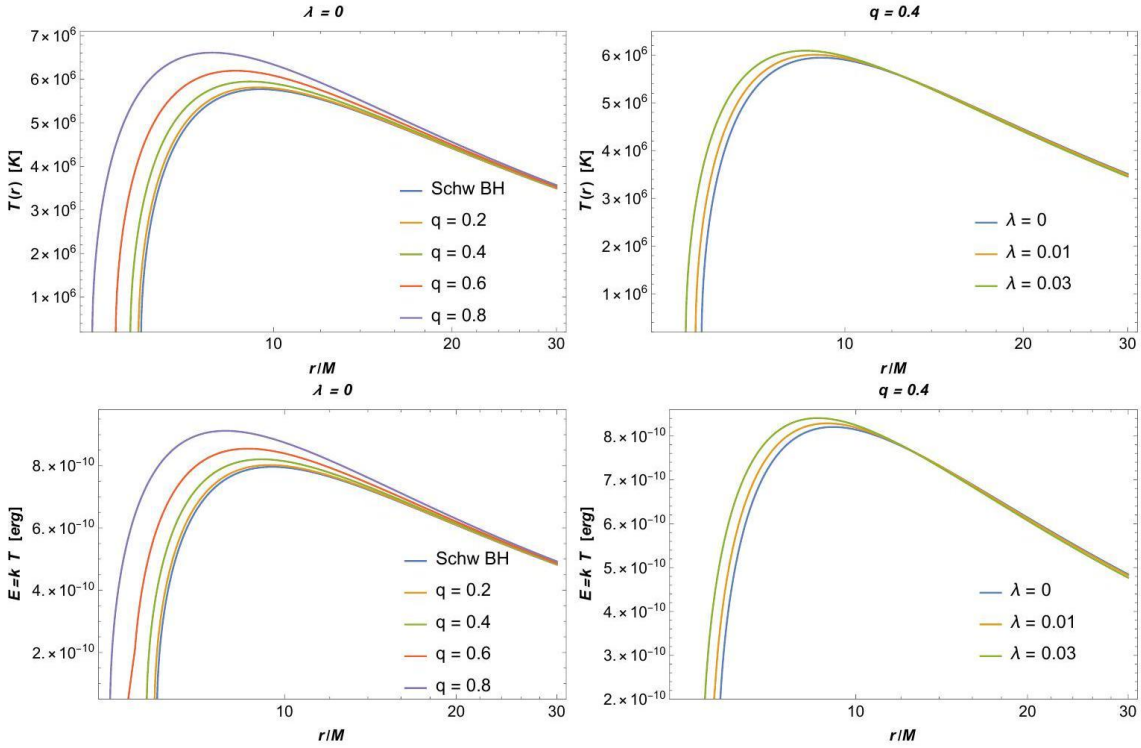


Figure 3.8: The radial profile of the temperature (top panel) and energy (bottom panel) for different values of magnetic charge q and λ parameter. The temperature is obtained from the disk flux through the Stefan–Boltzmann relation, using the same mass and accretion-rate normalization as in the flux calculation.

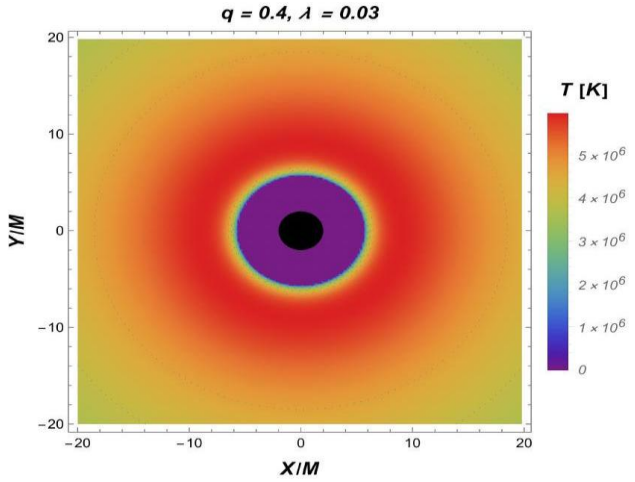


Figure 3.9: The plot depicts the density plot of the accretion disk temperature at the equatorial $X-Y$ plane of the magnetically charged black hole. Here, X and Y are the Cartesian coordinates.

It is worth noting that the impact of these parameters is the same for both temperature and energy. To provide more information, one can plot the temperature by "color map" in Fig. 3.9. From Fig. 3.9, it is evident that the dark region is located within the inner edge of the accretion disk, while the red areas represent regions where the disk's temperature reaches its peak value. Moreover, we consider the differential luminosity, which is defined by [205]

$$\frac{d\mathcal{L}_{\infty}}{d\ln\, r} = 4\pi r\sqrt{g}E\mathcal{F}(r) \tag{3.40}$$

It is worth noting that we have used numerical methods to explore the radial dependence of the differential luminosity. The radial profile of the differential luminosity is demonstrated in Fig. 3.10. One can see from this figure that there is an increase with the increase of the magnetic charge q. The values of the differential luminosity also increase slightly under the influence of the λ parameter.

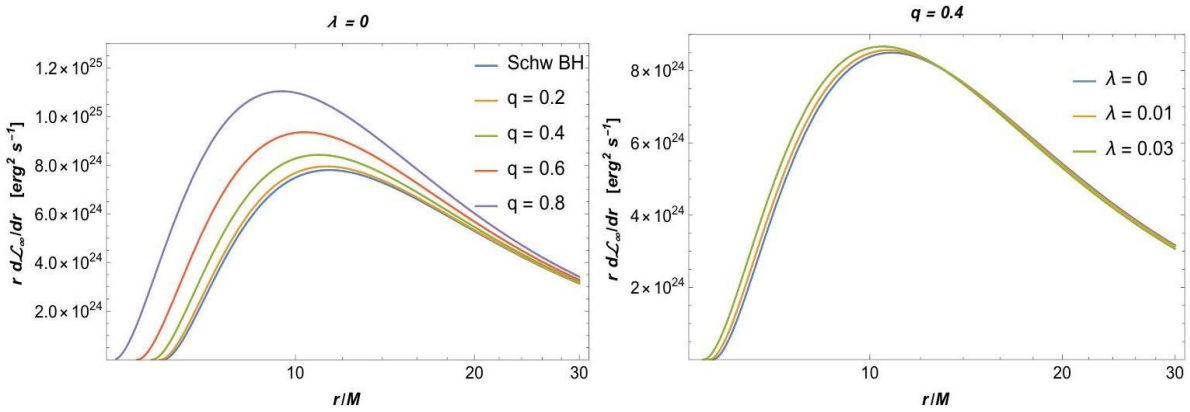


Figure 3.10: The radial profile of the differential luminosity of the accretion disk around the magnetically charged black hole for different values of the magnetic charge (left panel) and λ parameter (right panel). The differential luminosity is plotted in erg s^{-1}, using the same physical normalization adopted for the flux and temperature profiles.

The presence of magnetic charge (NED effects) and PFDM significantly alters the radiation properties of the accretion disk. The flux of electromagnetic radiation, disk temperature, and differential luminosity all increase with the magnetic charge q, indicating that stronger magnetic fields enhance energy release from the disk. This suggests that black holes with substantial NED charge could display brighter and hotter accretion disks than their Schwarzschild counterparts.

The PFDM parameter has a subtler effect, mainly modifying the flux and temperature at larger disk radii. This implies that PFDM influences longwavelength emissions (e.g., in infrared or radio bands), which could be detectable in active galactic nuclei (AGN) and X-ray binaries.

From an observational standpoint, the combination of increased flux, higher temperatures, and modified QPO frequencies offers a potential test for detecting NED black holes in X-ray spectra. Future Athena, XRISM, or NICER observations could constrain q and heta by analyzing deviations from standard accretion disk models. In addition, gravitational wave signatures from mergers involving magnetically charged black holes could reveal distinct features in the inspiral and ringdown phases, providing another avenue for testing these effects.

3.5 Fundamental frequencies

This section discusses the fundamental frequencies of test particles around our modified Schwarzschild BH of metric (3.1). The plan is to study the possible values of the upper and lower frequencies by the following models for twin peak HF QPOs described by the fundamental frequencies of test particles around compact gravitating objects $\left(\nu_{r,\theta,\phi} = c^3/(2\pi GM)\Omega_{r,\theta,\phi}\right.$, the speed of light in vacuum and the gravitational constant are $c = 3 \cdot 10^8$ m/sec and $G = 6.67 \cdot 10^{-11}$ m^3/(kg$^2 \cdot$ sec), respectively.) The equatorial circular orbits of a test particle are characterized by three fundamental frequencies:

1. Orbital frequency (or Keplerian frequency) ν_ϕ, which is the inverse of the orbital period.

2. Radial epicyclic frequency ν_r is the frequency of radial oscillations around the stable orbits.

3. The vertical epicyclic frequency ν_θ is the frequency of vertical oscillations around the stable orbits.

These three frequencies are determined solely by the space-time metric and the orbital radius. Although they are primarily defined as the characteristic frequencies of a free particle's orbital motion, they are directly linked to the oscillation modes of the fluid within an accretion flow.

To study the Keplerian frequency of a test particle, one uses the geodesic equation,

$$\ddot{x}^\alpha + \Gamma^\alpha_{\mu\nu}\dot{x}^\mu\dot{x}^\nu = 0, \tag{3.41}$$

here, $\Gamma^\alpha_{\mu\nu}$ are the Christoffel symbols and $\dot{x} = \dot{t}(1,0,0,\Omega)$, the equation of motion, the test particles get the form

$$\partial_r g_{tt} + \Omega^2 \partial_r g_{\phi\phi} = 0 \tag{3.42}$$

and the solution of the above equation for the Keplerian frequency, Ω_K, can be expressed as

$$\Omega_K^2 = \frac{M(2Mr - q^2)}{2e^{\frac{q^2}{2Mr}}r^4} + \frac{\lambda}{2r^3}\left(1 - \ln\frac{r}{|\lambda|}\right) \tag{3.43}$$

The radial dependence of the angular momentum of particles in Kepler orbits is shown in Figure 3.11 by varying the parameters q and λ. Compared with the Schwarzschild case, it can be observed that the Kepler frequency decreases when the parameter λ is present. In contrast, the parameter q leads to a sharp decrease. The effect of the PFDM parameter on the frequency is insignificant at large distances.

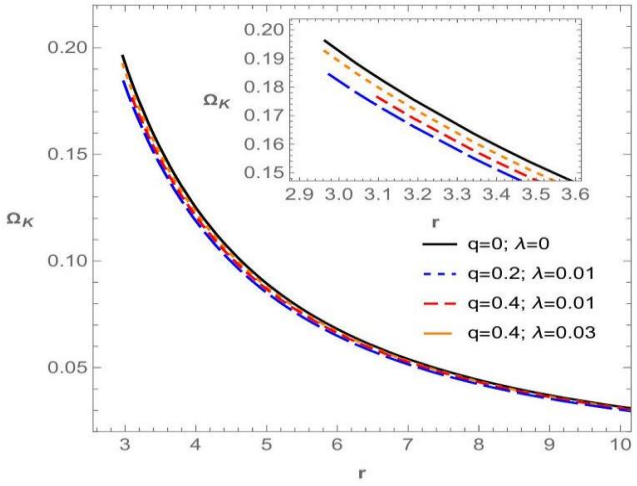


Figure 3.11: The figure shows the radial dependence Ω_K

The test particles moving in the equatorial plane around BHs in stable orbits oscillate along radial and vertical axes because of the small displacement from their stable orbits as $r_0 + \delta r$ and $\pi/2 + \delta\theta$. The radial and vertical frequencies can be calculated by the following harmonic oscillator equations as [206,207]:

$$\frac{d^2\delta r}{dt^2} + \Omega_r^2 \delta r = 0, \frac{d^2\delta\theta}{dt^2} + \Omega_\theta^2 \delta\theta = 0, \tag{3.44}$$

where

$$\Omega_i^2 = -\frac{1}{2g_{ii}(u^t)^2}\partial_i^2 V_{\text{eff}}(r,\theta)\Big|_{\theta=\pi/2}, i = r, \theta \tag{3.45}$$

are the radial and vertical angular frequencies, respectively. Some algebra leads to

$$\frac{\Omega_r^2}{\Omega_K^2} = \frac{2\lambda \ln\frac{r}{|\lambda|}}{r} + \frac{2\left(q^2 - r\lambda e^{\frac{q^2}{2Mr}} - 2rM\right)}{e^{\frac{q^2}{2Mr}} r^2} \tag{3.46}$$

$$+ \frac{\lambda \ln\frac{r}{|\lambda|} - 2Me^{-\frac{q^2}{2Mr}} + r}{2Mr^2\left(\lambda r e^{\frac{q^2}{2Mr}} \ln\frac{r}{|\lambda|} + \lambda r e^{\frac{q^2}{2Mr}} - 2Mr + q^2\right)} \tag{3.46}$$

$$\times\left(2\lambda M r^2 e^{\frac{q^2}{2Mr}} \ln\frac{r}{|\lambda|} - 4M^2r^2 - 2Mq^2r + q^4\right) \tag{3.46}$$

If we calculate the PFDM parameter $\lambda \to 0$, we have the following equality:

$$\frac{\Omega_r^2}{\Omega_K^2} = \frac{1}{2Mr^2(q^2-2Mr)}\left[r(q^4-4M^2r^2-2Mq^2r)\right.$$
$$\left.+2Me^{-\frac{q^2}{2Mr}}(q^4+12M^2r^2-6Mq^2r)\right] \quad (3.47)$$

If we calculate the NED parameter $q \to 0$, we have the following equality:

$$\frac{\Omega_r^2}{\Omega_K^2} = \frac{1}{r\left(\lambda-\lambda\ln\frac{r}{|\lambda|}+2M\right)}\left[\lambda(4\lambda+12M-r)\ln\frac{r}{|\lambda|}\right.$$
$$\left.-3\left(\lambda\ln\frac{r}{|\lambda|}\right)^2-2(\lambda^2+6M^2+4\lambda M-Mr)\right] \quad (3.48)$$

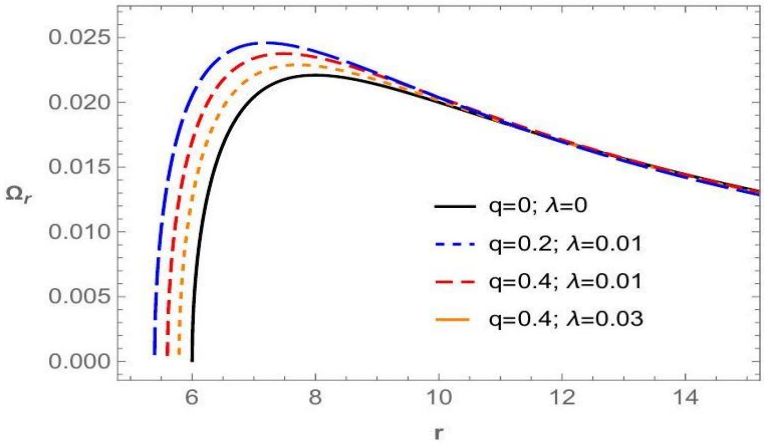


Figure 3.12: The figure shows the radial dependence Ω_r

Figure. 3.12 illustrates the radial dependence of the radial epicyclic frequency Ω_r for different values of the magnetic charge q and the PFDM parameter λ.

The radial epicyclic frequency Ω_r characterizes the oscillatory motion of test particles around stable circular orbits, playing a crucial role in the study of quasi-periodic oscillations (QPOs) observed in black hole accretion disks.

The figure shows that increasing the magnetic charge q significantly increases Ω_r, indicating stronger radial oscillations. This suggests that magnetically charged black holes influence disk dynamics more prominently than their Schwarzschild counterparts. The PFDM parameter λ, on the other hand, causes a slight decrease in Ω_r, implying that dark matter effects suppress radial oscillations, making orbits more stable.

For large radial distances, the effects of q and λ diminish, and Ω_r approaches the Schwarzschild case. These results have observational implications, as variations in epicyclic frequencies can modify QPO signals detected in X-ray binaries and active galactic nuclei, potentially offering a means to constrain black hole parameters through astrophysical observations.

3.6 Astrophysical Applications to Theoretically Calculated Quasi-Periodic Oscillations

This section explores possible frequencies of twin-peak QPOs around black holes in GR coupled to NED and surrounded by PFDM using various QPO models. Special attention is paid to examining the relationship between the observed frequencies and the motion of neutral particles orbiting such black holes. Additionally, we investigate the dependence of the mass of the black hole on the parameters q and λ using observational frequency data from QPOs. We also consider black holes at the center of microquasars GRS $1915+105$ and XTE 1550-564, assuming PFDM influences their surroundings within the framework of GR coupled to NED.

Detectors aboard X-ray missions can measure the arrival time of X-ray photons with micro- and nanosecond accuracy. QPOs appear as narrow features in a source's X-ray power density spectrum, typically found via Fourier transformation of the photon count rate. In black hole binaries, QPOs are categorized into low-frequency QPOs (LFQPOs) and high-frequency QPOs (HFQPOs). LFQPOs typically range from 0.1 - 30 Hz and exhibit variability on short timescales (~ 1 min) or remain relatively stable, classified into type-A, type-B, and type-C. For instance, type-A QPOs usually manifest in the high soft state after the intermediate state. Type-B QPOs define the soft intermediate state, while type-C QPOs are primarily observed when the source is in the bright end of the hard state or the hard intermediate state. HFQPOs, on the other hand, have frequencies in the range of 40 ~ 450 Hz. In four systems, pairs of HFQPOs have been detected, often appearing at frequency ratios of $3:2$. These two QPOs are

commonly referred to as the upper and lower HFQPOs. Table 3.1 presents the sources where such HFQPO pairs have been identified.

Table 3.1: Frequencies of twin peak QPOs in microquasars and Galactic centre

Source [197, 208-212]	$\nu_{\mathrm{U}}[\mathrm{Hz}]$	$\Delta\nu_{\mathrm{U}}[\mathrm{Hz}]$	$\nu_{\mathrm{L}}[\mathrm{Hz}]$	$\Delta\nu_{\mathrm{L}}[\mathrm{Hz}]$	Mass [208] [$\mathrm{M}_{\odot}$]
XTE J1550-564	276	± 3	184	± 5	9.1 ± 0.61
GRS 1915+105	168	± 3	113	± 5	$12.4^{+2.0}_{-1.8}$
GRO J1655-40	451	± 5	298	± 4	5.4 ± 0.3
M82 X-1	5.07	± 0.06	3.32	± 0.06	415 ± 63

Below, we analyze obtaining estimations of the NED and PFDM field parameters, including BH parameters, using the upper and lower frequencies of the QPO sources given in Table: 3.1 in the QPO models we further discuss.

3.6.1 QPO models and orbits

In this subsection, we study the potential outcomes of lower and upper frequencies through the following models of twin peak QPOs, which can be described by the fundamental frequencies of test particles around compact gravitating objects:

- Stella and Vietri introduced the relativistic precession (RP) model to explain kHz twin-peak QPOs within the $0.2 - 1.25$kHz frequency range observed from neutron stars in low-mass X-ray binaries (LMXRBs). This model also applies to black holes in binary systems, allowing precise estimation of the mass and spin of the central black hole in microquasars by analyzing the power-density spectrum of the accretion disk. In the RP model, the upper and lower frequencies correspond to the radial, vertical, and orbital oscillation frequencies of test particles within the accretion disk near ISCO, defined as $\nu_U = \nu_\phi$ and $\nu_L = \nu_\phi - \nu_r$.

- The epicyclic resonance (ER) model explores different resonance scenarios in axisymmetric oscillations occurring within a thin accretion disk around black holes. This model links disk oscillation frequencies and tests particles' orbital and epicyclic frequencies in circular geodesics. This study focuses on specific subcases of the ER

model, namely ER2, ER3, and ER4, with their respective upper and lower frequencies given by: ER2: $\nu_U = 2\nu_\theta - \nu_r, \nu_L = \nu_r$; ER3: $\nu_U = \nu_\theta + \nu_r, \nu_L = \nu_\theta$; ER4: $\nu_U = \nu_\theta + \nu_r, \nu_L = \nu_\theta - \nu_r$.

- The warped disk (WD) model is based on non-axisymmetric oscillatory modes within a thin accretion disk surrounding black holes and neutron stars. In this framework, the upper and lower frequencies are expressed as $\nu_U = 2\nu_\phi - \nu_r$ and $\nu_L = 2(\nu_\phi - \nu_r)$. Here, the vertical oscillation frequency is introduced by assuming vertical axisymmetric oscillations of the accretion disk, leading to a warped disk structure.

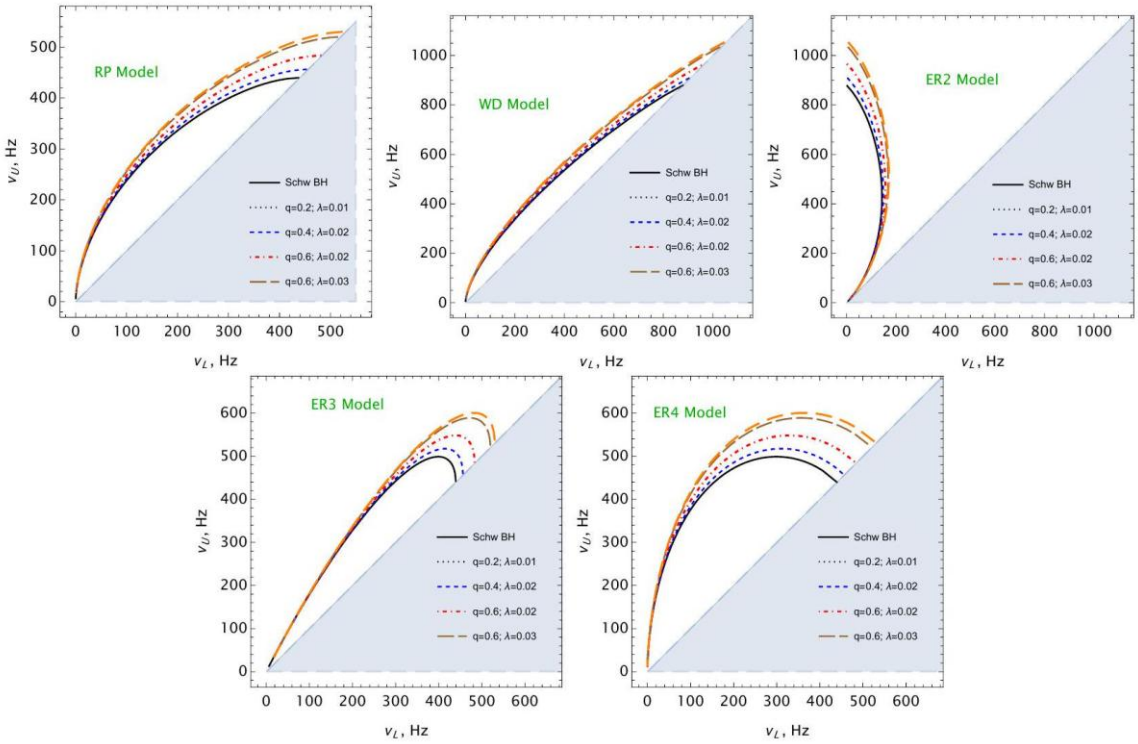


Figure 3.13: The relationship between the upper and lower frequencies around a Schwarzschild BH surrounded by NED field and PFDM for the different parameter values q and λ. Diagrams are shown in the RP, ER, and WD models from top left to bottom right.

Figure 3.13 illustrates the influence of magnetic charge (q) and PFDM, (λ) on the upper (ν_U) and lower (ν_L) QPO frequencies in different theoretical models: RP, WD, and ER2, ER3, ER4. Increasing q raises both ν_U and ν_L in all models, indicating stronger radial and vertical oscillations of particles in the accretion disk. The RP, ER3,

and ER4 models show a steeper increase in QPO frequencies, suggesting that magnetic charge enhances relativistic precession and epicyclic resonances. This effect is more significant at smaller radii, shifting QPO sources closer to the black hole. In contrast, the PFDM parameter primarily affects the QPO frequencies at larger disk radii, particularly in the WD and ER2 models, where it modifies vertical oscillations. The WD model shows a substantial increase in both ν_U and ν_L with λ, indicating that PFDM influences the warping of the accretion disk and alters resonant conditions. The ER2 and ER3 models suggest that PFDM affects radial oscillation modes more than vertical ones, modifying QPO resonance structures at large widths. In other words, both magnetic charge and PFDM significantly alter QPO frequencies. Still, q dominates near the ISCO differently, enhancing relativistic precession and epicyclic resonances, while λ modifies disk warping and resonance conditions at larger radii*. These effects could provide observational signatures of modified black hole spacetimes in future X-ray studies. Here, we study the outer orbits of ISCO where a twin peak QPO occurs in the RP, ER2-4, and WD models using the set of equations $m\nu_L(M,r,q) = n\nu_U(M,r,q)$ where m and n are integers.

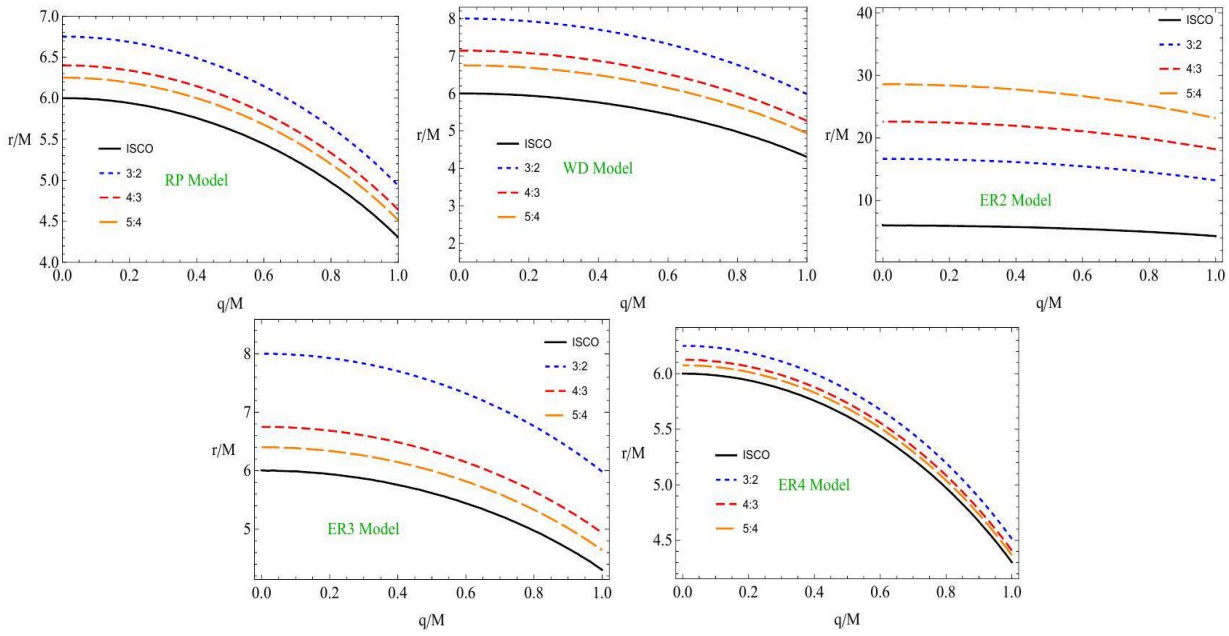


Figure 3.14: QPO radius as a function of q.

Fig. 3.14 illustrates the dependence of the quasi-periodic oscillation (QPO) radius on the magnetic charge parameter q in different QPO models, including the RP, WD, and ER2-4 models. The vertical axis represents the radial coordinate r/M, normalized by the black hole mass, while the horizontal axis displays the variation of the magnetic charge q/M. As q increases, the QPO radius moves outward in all models, signifying that magnetically charged black holes allow QPOs to occur at larger radii than the standard Schwarzschild case. The effect is particularly strong in the ER2 model, where the QPO radius increases significantly with q. In contrast, the RP and ER4 models predict that QPO orbits remain close to the ISCO even as q grows, suggesting a weaker dependence on the magnetic charge.

These results indicate that magnetic charge influences the location of oscillatory modes in accretion disks, which could be observable in X-ray binary systems. Future high-precision QPO observations could help constrain q and distinguish between different QPO models in magnetically charged black hole spacetimes.

Now, we analyze the distance between the ISCO and QPO orbit as ($\delta = r_{QPO} - r_{ISCO}$) for the QPOs observed in GRS $1915 + 105$ and XTE 1550564. Here, we assume an NED field and PFDM surround the central BH. The frequencies of the QPO sources in the microquasars GRS 1915+105 and XTE $1550 - 564$ are $\nu_U = 168 \pm 5$ Hz and $\nu_L = 113 \pm 3$ Hz, and $\nu_U = 184 \pm 5$ Hz and $\nu_L = 276 \pm 3$ Hz. The graphical representation is shown in Fig. 3.15.

Figure 3.15 presents the dependence of QPO orbits on the magnetic charge (q) for two microquasars, GRS $1915 + 105$ and XTE 1550-564, under different QPO models: the RP, ER3, ER4, and the WD models. The figure quantifies how the outermost stable orbit where QPOs occur shifts as the black hole's magnetic charge increases, comparing these results with the ISCO.

Each panel illustrates the QPO radius (r_{QPO}) as a function of q, normalized to the black hole mass (M). The upper row shows results for the zero PFDM parameter ($\lambda = 0$), while the lower row is for $\lambda = 0.03$. The curves corresponding to different

QPO resonance conditions (3:2, 4:3, 5:4) indicate the relative positions of resonant orbits.

As q increases, the QPO orbit shifts inward, approaching the ISCO. This effect is more pronounced in the RP and ER3 models. The WD model consistently predicts larger QPO radii, suggesting that warped disk oscillations are less sensitive to the magnetic charge than radial or vertical resonance models.

At low values of q, the QPO orbit remains far from ISCO, implying that magnetic effects are negligible in this regime. As q increases beyond 0.5 , the QPO orbit contracts significantly in all models. For $q \to 1$, QPOs occur very close to ISCO, suggesting that strong magnetic fields can influence accretion disk oscillations and affect QPO detectability.

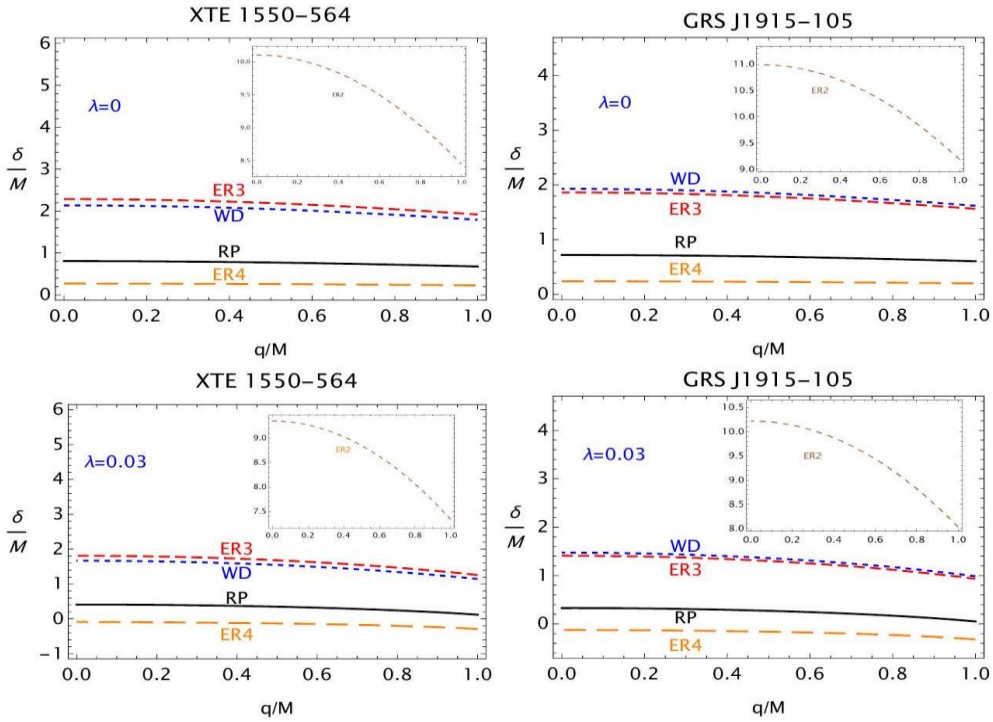


Figure 3.15: Distance between QPO orbits and ISCO as a function of the magnetic charge q, in RP, ER2-4, and WD models. The microquasars GRS J1915+105 (right column) and XTE 1550-564 (left column), $\lambda = 0$ case is in the top row, in the bottom row, we fixed $\lambda = 0.03$.

Comparing the panels of the top for the case $\lambda = 0$ and the bottom one for $\lambda = 0.03$, we see that including PFDM slightly expands QPO orbits for all models. This suggests that PFDM weakens the magnetic charge's inward pull, allowing QPO orbits to remain slightly farther from ISCO than in the pure Schwarzschild case. The contraction of QPO orbits due to increasing q suggests that a strong magnetic charge's gravitational effect could enhance the frequency of QPOs, making them detectable at higher ranges. The inclusion of PFDM modifies the resonance structure, indicating that dark matter-like fields could influence black hole accretion physics. This figure highlights the importance of magnetic charge and PFDM effects in black hole oscillation models, providing a potential avenue for observational constraints through QPO measurements.

3.7 MCMC priors for Black Holes Coupled to NED and Surrounded by PFDM

The present section is devoted to deriving constraints on the expressions' mass and metric parameters (3.14). Here, we select two BH candidates. The BHs depend on the mass of different classes, namely stellar and intermediatemass. For example, we use Well-known stellar mass BHs at the center of the microquasars GRS 1915+105, GRO J1655-40, and XTE 1550-564. QPO data from (ii) M82 X-1 were also used. The intermediate-mass BH is located in the ultraluminous X-ray source in galaxy M82. We employ the Python library emcee [114-116] to get the constraints, we then perform MCMC analysis in the RP model. The posterior distribution is [117],

$$\mathcal{P}(\theta \mid \mathcal{D}, \mathcal{M}) = \frac{P(\mathcal{D} \mid \theta, \mathcal{M})\pi(\theta \mid \mathcal{M})}{P(\mathcal{D} \mid \mathcal{M})}, \tag{3.49}$$

where the functions: $\pi(\theta)$ is the prior function and $P(\mathcal{D} \mid \theta, M)$ is the likelihood one. We consider priors to have a normal distribution known as Gaussian distribution within suitable boundaries (see Tables 3.2 and 3.3), i.e., $\pi(\theta_i) \sim \exp\left[-\frac{1}{2}\left(\frac{\theta_i - \theta_{0,i}}{\sigma_i}\right)^2\right], \theta_{\text{low},i} < \theta_i < \theta_{\text{high},i}$. Here, the parameters are $\theta_i = \{M, q, \lambda, r\}$ and σ_i are their deviations. We provide MCMC analysis using the orbital, vertical, and

radial frequencies calculated in the previous section. The likelihood function Λ has form,

$$\log \Lambda = \log \Lambda_{\mathrm{U}} + \log \Lambda_{\mathrm{L}} \tag{3.50}$$

where $\log \Lambda_{\mathrm{U}}$ denotes the likelihood of the upper frequencies, as

$$\log \Lambda_{\mathrm{U}} = -\frac{1}{2}\sum_{i} \frac{\left(\nu^{i}_{\phi,\mathrm{obs}} - \nu^{i}_{\phi,\mathrm{th}}\right)^{2}}{\left(\sigma^{i}_{\phi,\mathrm{obs}}\right)^{2}}, \tag{3.51}$$

where $\log \Lambda_{\mathrm{L}}$ is the probability (likelihood) of the lower frequency data as a form

$$\log \Lambda_{\mathrm{L}} = -\frac{1}{2}\sum_{i} \frac{\left(\nu^{i}_{\mathrm{L,obs}} - \nu^{i}_{\mathrm{L,th}}\right)^{2}}{\left(\sigma^{i}_{\mathrm{L,obs}}\right)^{2}} \tag{3.52}$$

Here $\nu^{i}_{\phi,\mathrm{obs}}, \nu^{i}_{\mathrm{L,obs}}$ are direct observational results of the orbital/Keplerian frequencies (ν_{K}), periastron precession frequencies $\nu_{\mathrm{L}} = \nu_{\mathrm{K}} - \nu_{\mathrm{r}}$ for the source of our interest. On the other side, $\nu^{i}_{\phi,\,\mathrm{th}}, \nu^{i}_{\mathrm{L,\,th}}$ are the respective theoretical estimations.

Table 3.2: The Gaussian priors (μ is the mean value and σ the variance) of magnetically charged BHs from QPOs.

P	XTE J1550-564		GRS 1915+105		GRO J1655-40		M82 X-1	
	μ	σ	μ	σ	μ	σ	μ	σ
$M/M_{\odot}$	6.9722	1.0458	11.5508	1.7326	4.2666	0.5546	372.77	44.64
q/M	0.0692	0.0103	0.0526	0.0079	0.024	0.0035	0.045	0.0067
λ/M	0.0225	0.0033	0.0241	0.0036	0.028	0.0042	0.0202	0.003
r/M	6.424	0.9634	6.3826	0.9573	6.4036	0.9605	6.5119	0.9768

We chose data from QPOs observed in X-ray binaries: GRS 1915+105, GRO J1655-40, XTE J1550-564, and M82 X-1 with well-reported observational results, as presented in Table 3.1. Next, we perform the MCMC simulation to constrain the parameters (M, q, λ, r) for magnetically charged BHs. We use Gaussian priors based on parameter values from existing literature on QPO data processing. We sampled approximately 10^{5} points from a prior Gaussian distribution for each parameter. This

allowed us to explore the physically possible parameter space within set boundaries and identify the best-fitting parameter values.

Having established the priors, we use the available data to perform an MCMC simulation to determine the plausible range of the parameters $\{M, q, \lambda, r\}$ for magnetically charged BH spacetime. Considering the Gaussian prior distribution, we sample 1×10^5 points for every parameter. This approach allows us to investigate the physically allowed multidimensional parameter space within defined limits and obtain the parameter values that best match the data.

P	XTE J1550-564	GRS 1915+105	GRO J1655-40	M82 X-1
$M/M_{\odot}$	$6.9792^{+0.7642}_{-1.0218}$	$9.9321^{+1.1902}_{-1.0328}$	$4.8654^{+0.4159}_{-0.3854}$	$419.671^{+34.424}_{-32.544}$
q/M	$0.0692^{+0.0103}_{-0.0102}$	$0.0525^{+0.0078}_{-0.0078}$	$0.0241^{+0.0036}_{-0.0036}$	$0.045^{+0.0066}_{-0.0067}$
λ/M	$0.0225^{+0.0033}_{-0.0033}$	$0.024^{+0.0036}_{-0.0036}$	$0.0281^{+0.0042}_{-0.0042}$	$0.0203^{+0.003}_{-0.003}$
r/M	$6.4191^{+0.8775}_{-0.8479}$	$6.0961^{+0.884}_{-0.8433}$	$7.1962^{+0.8014}_{-0.7762}$	$7.3697^{+0.8113}_{-0.7783}$

Table 3.3: Best fit values of M, q, λ, and r parameters for XTE J1550-564, GRS 1915+105, GRO J1655-40 and M82 X-1

In Fig. 3.16, we show the results of the MCMC analysis of the parameters $\{M, q, \lambda, r\}$ by using the QPO data from 4 different magnetically charged BHs (three candidates of stellar-mass BH and one intermediate-mass BH) with magnetic charged sourced by NED field and surrounded by PFDM. The goal is to compare observational data from QPOs in microquasars with theoretical predictions based on the modified Schwarzschild metric.

The figure consists of contour plots and posterior distributions that indicate the statistical confidence levels for each parameter. The MCMC algorithm samples the likelihood function, which is constructed using the fundamental frequencies from the QPO models.

Each subplot presents different parameter correlations. The diagonal elements show the marginalized probability distributions for individual parameters, while the

off-diagonal plots display 2D confidence contours (e.g., M vs. q, q vs. λ, etc.), typically including $68\%(3\sigma)$,$95\%(2\sigma)$, and $99.7\%(1\sigma)$ confidence intervals. These contours provide insight into how well the observational data constrain the parameters. The shaded regions on the contour plots reflect these confidence levels.

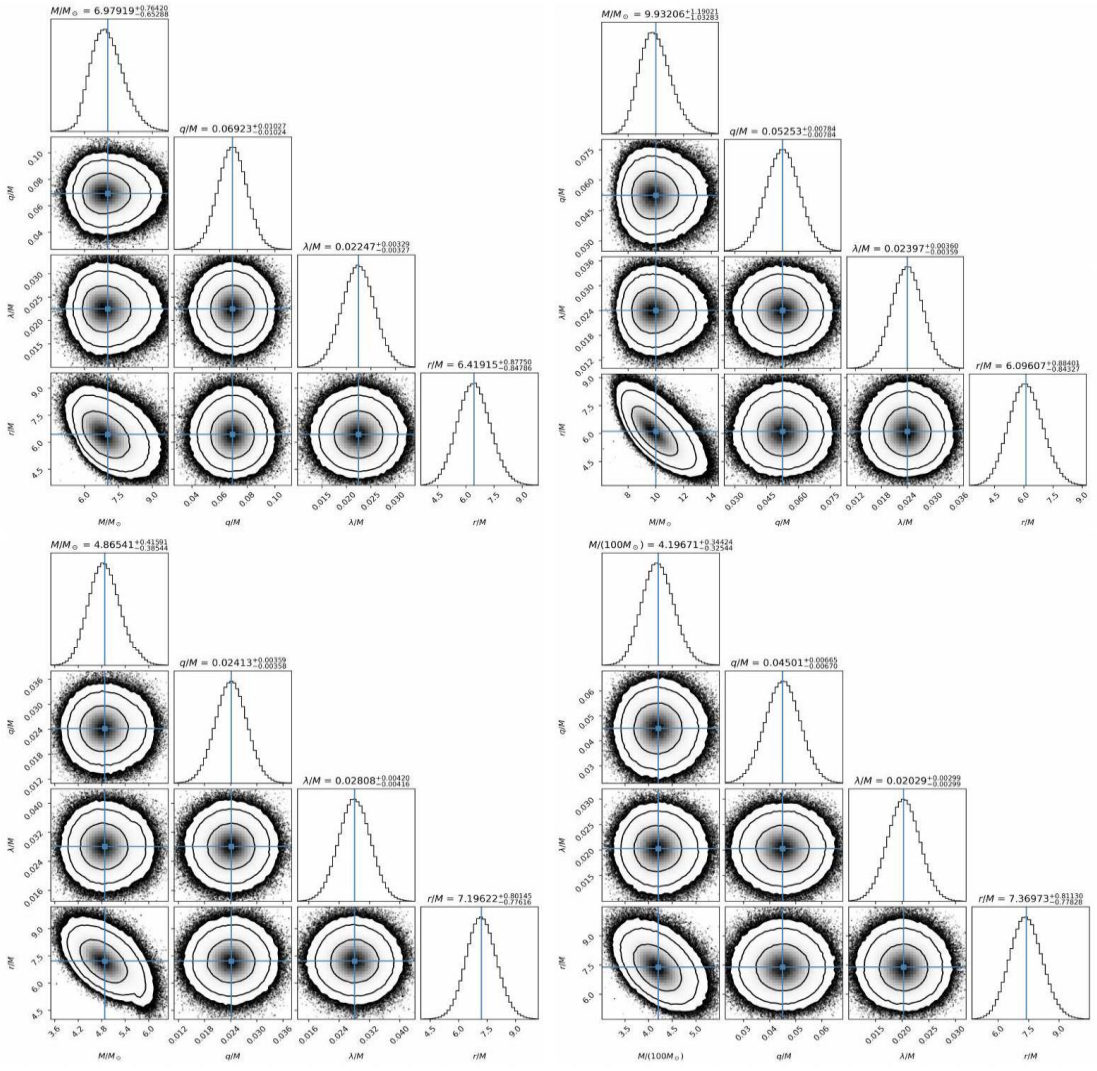


Figure 3.16: Constraints on magnetically charged BH parameters of the QPO orbit from a fourdimensional MCMC analysis using the QPO data for the stellar-mass BHs XTE J1550-564 (top left), GRS 1915+105 (top right), and GRO J1655-40 (bottom left) and intermediate-mass BHs M82 X-1 (bottom right) in the RP model.

Increasing q tends to shift the posterior mass distribution toward slightly lower values, indicating that magnetically charged black holes may appear less massive in QPO analysis than their Schwarzschild counterparts. Similarly, λ affects the orbital

frequencies, causing minor shifts in the estimated black hole mass. The contours also reveal strong degeneracies between parameters; for instance, an increase in λ can compensate for a lower q in determining QPO frequencies.

The results suggest that for black holes in microquasars such as GRS $1915+105$, GRO J1655-40, and XTE 1550-564, the best-fit values of q and λ remain within physically viable ranges. These constraints provide indirect observational evidence for the effects of nonlinear electrodynamics and PFDM in strong gravity regimes.

We use the emcee package to obtain the posterior distribution with the possible choice of the prior given in Tables 3.2 and 3.3.

3.8 Conclusion

This study investigated the physical properties of black holes embedded in an NED framework and surrounded by PFDM. By deriving a modified black hole metric, we explored its influence on key astrophysical processes, including test particle dynamics, accretion disk properties, and QPOs.

The spacetime structure of these black holes exhibits significant modifications due to the presence of both magnetic charge and PFDM. The derived metric function shows that the event horizon decreases with increasing magnetic charge, while PFDM has a more subtle influence on horizon structure.

The black hole's effective mass is also altered, affecting the gravitational interactions in its vicinity. The radiation properties of the accretion disk, analyzed using the NovikovThorne model, indicate that the electromagnetic flux and temperature increase with stronger magnetic charge and higher PFDM density. This suggests that such black holes could be associated with more luminous accretion disks, which may be observable through X-ray and gamma-ray emissions. QPOs, crucial tools for probing strong gravity regions, were found to be strongly influenced by the black hole's charge and dark matter environment. The fundamental frequencies of orbital motion, including radial and vertical epicyclic frequencies, were significantly altered, affecting the interpretation of observational data from X-ray binaries and microquasars. These

findings suggest that incorporating magnetic and dark matter effects into QPO models could improve the accuracy of black hole mass and spin estimates. Using MCMC simulations, we placed constraints on the mass, charge, and PFDM parameters of observed black hole candidates, including XTE J1550564, GRS 1915+105, GRO J1655-40, and M82 X-1. The results provide new insights into the astrophysical relevance of these modified gravity models. Our findings provide a theoretical framework for future observational studies to detect these effects. Future work should focus on obtaining more precise observational constraints using upcoming space-based X-ray observatories, which may confirm or refine the theoretical predictions presented in this study. Overall, it also highlights the potential of X-ray observations to probe modifications to general relativity and test alternative gravity models. Future high-precision QPO data, such as those from XRISM or Athena, could further refine these constraints and offer deeper insights into black hole physics beyond the Schwarzschild paradigm.

MAIN RESULT OF THE DISSERTATION:

The following conclusions were presented based on research carried out on the topic of "Fundamental frequencies and thermodynamical properties of black holes in the presence of external matter fields" for the Doctor of Philosophy (PhD) dissertation

1. It has been shown that the Chaplygin-like dark fluid significantly modifies the event-horizon structure of black holes. In particular, the equation-of-state parameter leads to an enlargement of the event horizon, whereas the fluid-strength parameter reduces the horizon area.

2. It has been established that perfect fluid dark matter surrounding black holes considerably affects their thermodynamical properties. As the PFDM contribution increases, the maximum value of the Hawking temperature becomes higher than in the vacuum case, while the phase-transition point shifts from smaller to larger event-horizon radii. It has also been shown that the thermodynamical behavior of more massive black holes is more sensitive to the PFDM contribution.

3. It has been obtained that the Chaplygin-like fluid strength causes an inward shift of the orbital radii corresponding to QPOs with a 3:2 frequency ratio. This indicates that, as the dark-fluid contribution becomes stronger, QPO signals are generated at orbits closer to the black hole, where the gravitational field is stronger.

4. It has been demonstrated that the MCMC-based QPO analysis of XTE J1550–564, GRO J1655–40, GRS 1915+105, and M82 X-1 provides constrained mass values consistent with independent observational results within the PFDM parameter ranges $q \in [0.024, 0.069]$ and $\lambda \in [0.020, 0.028]$. This confirms that QPO observations can serve as an effective tool for constraining the black hole charge and PFDM parameters.

BIBLIOGRAPHY

1. N. Aghanim, Y. Akrami, M. Ashdown, J. Aumont, C. Baccigalupi, M. Ballardini, et al., "Planck 2018 results-vi. cosmological parameters," Astronomy & Astrophysics, vol. 641, p. A6, 2020.

2. V. Kiselev, "Quintessence and black holes," Classical and Quantum Gravity, vol. 20, no. 6, p. 1187, 2003.

3. M. Chun-Rui, G. Yuan-Xing, and W. Fu-Jun, "Quintessence contribution to a schwarzschild black hole entropy," Chinese Physics Letters, vol. 24, no. 11, p. 3286, 2007.

4. S. Fernando, "Schwarzschild black hole surrounded by quintessence: null geodesics," General Relativity and Gravitation, vol. 44, pp. 18571879, 2012.

5. Z. Feng, L. Zhang, and X. Zu, "The remnants in reissner-nordström-de sitter quintessence black hole," Modern Physics Letters A, vol. 29, no. 26, p. 1450123, 2014.

6. B. Malakolkalami and K. Ghaderi, "Schwarzschild-anti de sitter black hole with quintessence," Astrophysics and Space Science, vol. 357, no. 2, p. 112, 2015.Hussain and S. Ali, "Effect of a quintessence model on the energy of the reissner-nordström black hole," General Relativity and Gravitation, vol. 47, no. 4, p. 34, 2015.

7. S. G. Ghosh, M. Amir, and S. D. Maharaj, "Quintessence background for 5d einstein-gauss-bonnet black holes," The European Physical Journal C, vol. 77, pp. 1-9, 2017.

8. S. G. Ghosh, S. D. Maharaj, D. Baboolal, and T. H. Lee, "Lovelock black holes surrounded by quintessence," The European Physical Journal C, vol. 78, pp. 1-8, 2018.

9. J. D. M. Toledo and V. B. Bezerra, "Black holes with cloud of strings and quintessence in lovelock gravity," The European Physical Journal C, vol. 78, pp. 1-12, 2018.

10. Y. Sekhmani, J. Rayimbaev, R. Myrzakulov, and D. J. Gogoi, "Phase structure of charged ads black holes surrounded by external matter fields fluid with modified chaplygin equation of state," 2023.

11. R. Bean and O. Dore, "Are chaplygin gases serious contenders for the dark energy?," Physical Review D, vol. 68, no. 2, p. 023515, 2003.

12. M. C. Bento, O. Bertolami, and A. A. Sen, "Generalized chaplygin gas, accelerated expansion, and dark-energy-matter unification," Physical Review D, vol. 66, no. 4, p. 043507, 2002.

13. N. Bilic, G. B. Tupper, and R. D. Viollier, "Unification of dark matter and dark energy: The inhomogeneous chaplygin gas," Physics Letters B, vol. 535, no. 1-4, pp. 17-21, 2002.

14. V. Gorini, A. Y. Kamenshchik, and U. Moschella, "Can the chaplygin gas be a plausible model for dark energy?," Physical Review D, vol. 67, no. 6, p. 063509, 2003.

15. Y. Kamenshchik, U. Moschella, and V. Pasquier, "An alternative to quintessence," Physics Letters B, vol. 511, no. 2-4, pp. 265-268, 2001.

16. M. Makler, S. Q. de Oliveira, and I. Waga, "Constraints on the generalized chaplygin gas from supernovae observations," Physics Letters B, vol. 555, no. 1-2, pp. 1-6, 2003.

17. G. Abbas, H. Rehman, T. Zhu, Q. Wu, and G. Mustafa, "Accretion disk around reissner-nordström black hole coupled with a nonlinear electrodynamics field," 2023.

18. D. Arora, N. U. Molla, H. Chaudhary, U. Debnath, F. Atamurotov, and G. Mustafa, "Exploring tidal force effects and shadow constraints for schwarzschild-like black hole in starobinsky-bel-robinson gravity," 2023.

19. H. Rehman, G. Abbas, T. Zhu, and G. Mustafa, "Matter accretion onto the magnetically charged euler-heisenberg black hole with scalar hair," The European Physical Journal C, vol. 83, no. 9, p. 856, 2023.

20. M. Yasir, T. Xia, F. Javed, and G. Mustafa, "Thermal analysis and joule-thomson expansion of black hole exhibiting metric-affine gravity," Chinese Physics C, vol. 48, no. 1, p. 015103, 2024.

21. G. Mustafa, Z. Hassan, and P. K. Sahoo, "Deflection of light by wormholes and its shadow due to dark matter within modified symmetric teleparallel gravity formalism," 2024.

22. G. Mustafa, F. Javed, A. Waseem, S. K. Maurya, and G. Fatima, "Imprints of dark energy models on structural properties of charged gravastars in extended teleparallel gravity," 2024.

23. G. Mustafa, F. Javed, S. K. Maurya, and A. Errehymy, "New embedded wormhole solutions in ricci inverse gravity," 2024.

24. F. Javed, A. Waseem, G. Mustafa, F. Tchier, F. Atamurotov, B. Ahmedov, and A. Abdujabbarov, "Constraining study of charged gravastars solutions in symmetric teleparallel gravity," Chinese Journal of Physics, vol. 90, pp. 410-421, 2024.

25. G. Mustafa, "Ricci inverse gravity wormholes," Physics Letters B, vol. 848, p. 138407, 2024.

26. G. Mustafa, A. Ditta, F. Javed, F. Atamurotov, I. Hussain, and B. Ahmedov, "Probing black hole in starobinsky-bel-robinson gravity with thermodynamical analysis, effective force and gravitational weak lensing," 2024.

27. G. Mustafa, A. Ditta, F. Javed, S. K. Maurya, H. Chaudhary, and F. Atamurotov, "A study on matter accretion onto charged black hole solution in metric-affine gravity," 2023.

28. D. Arora, M. Yasir, H. Chaudhary, F. Javed, G. Mustafa, T. Xia, and F. Atamurotov, "Joule-thomson expansion and tidal force effects of ads black holes surrounded by chaplygin dark fluid," 2023.

29. N. U. Molla, H. Chaudhary, D. Arora, F. Atamurotov, U. Debnath, and G. Mustafa, "Strong gravitational lensing by sgr a* and m87^* black holes embedded in dark matter halo exhibiting string cloud and quintessential field," 2023.

30. Ditta, G. Mustafa, G. Abbas, F. Atamurotov, and K. Jusufi, "Constraining study of circular orbits and accretion disk around nonlinear electrodynamics black hole," Journal of Cosmology and Astroparticle Physics, vol. 2023, no. 08, p. 002, 2023.

31. R. Ali, R. Babar, M. Asgher, and G. Mustafa, "Tunneling analysis of null aether black hole theory in the background of newman-janis algorithm," International Journal of Modern Physics A, vol. 37, no. 22, p. 2250134, 2022.

32. V. Poulin, T. L. Smith, and A. Bartlett, "Dark energy at early times and act data: A larger hubble constant without late-time priors," Physical Review D, vol. 104, no. 12, p. 123550, 2021.

33. X. Q. Li, H. P. Yan, L. L. Xing, and S. W. Zhou, "Critical behavior of ads black holes surrounded by dark fluid with chaplygin-like equation of state," 2023.

34. B. Pourhassan and E. O. Kahya, "Extended chaplygin gas model," Results in Physics, vol. 4, pp. 101-102, 2014.

35. B. Pourhassan and E. O. Kahya, "Frw cosmology with the extended chaplygin gas," Advances in High Energy Physics, vol. 2014, p. 231452, 2014.

36. E. O. Kahya, M. Khurshudyan, B. Pourhassan, R. Myrzakulov, and A. Pasqua, "Higher order corrections of the extended chaplygin gas cosmology with varying g and λ," The European Physical Journal C, vol. 75, no. 2, p. 86, 2015.

37. M. Hassaine and C. Martinez, "Higher-dimensional black holes with a conformally invariant maxwell source," Physical Review D, vol. 75, no. 2, p. 027502, 2007.

38. B. Hoffmann, "Gravitational and electromagnetic mass in the borninfeld electrodynamics," Physical Review, vol. 47, no. 11, p. 877, 1935.

39. Y. Sekhmani, G. Luciano, J. Rayimbaev, M. Jasim, A. Al-Badawi, and S. Maurya, "Topological ads black holes surrounded by chaplygin dark fluid: From stability to geometrothermodynamic analysis," Physics of the Dark Universe, vol. 46, p. 101567, 2024.

40. T. K. Dey, "Born-infeld black holes in the presence of a cosmological constant," Physics Letters B, vol. 595, no. 1-4, pp. 484-490, 2004.

41. R. G. Cai, D. W. Pang, and A. Wang, "Born-infeld black holes in (a)ds spaces," Physical Review D, vol. 70, no. 12, p. 124034, 2004.

42. G. Mustafa, S. Maurya, A. Ditta, S. Ray, and F. Atamurotov, "Circular orbits and accretion disk around ads black holes surrounded by dark fluid with chaplygin-like equation of state," The European Physical Journal C, vol. 84, p. 690, 2024.

43. D. Arora, M. Yasir, H. Chaudhary, F. Javed, G. Mustafa, X. Tiecheng, and F. Atamurotov, "Joule-thomson expansion and tidal force effects of ads black holes surrounded by chaplygin dark fluid," 2023.

44. Ditta, F. Javed, G. Mustafa, F. Atamurotov, and S. Salimov, "Particle dynamics and fundamental frequencies of black hole coupled with a nonlinear electrodynamics field," Journal of High Energy Astrophysics, vol. 43, pp. 51-60, 2024.

45. Ashraf, A. Ditta, D. Sofuoğlu, W. Ma, F. Javed, F. Atamurotov, and A. Mahmood, "Quasi-periodic oscillations and particle motion around charged black hole surrounded by a cloud of strings and quintessence field in rastall gravity," Physica Scripta, vol. 99, no. 6, p. 065011, 2024.

46. D. Carturan and F. Finelli, "Cosmological effects of a class of fluid dark energy models," Physical Review D, vol. 68, no. 10, p. 103501, 2003.

47. L. Amendola, F. Finelli, C. Burigana, and D. Carturan, "Wmap and the generalized chaplygin gas," Journal of Cosmology and Astroparticle Physics, vol. 2003, no. 07, p. 005, 2003.

48. F. Mushtaq, X. Tiecheng, A. Ditta, F. Atamurotov, A. Abduvokhidov, and A. Asalkhon, "Weak gravitational lensing and fundamental frequencies of einstein-euler-heisenberg black hole," New Astronomy, vol. 108, p. 102185, 2024.

49. Y. Feng, A. Ashraf, S. Mumtaz, S. Maurya, G. Mustafa, and F. Atamurotov, "Orbital motion and epicyclic oscillations around bardeen black hole surrounded by perfect fluid dark matter," Journal of High Energy Astrophysics, vol. 43, pp. 158-170, 2024.

50. A. Nosirov, F. Atamurotov, G. Rakhimova, A. Abdujabbarov, and S. Ghosh, "Particle acceleration near a rotating charged black hole in 4d einstein-gauss-bonnet gravity," Nuclear Physics B, vol. 1005, p. 116583, 2024.

51. K. Karshiboev, F. Atamurotov, A. Övgün, A. Abdujabbarov, and E. Karimbaev, "Particle dynamics and thermodynamical analysis of the rotating modmax black holes," New Astronomy, vol. 109, p. 102200, 2024.

52. A. Ditta, X. Tiecheng, F. Atamurotov, I. Hussain, and G. Mustafa, "Particle dynamics, black hole shadow and weak gravitational lensing in the f(q) theory of gravity," Communications in Theoretical Physics, vol. 75, no. 12, p. 125404, 2023.

53. Nosirov, F. Atamurotov, G. Rakhimova, and A. Abdujabbarov, "Particle acceleration and thermodynamics of the rotating simpson- visser black hole," The European Physical Journal Plus, vol. 138, p. 846, 2023.

54. X. Q. Li, B. Chen, and L. L. Xing, "Charged lovelock black holes in the presence of dark fluid with a nonlinear equation of state," The European Physical Journal Plus, vol. 135, no. 2, p. 175, 2020.

55. J. L. Jaramillo and E. Gourgoulhon, "Mass and angular momentum in general relativity," Fundamental Theories of Physics, vol. 162, p. 87, 2011.

56. J. Rayimbaev, N. Juraeva, M. Khudoyberdiyeva, A. Abdujabbarov, and M. Abdullaev, "Quasiperiodic oscillations and dynamics of test particles around regular-kiselev black holes," Galaxies, vol. 11, no. 6, p. 113, 2023.

57. A. Ditta, X. Tiecheng, S. Mumtaz, F. Atamurotov, G. Mustafa, and A. Abdujabbarov, "Testing metric-affine gravity using particle dynamics and photon motion," Physics of the Dark Universe, vol. 41, p. 101248, 2023.

58. L. Angelini, L. Stella, and A. N. Parmar, "The discovery of 0.2 hz quasiperiodic oscillations in the x-ray flux of the transient 42 second pulsar exo 2030+375," The Astrophysical Journal, vol. 346, pp. 906-911, 1989.

59. M. Alloqulov, F. Atamurotov, A. Abdujabbarov, and B. Ahmedov, "Probing hořava-lifshitz gravity using particle and photon dynamics in the presence of plasma," Chinese Physics C, vol. 47, no. 7, p. 075103, 2023.

60. A. Ditta, X. Tiecheng, F. Atamurotov, G. Mustafa, and M. Aripov, "Particle dynamics and weak gravitational lensing around nonlinear electrodynamics black hole," Chinese Journal of Physics, vol. 83, pp. 664-679, 2023.

61. S. Kato and J. Fukue, "Trapped radial oscillations of gaseous disks around a black hole," Publications of the Astronomical Society of Japan, vol. 32, p. 377, 1980.

62. M. A. Abramowicz and W. Kluźniak, "A precise determination of black hole spin in gro j1655-40," Astronomy & Astrophysics, vol. 374, no. 3, pp. L19-L20, 2001.

63. R. V. Wagoner, A. S. Silbergleit, and M. Ortega-Rodriguez, "stable" quasi-periodic oscillations and black hole properties from diskoseismology," The Astrophysical Journal, vol. 559, no. 1, p. L25, 2001.

64. S. Silbergleit, R. V. Wagoner, and M. Ortega-Rodríguez, "Relativistic diskoseismology. ii. analytical results for c-modes," The Astrophysical Journal, vol. 548, no. 1, p. 335, 2001.

65. D. H. Wang, L. Chen, C. M. Zhang, Y. J. Lei, J. L. Qu, and L. M. Song, "Investigation of the emission radii of khz qpos for the accreting millisecond x-ray pulsars, atoll and z sources," Monthly Notices of the Royal Astronomical Society, vol. 454, no. 2, pp. 1231-1237, 2015.

66. L. Rezzolla, S. I. Yoshida, T. J. Maccarone, and O. Zanotti, "A new simple model for high-frequency quasi-periodic oscillations in black hole candidates," Monthly Notices of the Royal Astronomical Society, vol. 344, no. 3, pp. L37-L41, 2003.

67. G. Török and Z. Stuchlik, "Radial and vertical epicyclic frequencies of keplerian motion in the field of kerr naked singularities-comparison with the black hole case and possible instability of naked-singularity accretion discs," Astronomy & Astrophysics, vol. 437, no. 3, pp. 775788, 2005.

68. A. Ingram and C. Done, "A physical interpretation of the variability power spectral components in accreting neutron stars," Monthly Notices of the Royal Astronomical Society, vol. 405, no. 4, pp. 2447-2452, 2010.

69. P. C. Fragile, O. Straub, and O. Blaes, "High-frequency and type-c qpos from oscillating, precessing hot, thick flow," Monthly Notices of the Royal Astronomical Society, vol. 461, no. 2, pp. 1356-1362, 2016.

70. Z. Stuchlík, A. Kotrlová, and G. Török, "Multi-resonance orbital model of high-frequency quasi-periodic oscillations: possible high-precision determination of black hole and neutron star spin," Astronomy & Astrophysics, vol. 552, p. A10, 2013.

71. Z. Stuchlík, A. Kotrlova, and G. Török, "Resonant switch model of twin peak hf qpos applied to the source 4 u 1636-53," Acta Astronomica, vol. 62, pp. 389-407, 2012.

72. M. Ortega-Rodríguez, H. Solís-Sánchez, L. Álvarez García, and E. Dodero-Rojas, "On twin peak quasi-periodic oscillations resulting from the interaction between discoseismic modes and turbulence in accretion discs around black holes," Monthly Notices of the Royal Astronomical Society, vol. 492, no. 2, pp. 1755-1760, 2020.

73. Z. Stuchlík, M. Kološ, J. Kovář, P. Slaný, and A. Tursunov, "Influence of cosmic repulsion and magnetic fields on accretion disks rotating around kerr black holes," Universe, vol. 6, no. 2, p. 26, 2020.

74. A. Maselli, G. Pappas, P. Pani, L. Gualtieri, S. Motta, V. Ferrari, and L. Stella, "A new method to constrain neutron star structure from quasi-periodic oscillations," The Astrophysical Journal, vol. 899, no. 2, p. 139, 2020.

75. J. Rayimbaev, K. F. Dialektopoulos, F. Sarikulov, and A. Abdujabbarov, "Quasiperiodic oscillations around hairy black holes in horndeski gravity," The European Physical Journal C, vol. 83, no. 7, p. 572, 2023.

76. J. Rayimbaev, U. Eshimbetov, B. Majeed, A. Abdujabbarov, A. Abduvokhidov, B. Abdulazizov, and A. Xalmirzayev, "Test particles and quasiperiodic oscillations around kiselev black hole with cloud of strings," Chinese Physics C, vol. 48, no. 5, p. 055103, 2024.

77. F. Atamurotov, D. Ortiqboev, A. Abdujabbarov, and G. Mustafa, "Particle dynamics and gravitational weak lensing around black hole in the kalb-ramond gravity," The European Physical Journal C, vol. 82, p. 659, 2022.

78. F. Atamurotov, M. Alloqulov, A. Abdujabbarov, and B. Ahmedov, "Testing the einstein-Æther gravity: particle dynamics and gravitational lensing," The European Physical Journal Plus, vol. 137, p. 634, 2022.

79. J. Rayimbaev, A. Abdujabbarov, and H. Wen-Biao, "Regular nonminimal magnetic black hole as a source of quasiperiodic oscillations," Physical Review D, vol. 103, no. 10, p. 104070, 2021.

80. F. Atamurotov, S. Shaymatov, P. Sheoran, and S. Siwach, "Charged black hole in 4d einstein-gauss-bonnet gravity: particle motion, plasma effect on weak gravitational lensing and centre-of-mass energy," Journal of Cosmology and Astroparticle Physics, vol. 2021, no. 08, p. 045, 2021.

81. G. Babar, F. Atamurotov, S. Ul Islam, and S. Ghosh, "Particle acceleration around rotating einstein-born-infeld black hole and plasma effect on gravitational lensing," Physical Review D, vol. 103, p. 084057, 2021.

82. S. Shaymatov, F. Atamurotov, and B. Ahmedov, "Isofrequency pairing of circular orbits in schwarzschild spacetime in the presence of magnetic field," Astrophysics and Space Science, vol. 350, pp. 413-419, 2014.

83. M. Qi, J. Rayimbaev, and B. Ahmedov, "Charged particles and quasiperiodic oscillations around magnetized schwarzschild black holes," The European Physical Journal C, vol. 83, no. 8, p. 749, 2023.

84. J. Rayimbaev, A. H. Bokhari, and B. Ahmedov, "Quasiperiodic oscillations from noncommutative inspired black holes," Classical and Quantum Gravity, vol. 39, no. 7, p. 075015, 2022.

85. Abbott, S. Jawahar, N. Lockerbie, and K. Tokmakov, "Directly comparing gw150914 with numerical solutions of einstein's equations for binary black hole coalescence," Physical Review D, vol. 94, no. 6, p. 064035, 2016.

86. F. De Paolis, A. Geralico, G. Ingrosso, and A. A. Nucita, "The black hole at the galactic center as a possible retro-lens for the s 2 orbiting star," Astronomy & Astrophysics, vol. 409, no. 3, pp. 809-812, 2003.

87. Bambi, Black holes: a laboratory for testing strong gravity. Singapore: Springer, 2017.

88. M. Zajaček, A. Tursunov, A. Eckart, S. Britzen, E. Hackmann, V. Karas, et al., "Constraining the charge of the galactic centre black hole," Journal of Physics: Conference Series, vol. 1258, no. 1, p. 012031, 2019.

89. Mukhopadhyay, "Lorentz symmetry violation in neutrinos in curved spacetime and its consequences," The Twelfth Marcel Grossmann Meeting, pp. 1471-1473, 2012.

90. M. A. Hohensee, N. Leefer, D. Budker, C. Harabati, V. A. Dzuba, and V. V. Flambaum, "Limits on violations of lorentz symmetry and the einstein equivalence principle using radio-frequency spectroscopy of atomic dysprosium," Physical Review Letters, vol. 111, no. 5, p. 050401, 2013.

91. J. M. Overduin, R. D. Everett, and Q. G. Bailey, "Constraints on violations of lorentz symmetry from gravity probe b ," Proceedings of the Sixth Meeting on CPT and Lorentz Symmetry, pp. 188-191, 2013.

92. R. Aaij, C. Abellán Beteta, B. Adeva, M. Adinolfi, Z. Ajaltouni, S. Akar, et al., "Search for violations of lorentz invariance and cpt symmetry in b(s)0 mixing," Physical Review Letters, vol. 116, p. 241601, 2016.

93. Y. M. P. Gomes, P. C. Malta, and M. J. Neves, "Testing lorentzsymmetry violation via electroweak decays," Physical Review D, vol. 101, no. 7, p. 075001, 2020.

94. Zhang, "The local lorentz symmetry violation and einstein equivalence principle," Journal of Physics B: Atomic, Molecular and Optical Physics, vol. 53, no. 23, p. 235001, 2020.

95. M. Zahid, S. U. Khan, J. Ren, and J. Rayimbaev, "Geodesics and shadow formed by a rotating gauss-bonnet black hole in ads spacetime," International Journal of Modern Physics D, vol. 31, no. 08, p. 2250058, 2022.

96. M. Zahid, J. Rayimbaev, F. Sarikulov, S. U. Khan, and J. Ren, "Shadow of rotating and twisting charged black holes with cloud of strings and quintessence," The European Physical Journal C, vol. 83, no. 9, p. 811, 2023.

97. M. Zahid, S. U. Khan, and J. Ren, "Shadow cast and center of mass energy in a charged gauss-bonnet-ads black hole," Chinese Journal of Physics, vol. 72, pp. 575-586, 2021.

98. Ding, A. Wang, and X. Wang, "Charged einstein-aether black holes and smarr formula," Physical Review D, vol. 92, no. 8, p. 084055, 2015.

99. Zhang, X. Zhao, K. Lin, S. Zhang, W. Zhao, and A. Wang, "Spherically symmetric static black holes in einstein-aether theory," Physical Review D, vol. 102, no. 6, p. 064043, 2020.

100. T. Zhu, Q. Wu, M. Jamil, and K. Jusufi, "Shadows and deflection angle of charged and slowly rotating black holes in einstein-Æther theory," Physical Review D, vol. 100, no. 4, p. 044055, 2019.

101. J. Oost, S. Mukohyama, and A. Wang, "Constraints on einstein-aether theory after gw170817," Physical Review D, vol. 97, no. 12, p. 124023, 2018.

102. M. Azreg-Aïnou, Z. Chen, B. Deng, M. Jamil, T. Zhu, Q. Wu, and Y. K. Lim, "Orbital mechanics and quasiperiodic oscillation resonances of black holes in einstein-Æther theory," Physical Review D, vol. 102, no. 4, p. 044028, 2020.

103. J. Rayimbaev, A. Abdujabbarov, M. Jamil, and W. B. Han, "Dynamics of magnetized particles around einstein-Æther black hole with uniform magnetic field," Nuclear Physics B, vol. 966, p. 115364, 2021.

104. R. Abuter, A. Amorim, M. Bauböck, J. P. Berger, H. Bonnet, W. Brandner, et al., "Detection of orbital motions near the last stable circular orbit of the massive black hole sgra," Astronomy & Astrophysics, vol. 618, p. L10, 2018.

105. M. Shahzadi, M. Kološ, Z. Stuchlík, and Y. Habib, "Testing alternative theories of gravity by fitting the hot-spot data of sgr a," The European Physical Journal C, vol. 82, p. 407, 2022.

106. J. Rayimbaev, B. Ahmedov, and Z. Stuchlik, "Particles with magnetic dipole moment orbiting magnetized schwarzschild black holes: Applications to orbits of hot spots around sgr a," Physics of the Dark Universe, vol. 45, p. 101516, 2024.

107. B. Turimov and O. Rahimov, "The orbital and epicyclic frequencies in axially symmetric and stationary spacetime," Universe, vol. 8, no. 10, p. 507, 2022.

108. S. Murodov, J. Rayimbaev, B. Ahmedov, and E. Karimbaev, "Quasiperiodic oscillations and dynamics of test particles around quasiand non-schwarzschild black holes," Universe, vol. 9, no. 9, p. 391, 2023.

109. S. Murodov, J. Rayimbaev, B. Ahmedov, and A. Hakimov, "Dynamics of particles with electric charge and magnetic dipole moment near schwarzschild-mog black hole," Symmetry, vol. 15, no. 11, p. 2084, 2023.

110. S. Murodov, K. Badalov, J. Rayimbaev, B. Ahmedov, and Z. Stuchlík, "Charged particles orbiting charged black-bounce black holes," Symmetry, vol. 16, no. 1, p. 109, 2024.

111. G. Török, "A possible 3:2 orbital epicyclic resonance in qpo frequencies of sgr a*," Astronomy & Astrophysics, vol. 440, pp. 1-4, 2005.

112. R. Fiorito and L. Titarchuk, "Is m 82 x -1 really an intermediate-mass black hole? x-ray spectral and timing evidence," The Astrophysical Journal, vol. 614, pp. L113-L116, 2004.

113. Abdulkhamidov, P. Nedkova, J. Rayimbaev, J. Kunz, and B. Ahmedov, "Parameter constraints on traversable wormholes within beyond horndeski theories through quasiperiodic oscillations," Physical Review D, vol. 109, no. 10, p. 104074, 2024.

114. Foreman-Mackey, D. W. Hogg, D. Lang, and J. Goodman, "emcee: The mcmc hammer," Publications of the Astronomical Society of the Pacific, vol. 125, no. 925, p. 306, 2013.

115. A. Zhadyranova, M. Koussour, S. Bekkhozhayev, V. Zhumabekova, and J. Rayimbaev, "Exploring late-time cosmic acceleration: A study of a linear f(t) cosmological model using observational data," Physics of the Dark Universe, vol. 45, p. 101514, 2024.

116. Liu, H. Xu, H. Siew, T. Zhu, Q. Wu, and Y. Zhao, "Constraints on the rotating self-dual black hole with quasi-periodic oscillations," 2023.

117. D. Sakharov, "The initial stage of an expanding universe and the appearance of a nonuniform distribution of matter," ZhETF Pis'ma Redaktsiiu, vol. 22, p. 241, 1966.

118. B. Gliner, "Algebraic Properties of the Energy-momentum Tensor and Vacuum-like States o ^+Matter," Soviet Journal of Experimental and Theoretical Physics, vol. 22, p. 378, Feb. 1966.

119. L. E. Gurevich and A. A. Starobinsky, "Cosmological models with a variable effective gravitational constant," Astrophysics and Space Science, vol. 38, pp. 67-74, 1975.

120. A. Starobinsky, "A new type of isotropic cosmological models without singularity," JETP Letters, vol. 30, pp. 682-685, 1979.

121. Y. Kurmanov, K. Boshkayev, T. Konysbayev, O. Luongo, N. Saiyp, A. Urazalina, G. Ikhsan, and G. Suliyeva, "Accretion disks properties around regular black hole solutions obtained from non-linear electrodynamics," Physics of the Dark Universe, vol. 46, p. 101566, Dec. 2024.

122. R. Kumar Walia, "Exploring nonlinear electrodynamics theories: Shadows of regular black holes and horizonless ultracompact objects," Phys. Rev. D, vol. 110, no. 6, p. 064058, 2024.

123. N. Aghanim et al., "Planck 2018 results. VI. Cosmological parameters," Astron. Astrophys., vol. 641, p. A6, 2020. [Erratum: Astron.Astrophys. 652, C4 (2021)].

124. O. Ludwig, "Galactic rotation curve and dark matter according to gravitomagnetism," Eur. Phys. J. C, vol. 81, no. 2, p. 186, 2021.

125. Toshmatov, Z. Stuchlík, and B. Ahmedov, "Rotating black hole solutions with quintessential energy," European Physical Journal Plus, vol. 132, p. 98, Feb. 2017.

126. Rahaman, K. K. Nandi, A. Bhadra, M. Kalam, and K. Chakraborty, "Perfect fluid dark matter," Physics Letters B, vol. 694, pp. 10-15, Oct. 2010.

127. M.-H. Li and K.-C. Yang, "Galactic dark matter in the phantom field," , vol. 86, p. 123015, Dec. 2012.

128. X. Hou, Z. Xu, and J. Wang, "Rotating black hole shadow in perfect fluid dark matter," , vol. 2018, p. 040, Dec. 2018.

129. S. U. Khan, M. Shahzadi, and J. Ren, "Particle collisions in ergoregion of braneworld Kerr black hole," Physics of the Dark Universe, vol. 26, p. 100331, Dec. 2019.

130. R. A. Konoplya, "Shadow of a black hole surrounded by dark matter," Physics Letters B, vol. 795, pp. 1-6, Aug. 2019.

131. S. Haroon, M. Jamil, K. Jusufi, K. Lin, and R. B. Mann, "Shadow and deflection angle of rotating black holes in perfect fluid dark matter with a cosmological constant," , vol. 99, p. 044015, Feb. 2019.

132. M. Akramov, B. Eshchanov, S. Usanov, S. Norbekov, and D. Matrasulov, "Second-harmonic generation in branched optical waveguides: Metric graphs based approach," Physics Letters A, vol. 524, p. 129827, Nov. 2024.

133. K. Jusufi, M. Jamil, and T. Zhu, "Shadows of Sgr A* black hole surrounded by superfluid dark matter halo," European Physical Journal C, vol. 80, p. 354, May 2020.

134. J. Rayimbaev, S. Shaymatov, and M. Jamil, "Dynamics and epicyclic motions of particles around the Schwarzschild-de Sitter black hole in perfect fluid dark matter," European Physical Journal C, vol. 81, p. 699, Aug. 2021.

135. A. Kumar, A. Sood, J. K. Singh, A. Beesham, and S. G. Ghosh, "Phase structure and critical behaviour of charged-AdS black holes with perfect fluid dark matter," Physics of the Dark Universe, vol. 40, p. 101220, May 2023.

136. Rakhimova, F. Atamurotov, F. Javed, A. Abdujabbarov, and G. Mustafa, "Thermodynamical analysis of charged rotating black hole surrounded by perfect fluid dark matter," Nuclear Physics B, vol. 996, p. 116363, Nov. 2023.

137. Mustafa, G. and Javed, Faisal and Maurya, S. K. and Ray, Saibal, "Possibility of stable thin-shell around wormholes within string cloud and quintessential field via the van der Waals and polytropic EOS," Chinese Journal of Physics, vol. 88, pp. 32-54, Apr. 2024.

138. S. W. Hawking, "Particle creation by black holes," Communications in Mathematical Physics, vol. 43, pp. 199-220, Aug. 1975.

139. S. W. Hawking, "Black holes and thermodynamics," , vol. 13, pp. 191197, Jan. 1976.

140. Kubizňák, R. B. Mann, and M. Teo, "Black hole chemistry: thermodynamics with Lambda," Classical and Quantum Gravity, vol. 34, p. 063001, Mar. 2017.

141. I. Kaygorodov, A. Khudoyberdiyev, and Z. Shermatova, "Transposed Poisson structures on Virasoro-type algebras," Journal of Geometry and Physics, vol. 207, p. 105356, Jan. 2025.

142. B. Narzilloev and B. Ahmedov, "Regular black hole solution in PFDM environment to explain the radiative efficiency of black hole candidates," , vol. 98, p. 101922, Jan. 2023.

143. M. Rizwan and K. Jusufi, "Topological classes of thermodynamics of black holes in perfect fluid dark matter background," European Physical Journal C, vol. 83, p. 944, Oct. 2023.

144. V. Vertogradov and A. Övgün, "Exact regular black hole solutions with de sitter cores and hagedorn fluid," Classical and Quantum Gravity, vol. 42, p. 025024, Dec. 2024.

145. K. A. Bronnikov, "Regular magnetic black holes and monopoles from nonlinear electrodynamics," Physical Review D, vol. 63, p. 044005, 2001.

146. Bambi, D. Malafarina, and L. Modesto, "Non-singular quantuminspired gravitational collapse," Physical Review D, vol. 88, Aug. 2013.

147. Ayón-Beato and A. García, "Regular black hole in general relativity coupled to nonlinear electrodynamics," Physical Review Letters, vol. 80, pp. 5056-5059, 1998.

148. Ayon-Beato and A. Garcia, "The bardeen model as a nonlinear magnetic monopole," General Relativity and Gravitation, vol. 31, pp. 629633, 1999.
149. C. Bambi and L. Modesto, "Rotating regular black holes," Physics Letters B, vol. 721, pp. 329-334, 2013.
150. J. Rayimbaev, M. Figueroa, Z. c. v. Stuchlík, and B. Juraev, "Test particle orbits around regular black holes in general relativity combined with nonlinear electrodynamics," Phys. Rev. D, vol. 101, p. 104045, May 2020.
151. Z.-Y. Fan and X. Wang, "Construction of regular black holes in general relativity," Physical Review D, vol. 94, p. 124027, 2016.
152. Z.-Y. Fan and X. Wang, "Construction of regular black holes in general relativity," Physical Review D, vol. 94, Dec. 2016.
153. O. Zaslavskii, "Regular black holes and energy conditions," Physics Letters B, vol. 688, p. 278-280, May 2010.
154. J. Neves and A. Saa, "Regular rotating black holes and the weak energy condition," Physics Letters B, vol. 734, p. 44-48, June 2014.
155. S. Rakhmanov, K. Matchonov, H. Yusupov, K. Nasriddinov, and D. Matrasulov, "Optical high harmonic generation in Dirac materials," The European Physical Journal B, vol. 98, p. 35, Feb. 2025.
156. E.-A. Kontou and K. Sanders, "Energy conditions in general relativity and quantum field theory," Classical and Quantum Gravity, vol. 37, p. 193001, Sept. 2020.
157. S. Capozziello, F. S. Lobo, and J. P. Mimoso, "Energy conditions in modified gravity," Physics Letters B, vol. 730, p. 280-283, Mar. 2014.
158. M. Novello, S. E. Perez Bergliaffa, and J. Salim, "Nonlinear electrodynamics and the acceleration of the universe," Physical Review D, vol. 69, June 2004.
159. R. Penrose, "Gravitational collapse and space-time singularities," Phys. Rev. Lett., vol. 14, pp. 57-59, 1965.
160. V. SAHNI and A. STAROBINSKY, "The case for a positive cosmological -term," International Journal of Modern Physics D, vol. 09, p. 373-443, Aug. 2000.
161. R. B. T. Ndongmo, S. Mahamat, T. B. Bouetou, C. B. Tabi, and T. C. Kofane, "Corrected thermodynamics of nonlinear magnetic-charged black hole surrounded by perfect fluid dark matter," International Journal of Theoretical Physics, vol. 63, June 2024.
162. B. Turimov, S. Usanov, and Y. Khamroev, "Particles acceleration by Bocharova-Bronnikov-Melnikov-Bekenstein black hole," Physics of the Dark Universe, vol. 48, p. 101876, May 2025.

163. K. Glampedakis and D. I. Jones, "Pitfalls in applying gravitomagnetism to galactic rotation curve modelling," Class. Quant. Grav., vol. 40, no. 14, p. 147001, 2023.
164. D. Clowe, M. Bradač, A. H. Gonzalez, M. Markevitch, S. W. Randall, C. Jones, and D. Zaritsky, "A direct empirical proof of the existence of dark matter," The Astrophysical Journal, vol. 648, p. L109-L113, Aug. 2006.
165. Nesti, P. Salucci, and N. Turini, "The quest for the nature of the dark matter: The need of a new paradigm," Astronomy, vol. 2, p. 90-104, May 2023.
166. Y. Kurmanov, K. Boshkayev, T. Konysbayev, O. Luongo, N. Saiyp, A. Urazalina, G. Ikhsan, and G. Suliyeva, "Accretion disks properties around regular black hole solutions obtained from non-linear electrodynamics," Phys. Dark Univ., vol. 46, p. 101566, 2024.
167. S. G. Ghosh and R. K. Walia, "Rotating black holes in general relativity coupled to nonlinear electrodynamics," Annals of Physics, vol. 434, p. 168619, Nov. 2021.
168. K. Mkrtchyan and M. Svazas, "Solutions in nonlinear electrodynamics and their double copy regular black holes," Journal of High Energy Physics, vol. 2022, Sept. 2022.
169. E. Ayon-Beato and A. Garcia, "Regular black hole in general relativity coupled to nonlinear electrodynamics," Phys. Rev. Lett., vol. 80, pp. 5056-5059, 1998.
170. M. Novello, E. Goulart, J. M. Salim, and S. E. Perez Bergliaffa, "Cosmological Effects of Nonlinear Electrodynamics," Class. Quant. Grav., vol. 24, pp. 3021-3036, 2007.
171. M. Novello, S. E. Perez Bergliaffa, and J. Salim, "Non-linear electrodynamics and the acceleration of the universe," Phys. Rev. D, vol. 69, p. 127301, 2004.
172. B. Benaoum, L. A. García, and L. Castañeda, "Early dark energy induced by non-linear electrodynamics," 72023.
173. N. Beissen, M. Abishev, S. Toktarbay, T. Yernazarov, Y. Aimuratov, and M. Khassanov, "Nonlinear electrodynamical lensing of electromagnetic waves on the dipole magnetic field of the magnetar," Int. J. Mod. Phys. D, vol. 32, no. 16, p. 2350106, 2023.
174. N. Breton and R. Garcia-Salcedo, "Nonlinear Electrodynamics and black holes," 22007.
175. J. Mosquera Cuesta and J. M. Salim, "Non-linear electrodynamics and the gravitational redshift of highly magnetized neutron stars," Monthly Notices of the Royal Astronomical Society, vol. 354, p. L55-L59, Nov. 2004.
176. A. Bronnikov, "Regular black holes sourced by nonlinear electrodynamics," 112022.

177. C. Fonseca-Barbatti, M. Novello, J. M. Salim, and R. C. Arcuri, "Creation of a wormhole due to nonlinear electrodynamics," Mod. Phys. Lett. A, vol. 17, pp. 1305-1314, 2002.

178. F. Atamurotov, S. Shaymatov, P. Sheoran, and S. Siwach, "Charged black hole in 4d einstein-gauss-bonnet gravity: particle motion, plasma effect on weak gravitational lensing and centre-of-mass energy," Journal of Cosmology and Astroparticle Physics, vol. 2021, p. 045, Aug. 2021.

179. I. Nishonov, J. Rayimbaev, S. U. Khan, M. Zahid, T. Tolibjanov, and I. Ibragimov, "Collisions and particle dynamics around black holes surrounded by PFDM in STVG," Eur. Phys. J. C, vol. 85, no. 3, p. 325, 2025.

180. Z. Babar, F. Atamurotov, S. Ul Islam, and S. G. Ghosh, "Particle acceleration around rotating einstein-born-infeld black hole and plasma effect on gravitational lensing," Phys. Rev. D, vol. 103, p. 084057, Apr 2021.

181. A. Abdujabbarov, B. J. Ahmedov, and V. G. Kagramanova, "Particle motion and electromagnetic fields of rotating compact gravitating objects with gravitomagnetic charge," General Relativity and Gravitation, vol. 40, pp. 2515-2532, Dec. 2008.

182. Nishonov, M. Zahid, S. U. Khan, J. Rayimbaev, and A. Abdujabbarov, "Dynamics and collision of particles in modified black-bounce geometry," European Physical Journal C, vol. 84, p. 829, Aug. 2024.

183. V. P. Frolov, "Weakly magnetized black holes as particle accelerators," , vol. 85, p. 024020, Jan. 2012.

184. Kovář, P. Slaný, C. Cremaschini, Z. Stuchlík, V. Karas, and A. Trova, "Electrically charged matter in rigid rotation around magnetized black hole," , vol. 90, p. 044029, Aug. 2014.

185. A. Tursunov, Z. Stuchlík, and M. Kološ, "Circular orbits and related quasiharmonic oscillatory motion of charged particles around weakly magnetized rotating black holes," , vol. 93, p. 084012, Apr. 2016.

186. S. S. Kutlimuratov, N. B. Otojanova, and I. U. Tadjibaev, "Calculation of the Anisotropy Parameter for Galaxy Clusters," Ukrainian Journal of Physics, vol. 69, no. 6, pp. 367-372, 2024.

187. Z. Stuchlík and M. Kološ, "Acceleration of the charged particles due to chaotic scattering in the combined black hole gravitational field and asymptotically uniform magnetic field," European Physical Journal C, vol. 76, p. 32, Jan. 2016.

188. Vrba, A. Abdujabbarov, A. Tursunov, B. Ahmedov, and Z. Stuchlík, "Particle motion around generic black holes coupled to non-linear electrodynamics," European Physical Journal C, vol. 79, p. 778, Sept. 2019.

189. Rayimbaev, M. Figueroa, Z. Stuchlík, and B. Juraev, "Test particle orbits around regular black holes in general relativity combined with nonlinear electrodynamics," , vol. 101, p. 104045, May 2020.

190. J. Rayimbaev, S. Shaymatov, and M. Jamil, "Dynamics and epicyclic motions of particles around the Schwarzschild-de Sitter black hole in perfect fluid dark matter," European Physical Journal C, vol. 81, p. 699, Aug. 2021.

191. B. Toshmatov, O. Rahimov, B. Ahmedov, and A. Ahmedov, "Capture of Massless and Massive Particles by Parameterized Black Holes," Galaxies, vol. 9, p. 65, Sept. 2021.

192. B. Ahmedov, O. Rahimov, and B. Toshmatov, "Gravitational Capture Cross-Section of Particles by Schwarzschild-Tangherlini Black Holes," Universe, vol. 7, p. 307, Aug. 2021.

193. O. Rahimov, B. Toshmatov, Y. Vyblyi, A. Akhmedov, and B. Abdulazizov, "Charged particle dynamics in Reissner-Nordström-Tangherlini spacetime," Physics of the Dark Universe, vol. 44, p. 101483, May 2024.

194. B. Turimov, O. Rahimov, B. Ahmedov, Z. Stuchlík, and K. Boymurodova, "Dynamical motion of matter around a charged black hole," International Journal of Modern Physics D, vol. 30, pp. 2150037-407, Apr. 2021.

195. B. Turimov, A. Mamadjanov, and O. Rahimov, "Hawking Radiation and Lifetime of Primordial Black Holes in Braneworld," Galaxies, vol. 11, p. 70, May 2023.

196. B. Rahmatov, M. Zahid, J. Rayimbaev, R. Rahim, and S. Murodov, "QPOs and circular orbits around black holes in Chaplygin-like cold dark matter," Chinese Journal of Physics, vol. 92, pp. 143-165, Dec. 2024.

197. S. Kutlimuratov, N. Otojanova, I. Tadjibaev, and K. Tillaboev, "A study of the dynamic evolution of spherical gravitating systems," EU REKA: Physics and Engineering, vol. 4 (2024), no. 4, pp. 3-12, 2024.

198. E. Ayon-Beato, "New regular black hole solution from nonlinear electrodynamics," Physics Letters B, vol. 464, pp. 25-29, 1999.

199. J. M. Bardeen, B. Carter, and S. W. Hawking, "The four laws of black hole mechanics," Communications in Mathematical Physics, vol. 31, pp. 161-170, June 1973.

200. C. H. Nam, "Non-linear charged AdS black hole in massive gravity," European Physical Journal C, vol. 78, p. 1016, Dec. 2018.

201. S. Ali, S. G. Ghosh, and S. D. Maharaj, "Effective thermodynamics and critical phenomena of rotating regular-de Sitter black holes," Classical and Quantum Gravity, vol. 37, p. 185003, Sept. 2020.

202. M.-H. Li and K.-C. Yang, "Galactic dark matter in the phantom field," Phys. Rev. D, vol. 86, p. 123015, Dec 2012.

203. H.-X. Zhang, Y. Chen, T.-C. Ma, P.-Z. He, and J.-B. Deng, "Bardeen black hole surrounded by perfect fluid dark matter *," Chinese Physics C, vol. 45, p. 055103, May 2021.

204. I. Shakura and R. A. Sunyaev, "Black holes in binary systems. Observational appearance," Astron. Astrophys., vol. 24, pp. 337-355, 1973.

205. S. Murodov, J. Rayimbaev, B. Ahmedov, and E. Karimbaev, "Quasiperiodic Oscillations and Dynamics of Test Particles around Quasi- and Non-Schwarzschild Black Holes," Universe, vol. 9, p. 391, Aug. 2023.

206. J. Rayimbaev, F. Abdulxamidov, S. Tojiev, A. Abdujabbarov, and F. Holmurodov, "Test Particles and Quasiperiodic Oscillations around Gravitational Aether Black Holes," Galaxies, vol. 11, p. 95, Sept. 2023.

207. R. A. Remillard and J. E. McClintock, "X-Ray Properties of BlackHole Binaries," Annual Review of Astronomy and Astrophysics, vol. 44, pp. 49-92, Sep 2006.

208. S. Jumaniyozov, S. U. Khan, J. Rayimbaev, A. Abdujabbarov, S. Urinbaev, and S. Murodov, "Circular motion and QPOs near black holes in Kalb-Ramond gravity," European Physical Journal C, vol. 84, p. 964, Sept. 2024.

209. J. Rayimbaev, S. Murodov, A. Shermatov, and A. Yusupov, "Qpos from charged particles around magnetized black holes in braneworlds," The European Physical Journal C, vol. 84, no. 10, p. 1114, 2024.

210. Mustafa, E. Demir, F. Javed, S. Maurya, E. Güdekli, S. Murodov, and F. Atamurotov, "Epicyclic oscillations and particle collision with trajectories around quantum corrected black holes," Physics of the Dark Universe, vol. 46, p. 101708, 2024.

211. A. Caliskan, G. Mustafa, T. Naseer, S. K. Maurya, E. Güdekli, S. Murodov, and F. Atamurotov, "Particle dynamics with trajectories and epicyclic oscillations around a piece-wise black hole immersed in dark matter," Journal of High Energy Astrophysics, vol. 44, pp. 99-115, Nov. 2024.

212. Z. Stuchlík and M. Kološ, "Mass of intermediate black hole in the source M82 X-1 restricted by models of twin high-frequency quasi-periodic oscillations," Mon. Not. R. Astron. Soc Soc., vol. 451, pp. 2575-2588, Aug. 2015.